THESIS

DEVELOPMENT OF INTERNALLY-CALIBRATED, DIRECT DETECTION MILLIMETER-WAVE RADIOMETERS TO IMPROVE REMOTE SENSING OF WET-TROPOSPHERIC PATH DELAY

Submitted by

Victoria D. Hadel

Department of Electrical and Computer Engineering

In partial fulfillment of the requirements

For the Degree of Master of Science

Colorado State University

Spring 2015

Master's Committee:

Advisor: Steven C. Reising

Pekka Kangaslahti
Branislav Notaros
Susan Van Den Heever

ABSTRACT

DEVELOPMENT OF INTERNALLY-CALIBRATED, DIRECT DETECTION MILLIMETER-WAVE RADIOMETERS TO IMPROVE REMOTE SENSING OF WET-TROPOSPHERIC PATH DELAY

Satellite ocean altimeters measure the sea surface height by emitting a radar pulse and measuring the time for it to propagate to the surface, bounce off and return to the satellite. Assuming speed-of-light propagation, the sea surface height can be determined. However, water vapor in the atmosphere, which is highly variable both temporally and spatially, reduces the propagation speed of these radar signals, in turn increasing the round-trip radar propagation time, leading to substantial errors in the sea surface height estimation. This delay in the arrival time of radar pulse returns is referred to as wet-tropospheric path delay.

Past and current satellite ocean altimeters include nadir-viewing, co-located 18-34 GHz microwave radiometers to measure wet-tropospheric path delay with a precision of 1 cm. However, due to the large antenna footprint sizes at these frequencies, the accuracy of wet path retrievals is substantially degraded within 40 km of coastlines, and retrievals are not provided over land. Because footprint diameter is directly proportional to wavelength for the same antenna aperture size, a viable approach to improve their capability is to add wide-band millimeter-wave window channels in the 90-175 GHz band, thereby achieving finer spatial resolution for a fixed antenna size.

To address this need, an internally-calibrated, wide-band, cross-track scanning airborne microwave and millimeter-wave radiometer has been collaboratively developed between Colorado State University (CSU) and Caltech/NASA's Jet Propulsion Laboratory (JPL). This airborne radiometer, referred to as the High Frequency Airborne Microwave and Millimeter Wave Radiometer (HAMMR) includes microwave channels at 18.7, 23.8, and 34.0 GHz at both Quasi-H and Quasi-V polarizations, millimeter-wave window channels at 90, 130, and 168 GHz, as well as temperature and water vapor sounding channels near the 118 and 183 GHz absorption lines, respectively. Since this instrument also serves as a prototype for potential future Earth science missions, substantial effort has been devoted to minimizing the mass, size and power consumption of the radiometer. Preliminary airborne measurements of the HAMMR demonstrate the reliable and robust operation of the millimeter-wave window and sounding channels on an airborne platform, as well as the improvement in spatial resolution that they provide, over that of the traditional microwave channels.

ACKNOWLEDMENTS

I would first like to thank Prof. Steven C. Reising for his support and guidance, not only as my adviser in this research, but also as a role model and mentor for the past four years. I would like to thank Dr. Pekka Kangaslahti, Prof. Branislav Notaros, and Prof. Sue Van Den Heever for their input on my thesis and for serving on my committee.

I would like to thank the HAMMR IIP-10 team at Caltech/NASA's Jet Propulsion Laboratory for their technical contributions, support, and guidance throughout my thesis. Specifically, I would like to thank Dr. Pekka Kangaslahti, Dr. Sharmila Padmanabhan, Dr. Alan Tanner, Dr. Chaitali Parashare, and Mr. Oliver Montes.

I would like to thank Dr. Javier Bosch-Lluis for his technical contributions and invaluable feedback throughout the research completed for this thesis. I would also like to thank my peers in the Microwave Systems Laboratory, especially Mr. Thaddeus Johnson, for their contributions and assistance with this work.

Finally, I would like to thank my family and my dear friend Meghan Schneider for their unwavering support and patience.

DEDICATION

I would like to dedicate this thesis to my wonderful, supportive family and dear friend Meghan Schneider.

TABLE OF CONTENTS

LIST OF FIGURES

Chapter I Introduction

The purpose of this thesis is to describe the development and fabrication of the High-frequency Airborne Microwave and Millimeter-Wave Radiometer (HAMMR). In particular, this thesis focuses on the design, testing and airborne demonstration of the high-frequency, millimeter-wave window and sounding channels of this 25-channel, cross-track scanning radiometer instrument. HAMMR was developed under the Instrument Incubator Program 2010 funded by the National Aeronautics and Space Administration (NASA)'s Earth Science Technology Office (ESTO). ESTO is directed by Mr. George Komar, and the lead for Advanced Observation Technology is Mr. Parminder Ghuman. The HAMMR IIP-10 program is led by Principal Investigator Prof. Steven C. Reising and is a collaborative effort between the Colorado State University (CSU) Microwave Systems Laboratory (MSL) and NASA's Jet Propulsion Laboratory (JPL), California Institute of Technology (Caltech). An overview of the motivation for the development of the HAMMR instrument and the fundamentals of radiometry, particularly in the microwave and millimeter-wave regions of the electromagnetic spectrum, are presented in this section, and the contents of this thesis are described.

1.1. Scientific Motivation

The 2007 U.S. National Research Council (NRC)'s Earth Science Decadal Survey entitled, "Earth Science and Applications from Space: National Imperatives for the Next Decade and Beyond," [1] recommended the Surface Water and Ocean

Topography (SWOT) mission as one of the Tier II Missions. After a number of years of SWOT feasibility studies, on May 2, 2014, in Washington, DC, NASA Administrator Charles Bolden and Centre National d'Études Spatiales (CNES, the French Space Agency) President Jean-Yves Le Gall signed an agreement for joint implementation of the SWOT mission, now planned for launch in late 2020 [2].

The SWOT mission has two broad scientific objectives in oceanography and hydrology. The primary oceanographic goal is to characterize mesoscale (~5 km-100 km) and sub-mesoscale (< 5 km) circulation by measuring the sea surface height with a horizontal spatial resolution of 15 km (over 68% of the world's oceans) and 1 cm (baseline) to 3 cm (threshold) vertical resolution [3]. Current constellations of altimeters can resolve the ocean circulation only at a horizontal spatial resolution of 200 km. However, it is necessary to measure at significantly smaller scales to understand the heat and carbon exchange between the ocean and atmosphere and to improve knowledge of coastal and internal tides. The primary hydrological objective is to improve measurement of the water cycle on a global basis. Specifically, SWOT intends to measure changes in water storage of large inland bodies with surface area of greater than 250 m^2 and rivers with greater than 100 m width by measuring changes in their surface height [3]. These measurements of the global change in water storage and river dynamics are intended to improve our understanding of global fresh water changes on regional to global scales.

The National Research Council's (NRC) mid-term review in 2012 (five years after the Decadal Survey) entitled "Earth Science and Applications from Space: A Midterm Assessment of NASA's Implementation of the Decadal Survey" [1] points out that, "the [Earth Science Decadal] survey's Surface Water Ocean Topography (SWOT) mission is being considered as a multidisciplinary cooperative international effort that builds on a long-lived and successful U.S. and French partnership. The SWOT satellite mission will expand on previous altimetry flights (e.g., TOPEX/Poseidon) through wide-swath altimetry technology to completely cover the world's oceans and freshwater bodies with repeated high-resolution elevation measurements."

1.2. Wet-Tropospheric Path Delay

Planned for launch in 2020, SWOT will expand on 22 years of collaboration to date between the U.S. and France on precision global sea surface altimetry missions, including TOPEX (launched in 1992), Jason-1 (launched in 2001), Ocean Surface Topography Mission (OSTM)/Jason-2 (launched in 2008), and the upcoming Jason-3 (scheduled for launch in 2015) [4]. SWOT will use the new Ka-band Radar Interferometer (KaRIN) to measure the height of the sea surface, as well as inland bodies of water, including lakes and rivers, with unprecedented horizontal resolution on a global basis.

Precision altimetry requires correction for variations in the amount of atmospheric water vapor along the propagation path between the satellite and the surface. The reason is that the change in the index of refraction of the atmosphere due to water vapor causes a change in the speed of propagation of the radar signal and delays the time of the return from the surface. This wet-tropospheric path delay causes a significant error in sea surface height estimates.

Past and current high-precision satellite ocean altimeter missions include nadir-viewing, co-located 18-34 GHz multi-channel microwave radiometers to retrieve integrated water vapor, closely related to wet-tropospheric path delay. However, these microwave radiometers at relatively low frequencies of 18-34 GHz have large surface footprints that degrade wet path retrievals at approximately 40 km from the coasts, as shown in Figure 1.

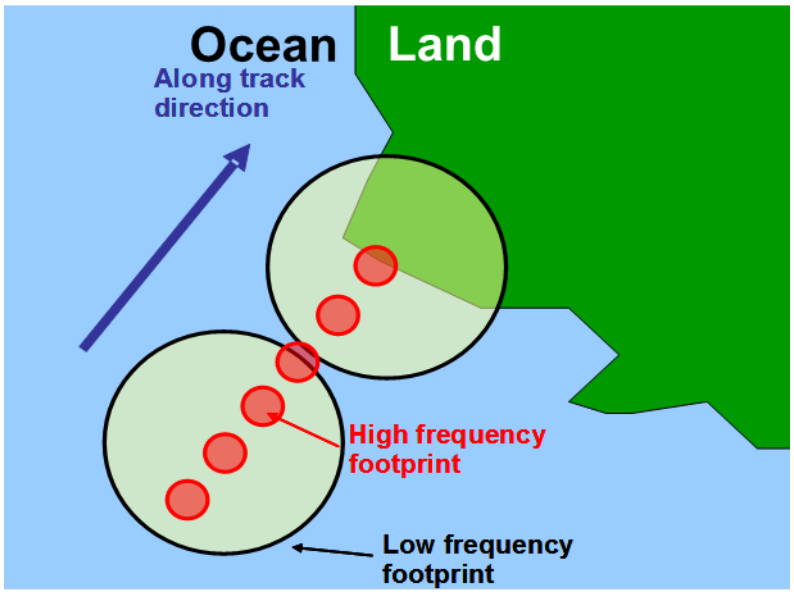

Figure 1: Schematic Comparison of the Footprints of Low and High Frequency Radiometers [5], [6]

The degradation of the radiometer's brightness temperature measurements is caused by the large magnitude and large variability of the microwave emissivity of land surfaces. Microwave brightness temperatures near the world's coastlines depend on surface temperature, vegetation, surface roughness, snow and ice cover, soil moisture and water vapor in the atmosphere. The addition of high frequency, millimeter-wave window channels in the range of 90-175 GHz is expected to enable sea surface height measurements closer to the coasts due to their smaller footprints, which are proportional to wavelength for a given antenna aperture size.

1.3. Instrument Incubator Program (IIP) Objectives

The research completed for this thesis was performed as part of the Instrument Incubator Program (IIP) 2010 project led by Principal Investigator Prof. Steven C. Reising. The IIP is one of several initiatives administered by NASA ESTO to develop new, innovative technologies to reduce risk, cost, mass, size and power consumption of future Earth science missions. For these programs, the technology readiness level (TRL) is used to describe the maturity of any technology in terms of its level of progression toward readiness for space flight. During these funded projects, the components, subsystems, and instruments progress from the early stages of development through readiness to build engineering models of space-flight hardware [7]. A number of the programs administered by NASA ESTO and their corresponding disciplines and range of TRLs are shown in Figure 2.

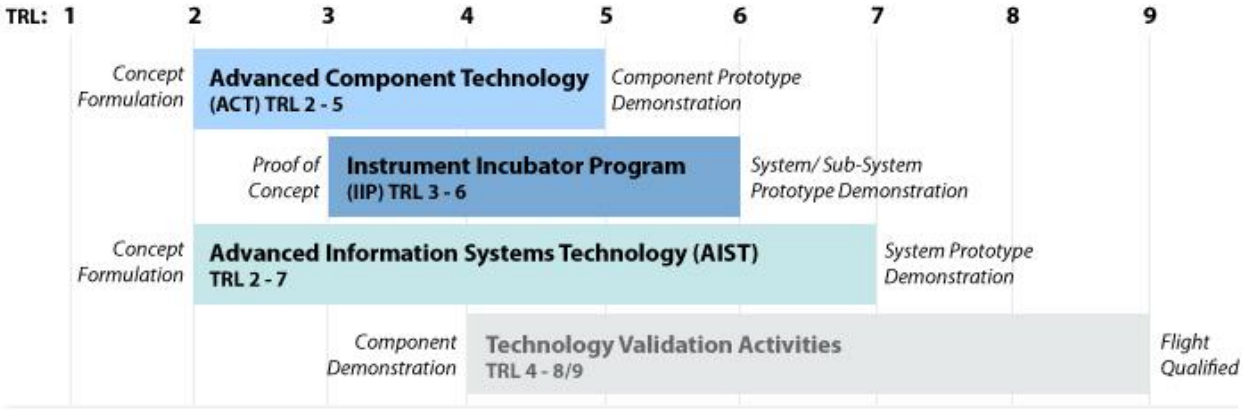

Figure 2: NASA ESTO Programs and Corresponding Range of Technology Readiness Level (TRL) [8]

The development of technologies for laboratory prototypes of high-frequency millimeter-wave radiometers was accomplished in collaboration between the Microwave Systems Laboratory (MSL) at Colorado State University (CSU) and the NASA Jet Propulsion Laboratory (JPL), California Institute of Technology (Caltech). This program was conducted under the Advanced Component Technology (ACT-08) project led by Principal Investigator Prof. Steven C. Reising. The main goal of the IIP-10, which builds upon the work done on the ACT-08, is to design, fabricate, test and demonstrate an airborne millimeter-wave window and sounding (i.e., to retrieve temperature and humidity profiles) radiometer instrument. The technologies necessary for the high-frequency, millimeter-wave window and sounding radiometer channels were at TRL 3 at the start of the IIP-10 project, and they were increased to TRL 6 through airborne demonstration during the project.

1.4. Thesis Organization and Description

The remainder of this thesis is divided into six chapters. Chapter II introduces the fundamental concepts of Planck blackbody radiation, atmospheric opacity and radiometry for remote sensing. Chapter III gives an overview of the HAMMR instrument, including the functionality of its radiometer channels and subsystems. It includes a description of the microwave radiometer channels developed by JPL. Chapter IV provides a detailed description of the contributions of this thesis to the design and fabrication of the millimeter-wave sounding channels. Chapter V describes the design, simulation and measurement results for components and subsystems comprising the millimeter-wave window channels. Chapter VI provides a first look at the first airborne measurements performed using the HAMMR instrument during July 2014. Finally, Chapter VII presents the summary and conclusions of the thesis.

Chapter II Fundamentals of Passive Microwave Remote Sensing

Radiometers are used to measure the electromagnetic energy emitted by a body. Passive microwave remote sensing consists of measuring the energy emitted or radiated by a body at a number of frequencies, and inferring therefrom certain characteristics of the body. In the context of this thesis, radiometers are used to measure properties of the atmosphere, but emission or radiation from the surface normally plays a role as well. This chapter provides an introduction to the fundamentals of atmospheric radiation, radiometry and radiometer topologies.

2.1. Atmospheric Radiation

Fundamental concepts of an ideal blackbody are presented in this section along with a radiative transfer model relating the antenna temperature measured by a radiometer, typically converted to brightness temperature, to properties of the atmosphere.

2.1.1 Ideal Blackbody

All matter absorbs and emits electromagnetic radiation [9]. An ideal blackbody is a perfect emitter of electromagnetic radiation. If the body has reached thermal equilibrium, all of the energy it absorbs is emitted. The spectral brightness emitted by a blackbody at physical temperature T is given by Planck's Law in (II.1).

$$B_f = \frac{2hf^3}{c^2}\left(e^{\frac{hf}{kT}} - 1\right)^{-1} \tag{II.1}$$

where B_f is the spectral brightness of an object in Watts per square meter per steradian per Hertz (W/(m^{2}SrHz)), h is Planck's constant in Joule seconds (*Js*), f is frequency in Hertz (Hz), k is Boltzmann's constant in Joules per Kelvin (J/K), T is absolute physical (or thermodynamic, as opposed to brightness) temperature in K, and c is the speed of light in meters per second (m/s) [9]. For frequencies in the microwave and millimeter-wave range, the exponential term in (II.1) is close to unity and can be approximated by its first-order Taylor series' approximation as (II.2).

$$\frac{hf}{kT} << 1$$
$$e^{\frac{hf}{kT}} - 1 \approx \frac{hf}{kT} \tag{II.2}$$

With this approximation, Planck's Law (II.1) becomes (II.3), Rayleigh-Jeans' Law [9].

$$B_f = \frac{2kT}{\lambda^2} \tag{II.3}$$

where λ is wavelength in meters. The Rayleigh-Jeans' Law exhibits a linear relationship between the spectral brightness and the physical temperature. It is valid in the microwave and millimeter-wave frequency regions, where the error due

to the approximation increases with frequency and is less than 3% at 300 GHz [9].

2.1.2 Antennas and Blackbody Radiators

To receive emitted or radiated power from a body, an antenna receives electromagnetic radiation and converts it into energy propagating along a waveguide, coaxial line or wire in an electric circuit. To quantify the amount of power received by the antenna, consider a lossless antenna that receives the radiated power from an ideal blackbody. If an antenna receives radiation according to the Rayleigh-Jeans' Law in a bandwidth B, the received power at the antenna is (II.4).

$$P_{bb} = kTB\frac{A_r}{\lambda^2}\iint_{4\pi} F_n(\theta,\phi)d\Omega \tag{II.4}$$

where P_{bb} is the received power in Watts, A_r is the effective aperture area of the antenna in square meters, and $F_n(\theta,\phi)$ is the normalized radiation pattern of the antenna. Using the relationship in (II.5), (II.4) can be simplified to the linear relationship in (II.6) [9].

$$\frac{\lambda^2}{A_r} = \iint_{4\pi} F_n(\theta,\phi)d\Omega \tag{II.5}$$

$$P_{bb} = kTB \tag{II.6}$$

It is important to note that (II.6) also describes the available output noise power from a resistor of resistance R at a physical temperature T over a bandwidth, B, also known as Nyquist or Johnson noise [9]. Therefore, a lossless antenna observing an ideal blackbody can be modeled as a matched resistor at the antenna terminals and at the same physical temperature as the blackbody.

However, actual bodies are not ideal blackbodies, since they partially reflect energy and do not radiate perfectly. Emissivity, e, is introduced to quantify the relationship between the thermal power radiated by actual bodies and that radiated by an ideal blackbody with the same temperature, T, and over the same bandwidth, B, as (II.7).

$$e = \frac{P}{kTB}\ ,\ 0 \le e \le 1 \tag{II.7}$$

where P is the power radiated by the actual body and kTB is the power emitted from an ideal blackbody, as (II.6). The brightness temperature of an actual body is defined as (II.8).

$$\boldsymbol{T_B = eT} \tag{II.8}$$

where T is the absolute physical temperature of the body. The emissivity of a blackbody is unity, and the emissivity of a perfect reflector is zero. This relationship shows that the brightness temperature of a body is always less than or equal to its absolute physical temperature.

In passive microwave remote sensing, measured brightness temperatures, often at multiple frequencies and polarizations, are used in retrieval algorithms to infer physical characteristics of the body. In Earth remote sensing in particular, the quantities to be retrieved are geophysical characteristics of the land, oceans and atmosphere. To improve retrieval algorithms for passive microwave remote sensing, models are needed for radiometric emission. In this thesis, the emphasis is on the Earth's atmosphere, with properties such as pressure, temperature and humidity, the last of which is often expressed as water vapor content or density.

2.1.3 Atmospheric Attenuation

At millimeter-wave and sub-millimeter-wave frequencies, the major contributors to atmospheric attenuation are oxygen and water vapor (along with continuum contributions from nitrogen and other trace gases) [9]. The atmospheric attenuation coefficients of water vapor, cloud liquid water and oxygen are shown in Figure 3, as calculated using the Rosenkranz model [10].

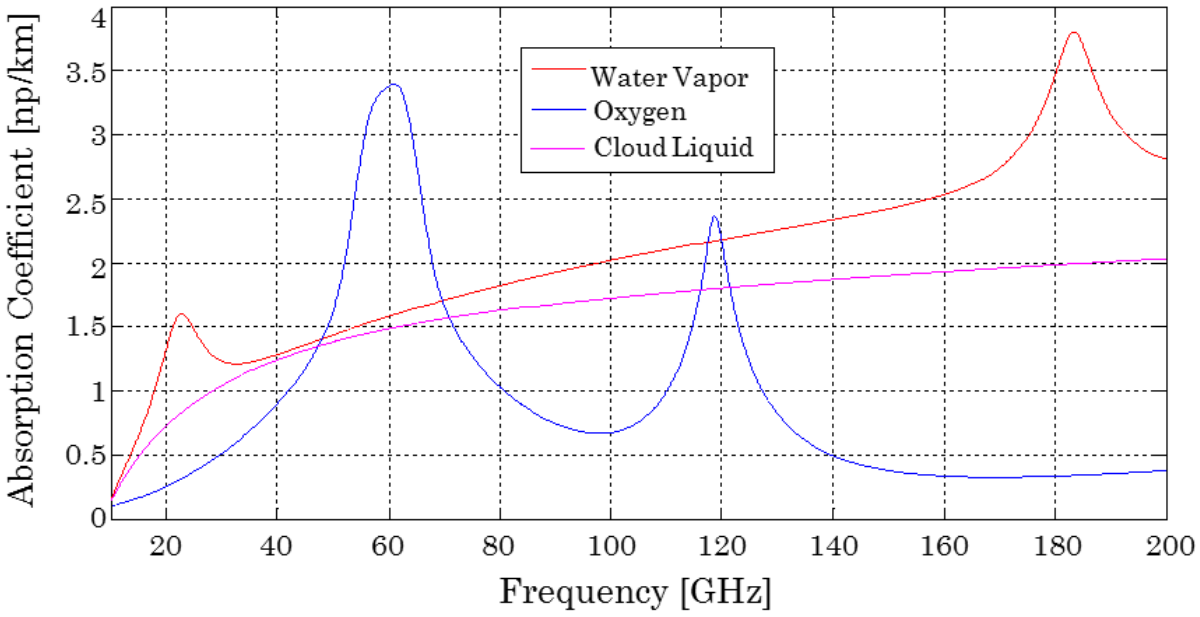

Figure 3: Microwave and Millimeter-Wave Absorption Spectra from 10 to 200 GHz for Water Vapor Density of 15.1 g/m^3, Temperature of 297 K, and Cloud Liquid Water Density of 0.1 g/m^3 [11]

The peaks are absorption lines of oxygen (blue curve) and water vapor (red curve). Frequencies that are sufficiently separated from these absorption lines are considered to be window regions. In these regions, brightness temperatures measured by a nadir-viewing radiometer are generally influenced by both the atmosphere and the surface. The absorption lines and window regions, which have different atmospheric attenuation characteristics, allow retrieval of different atmospheric properties. Brightness temperature measurements near the absorption lines (e.g., 23.8 GHz near a microwave water vapor absorption line) can be used to retrieve total column, or integrated, water vapor. Comparison of brightness temperature measurements near water vapor absorption lines (e.g., 23.8 GHz) with those in window regions (e.g. 34.0 GHz) can distinguish between emission from

water vapor and that from liquid water, typically in the form of clouds or precipitation. Brightness temperature measurements at a number of frequencies near water vapor absorption lines allow retrieval of atmospheric water vapor content at a variety of heights (often referred to as profiling or sounding) due to pressure broadening. Since the amount of oxygen in the atmosphere is constant in the well-mixed troposphere and line width also changes with temperature, brightness temperature measurements at a number of frequencies near the oxygen lines allow the retrieval of atmospheric temperature profiles.

2.1.4 Radiative Transfer Model

The radiative transfer model describes the apparent temperature of the atmosphere, T_{AP}, that is observed by a nadir-viewing radiometer, e.g. mounted on an aircraft. This model, shown in (II.9) for a radiometer observing a scatter-free medium at a range r above the surface, takes atmospheric attenuation into account.

$$T_{AP}(r) = T_{AP}(0)e^{-\tau(0,r)} + \int_0^r \kappa_a(r')T(r')e^{-\tau(r',r)}dr' \qquad \text{(II.9)}$$

where the first term is $T_{AP}(0)$, the apparent temperature of the ground in K, attenuated by $e^{-\tau(0,r)}$, which accounts for the absorption due to the atmosphere along the path measured by the radiometer, and the second term represents the upwelling emission from the atmosphere in the direction of and over the distance to

the radiometer. This model is true in a scatter-free atmosphere [9].

The apparent temperature of the atmosphere can be modeled as the equivalent noise temperature of a matched, non-ideal (noisy) resistor replacing a radiometer antenna at its input terminals. The antenna of a nadir-viewing radiometer receives the power of the apparent temperature of the atmosphere.

2.2. Radiometers

A radiometer is a receiver designed to measure the power of a scene's emitted thermal radiation over a certain bandwidth. The output of an antenna is input at the front end of a radiometer, and the radiometer's output voltage is proportional to the antenna noise temperature, T_A. By compensating for the antenna radiation pattern (including any sidelobes or backlobes that may inadvertently be receiving different brightness temperatures), the antenna noise temperature can be converted to the brightness temperature, T_B, emitted by a uniform scene illuminating the antenna. Although there are many different radiometer topologies, this thesis will discuss the two most basic topologies in super-heterodyne configuration, the total-power radiometer (TPR) and the Dicke radiometer, and a direct-detection radiometer, as opposed to the more common super-heterodyne configuration.

2.2.1 Total Power Radiometers

Figure 4 shows a block diagram of a typical total power radiometer (TPR) in a

super-heterodyne configuration. The pre-detection components of the TPR are an antenna, a radio-frequency (RF) low noise amplifier (LNA), local oscillator (LO), mixer and an intermediate-frequency (IF) amplifier.

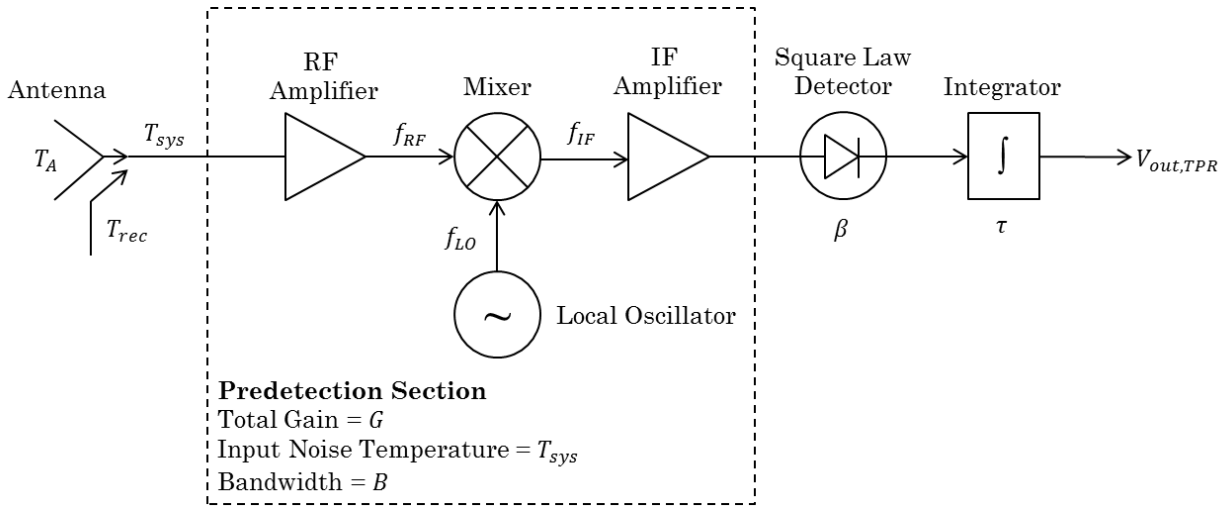

Figure 4: Topology of a Total Power Radiometer

The system noise temperature, T_{sys}, is the sum of the antenna noise temperature, T_A, and the noise added by the receiver, T_{rec}. The purpose of the RF amplifier is to amplify the signal before down-conversion in a specified bandwidth, B, centered at the RF frequency, f_{RF}. The signal is then down converted using a mixer with a local oscillator at a frequency of f_{LO}. The resulting IF signal, centered at the IF frequency, $f_{IF} = f_{RF} - f_{LO}$, is then amplified by an IF amplifier. Afterward, the square law detector outputs a voltage proportional to the amount of power at its input. Finally, an integrator averages the signal over a time period, τ, thereby averaging a number of independent samples (equivalent to the time-bandwidth product, $B\tau$) to reduce the effect of the system noise on the desired signal. The output voltage of an ideal

TPR is defined by the linear relationship (II.10).

$$V_{out,TPR} = kBG\beta T_{sys} \tag{II.10}$$

where B is bandwidth of the system in Hz, G is the overall gain of the radiometer, and β is the detector sensitivity in V/W. The output voltage signal of the square law detector has time-varying Gaussian noise fluctuations which are averaged by the integrator. The minimum change in antenna noise temperature that produces a detectable change in output voltage is equal to the standard deviation of the noise fluctuations during an integration period τ and is called radiometric resolution and defined as ΔT_N in (II.11) [12].

$$\Delta T_N = \frac{T_{sys}}{\sqrt{B\tau}} \tag{II.11}$$

However, the expressions in (II.10) and (II.11) do not take into account time-varying $1/f$ gain fluctuations, ΔG, that occur in a receiver system. The gain fluctuations affect both the output voltage and the minimum noise fluctuation that can be detected, or radiometric resolution of the radiometer. Taking the gain fluctuations into consideration, the output voltage of a TPR is given in (II.12),

$$V_{out,TPR} = kBG\beta T_{sys} + kB\Delta G\beta T_{sys} \tag{II.12}$$

Analogous to (II.11), the standard deviation of gain fluctuations over the integration period, τ, is defined as ΔT_G in (II.13).

$$\Delta T_G = T_{sys}\left(\frac{\Delta G}{G}\right) \tag{II.13}$$

Taking into account the additional uncertainty of gain fluctuations in the system, the minimum noise fluctuation that can be detected is in (II.14).

$$\Delta T_{TPR} = T_{sys}\sqrt{\frac{1}{B\tau} + \left(\frac{\Delta G}{G}\right)^2} \tag{II.14}$$

It has been shown that the radiometric resolution of a TPR, ΔT_{TPR}, is impacted by gain fluctuations, ΔG, in the system. One method to address this issue involves changing the architecture of a TPR to that of a Dicke radiometer.

2.2.2 Dicke Radiometers

Dicke radiometers are total power radiometers to which a single-pole double-throw (SPDT) "Dicke" switch has been added before the first LNA, with one of its two input ports connected to the antenna and the output port connected to the input of the first LNA. The other port is connected to a reference matched load. The block diagram for a Dicke radiometer in super-heterodyne configuration is given in Figure 5. The switch alternates the input to the receiver between the antenna and the

reference matched load with equivalent noise temperature, T_{ref}, (typically implemented by a matched load, which can be implemented as a resistor in microstrip (due to its physical size being a small fraction of a wavelength), at physical temperature, T_{ref}, for a certain fraction of each integration period, τ.

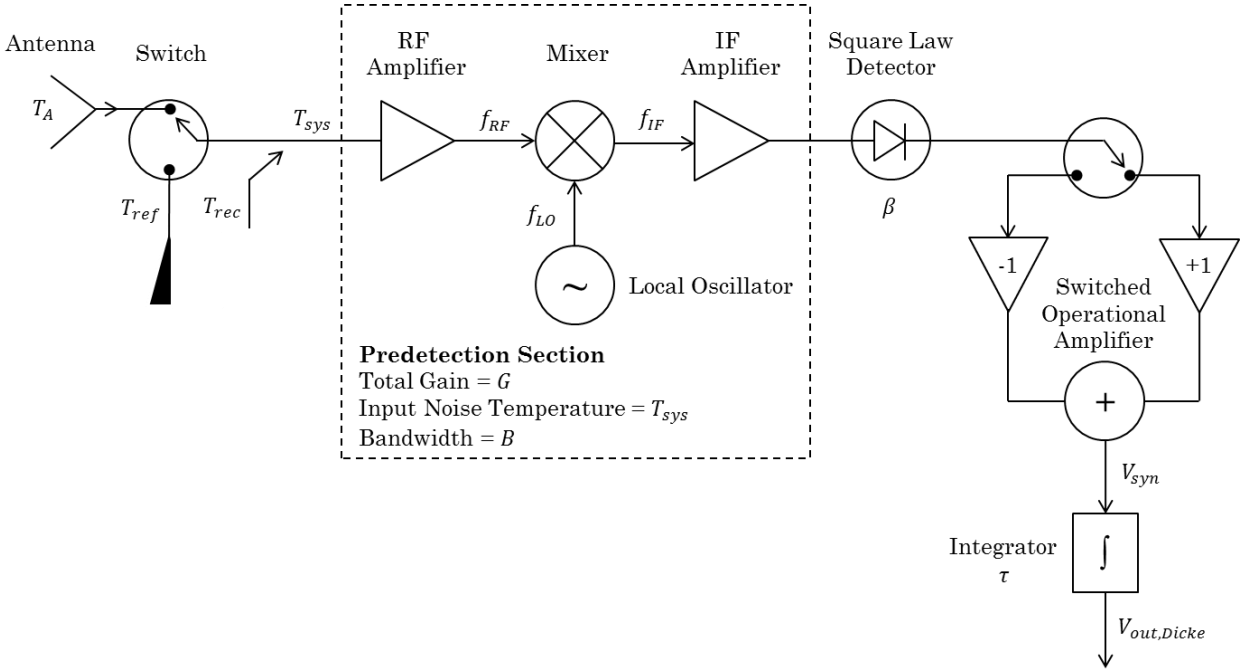

Figure 5: Topology of a Dicke Switched Radiometer

An operational amplifier after the square-law detector is switched between inverting and non-inverting modes, as shown in Figure 5. The operational amplifier is switched between these two modes synchronously with the Dicke switch at the beginning of the receiver chain. The result is that the antenna signal is input to a positive unity gain amplifier and the reference signal is input to a negative unity gain amplifier. If the input to the receiver is switched to the antenna for half of the

time and to the reference matched load for the other half of the time, the output voltage of the integrator is given in (II.15).

$$V_{out,Dicke} = kB\Delta G\beta\left(T_A - T_{ref}\right) \tag{II.15}$$

The T_{ref} term in (II.15) effectively reduces the error in the output voltage due to gain fluctuations and the radiometric resolution of a Dicke radiometer is given in (II.16) [9].

$$\Delta T_{Dicke} = \left[\frac{2(T_A + T_{Rec})^2 + 2\left(T_{Ref} + T_{Rec}\right)^2}{B\tau} + \left(\frac{\Delta G}{G}\right)^2 \left(T_A - T_{Ref}\right)^2\right]^{1/2} \tag{II.16}$$

However, the reduction in error in a Dicke radiometer comes at the expense of an increase in radiometric resolution by a factor of two compared to a TPR for a balanced radiometer with $T_A = T_{Ref}$ and neglecting gain variations in the TPR. This factor of two increase for a balanced radiometer, shown in (II.17), is the result of a reduction of integration time of the signal of interest by a factor of two due to viewing the scene only half of the time.

$$\Delta T_{Dicke,balanced} = \frac{2T_{sys}}{\sqrt{B\tau}} \tag{II.17}$$

From a comparison of (II.11) to (II.16), it appears that the TPR has a better radiometric resolution than a Dicke radiometer; however, since the gain variations

increase with longer integration time, the radiometric resolution of a TPR increases much more rapidly with increasing integration time than that of a Dicke radiometer [9].

2.2.3 Direct-Detection Radiometers

The previous two sections discussed total power radiometers and Dicke radiometers in a super-heterodyne configuration; however, both types of radiometers can also be implemented in a direct-detection configuration. For both total power radiometers and Dicke radiometers, direct-detection configurations have no down-conversion of the radio-frequency (RF) signal to an intermediate-frequency (IF) signal. The detector diode must operate at the RF frequency. Without down conversion, mixers and local oscillators are not needed. In addition to the reduction of both power and complexity, the system noise temperature can often be reduced if LNAs with sufficiently low-noise are available at the RF frequencies used.

2.2.1 Radiometer Calibration

The performance of a radiometer is characterized by both its accuracy and precision. Precision is determined by the radiometric resolution of the radiometer, discussed in the previous sub-section, and accuracy depends upon the quality of calibration of the radiometer.

Calibration of the radiometer can be performed either external to the radiometer

before the antenna or internal to the radiometer after the antenna. In both methods, two loads of known temperatures, one often called "hot" and the other often called "cold," are observed by the receiver. For airborne and ground-based radiometers with external calibration, the hot load is typically at ambient temperature, near 300 K on the ground, and the cold load is typically the temperature of liquid N_2, about 77 K. These measured or *a-priori* known temperature values, T_{hot} and T_{cold}, are related to their respective output voltages, V_{hot} and V_{cold}, in the two-point calibration curve, as illustrated in Figure 6.

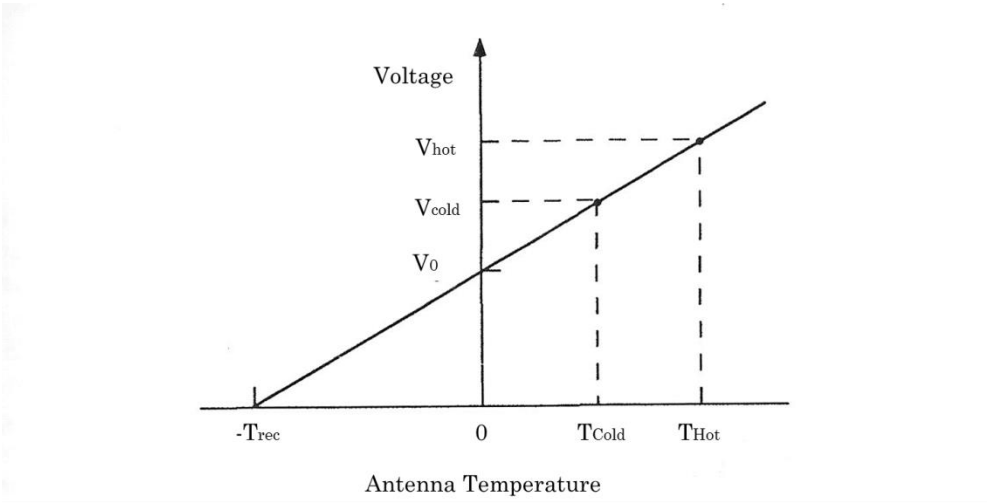

Figure 6: Output Voltage and Antenna Temperature Relationship Used in Calibration [13]

The calibration curve in Figure 6 has an offset due to the receiver noise temperature, T_{rec}, that can be found from the negative x-intercept of the calibration curve [9]. Additionally, assuming the gain fluctuations of the radiometers have been effectively eliminated by the Dicke radiometer, the slope of the calibration curve can be used to determine the gain of the system.

Chapter III System Design

This chapter discusses each of the three sets of radiometer channels in the HAMMR instrument and the contribution of each of them to correcting sea surface altimeter signals for wet-tropospheric path delay. Additionally, all of the HAMMR subsystems and the aircraft used to demonstrate HAMMR operation in flight are also presented here.

3.1. HAMMR System

In addition to the three sets of radiometer channels, many other subsystems comprise the HAMMR instrument. This section presents those subsystems, their functionality in the overall system, and their physical location in HAMMR.

3.1.1 HAMMR Block Diagram

A block diagram of the HAMMR instrument is provided in Figure 7. The HAMMR components and subsystems are needed for the successful operation and airborne demonstration of the radiometers.

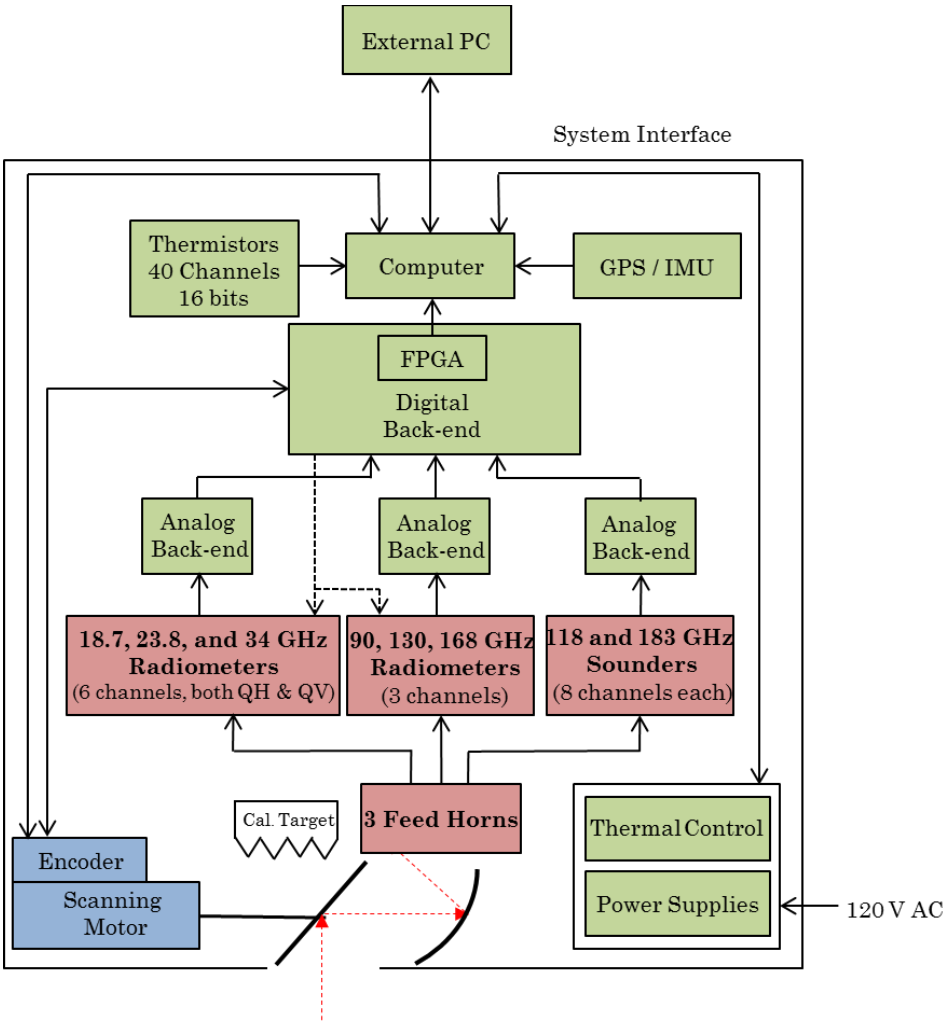

Figure 7: HAMMR System Block Diagram [14]

One flat and one parabolic reflector are used to direct the incoming atmospheric radiation and focus it onto the feed horns of the three radiometers. In addition, the flat reflector scans the antenna beams across the direction of flight, called cross-track scanning. The signal that is reflected onto the parabolic reflector changes as scanning motor rotates the flat reflector over each complete revolution. When the flat reflector is pointed within approximately ±60° of the nadir direction, the emission from the atmosphere is reflected onto the parabolic reflector. When the flat

reflector is pointed within approximately ±40° of the zenith direction, the emission from the calibration target is reflected onto the parabolic reflector. The parabolic reflector reflects and focuses the emission onto the three feed horns of the three sets of radiometer channels. The calibration target, radiometer feed horns, and flat and parabolic reflectors are all shown in Figure 8.

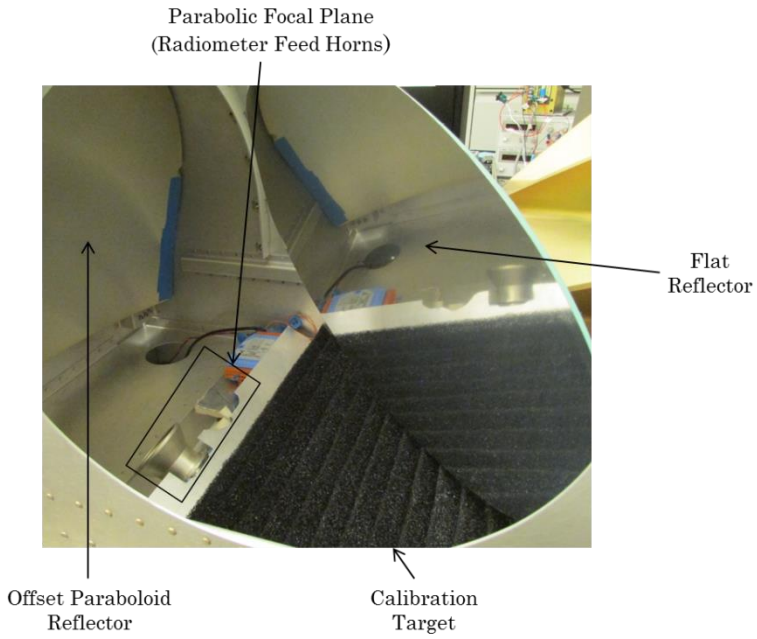

Figure 8: Configuration of Flat and Parabolic Reflector, Calibration Target and Three Feed Horns

The flat reflector is rotated with a scanning motor and encoder from Quick Silver Controls, Inc. [15]. The encoder outputs the motor position to the internal computer, which allows the post-processed data to be matched with the scene being viewed and the incidence angle at which it is viewed.

For external calibration, HAMMR has a wide-band calibration target that was developed by Thaddeus Johnson as part of the IIP-10 project. This calibration target, shown in Figure 8, is used as a blackbody target from 18-183 GHz, with a brightness temperature very similar to its physical temperature [16]. The calibration target is made of ECCOSORB HR-10 [17] and has eight embedded thermistors at different locations and depths, as well as dedicated digitizers to monitor the temperature throughout the target.

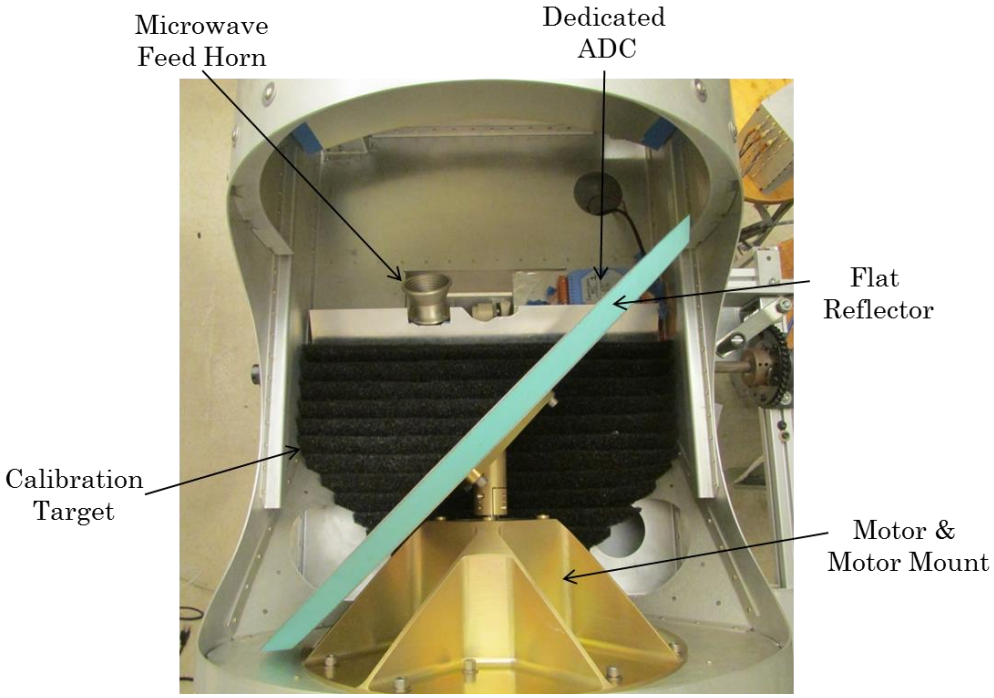

Figure 9: Configuration of Calibration Target, Flat Reflector and Three Feed Horns [16]

The temperature monitoring subsystem includes digitizers at various locations in the instrument to convert the thermistor signals from analog to digital and output them to the internal computer. Thermistors are variable resistors whose resistance

changes with their physical temperature. For HAMMR, 5 kΩ thermistors from US Sensor are used. The relationship between their resistance and the physical temperature is provided by the manufacturer [18]. The thermistors measure the physical temperature at many points throughout the HAMMR system, which is important to ensure that none of the subsystems are overheating and to account for the effect of the physical temperature on the performance of the radiometers (including gain and noise figure of each channel) and subsystems. The signals from the thermistors are digitized by five Superlogic's 8017 Analog-to-Digital Converters (ADCs) in the HAMMR instrument. The ADCs and thermistors used in HAMMR are shown in Figure 10.

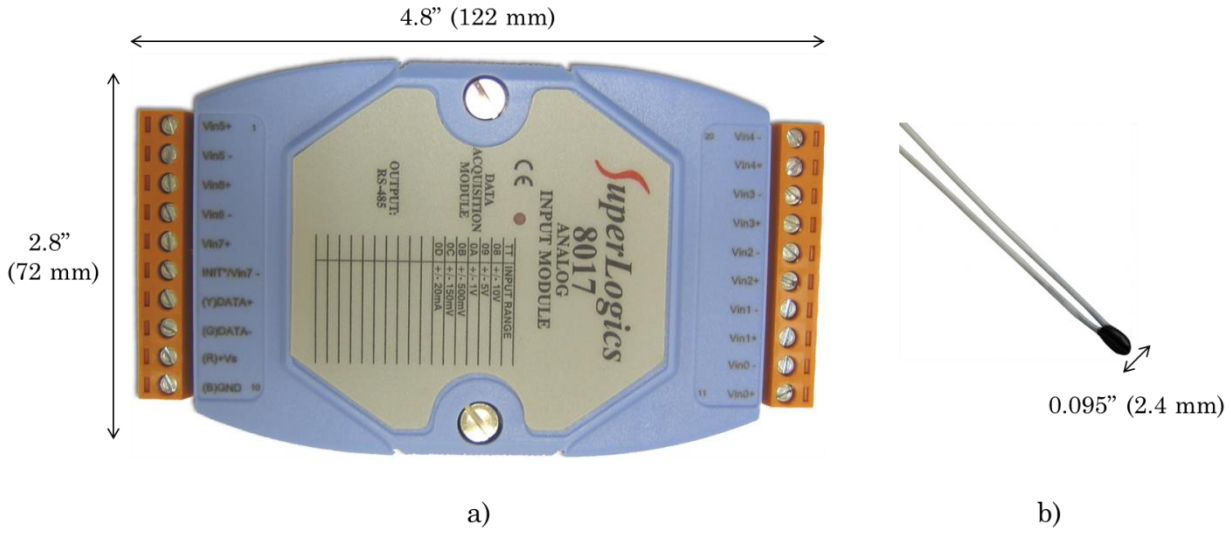

Figure 10: a) Superlogic 8017 Digitizer [18] and b) Thermistor [19]

To record the position of the instrument in latitude, longitude and altitude, as well as its attitude in terms of roll, pitch, and yaw, HAMMR uses a global positioning

system (GPS) receiver and inertial measurement unit (IMU). The GPS receiver measures the latitude and longitude of the instrument, and the IMU measures the roll, pitch, yaw, and altitude. The latitude, longitude, attitude and altitude of the instrument are needed to determine the scene that is observed by the radiometers (i.e. whether the radiometer is viewing land or water surface). For this reason, the IG-500N from SBG Systems, shown in Figure 11, is used in the HAMMR system to measure roll, pitch and yaw precisely, i.e. to within 0.45°, and latitude, longitude and altitude to within 3 meters [20].

Figure 11: SBG Systems IG-500N GPS IMU [20]

The signal conditioning and digitizing portion of the radiometer system consists of the analog back-end board (ABEB) as well as the digital back-end board and FPGA [21]. The ABEB integrates and digitizes the analog signals output by the radiometers. The digital back-end consists of a custom-designed buffer board and a BeMicro SDK field programmable gate array (FPGA) [22]. The buffer board routes

all of the input and output signals to and from the FPGA, respectively. It also acts as a buffer between the ABEB and internal computer. The FPGA sends control signals to the noise sources, Dicke switches, analog back-ends and the flat-reflector scanning motor. The ABEB, buffer board, and FPGA are shown in Figure 12.

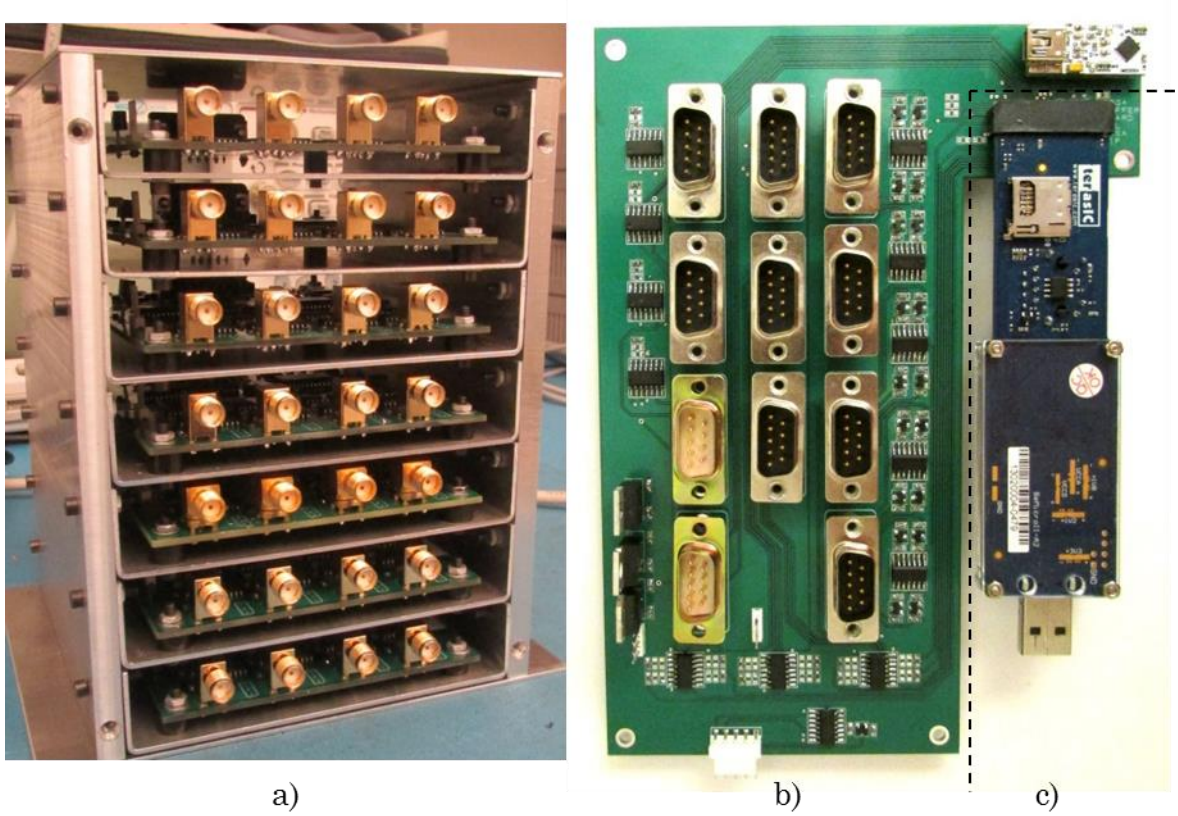

Figure 12: a) ABEB Stack in Internal Chassis, b) Buffer Board and c) FPGA [21]

An internal computer controls the FPGA and stores the signals from the back-end, thermistors, GPS/IMU and motor encoder. The HAMMR internal computer, MXE-5301 from Media Wave PC, Inc. was chosen based on its ruggedness, size, and performance [23]. The internal computer is shown in Figure 13.

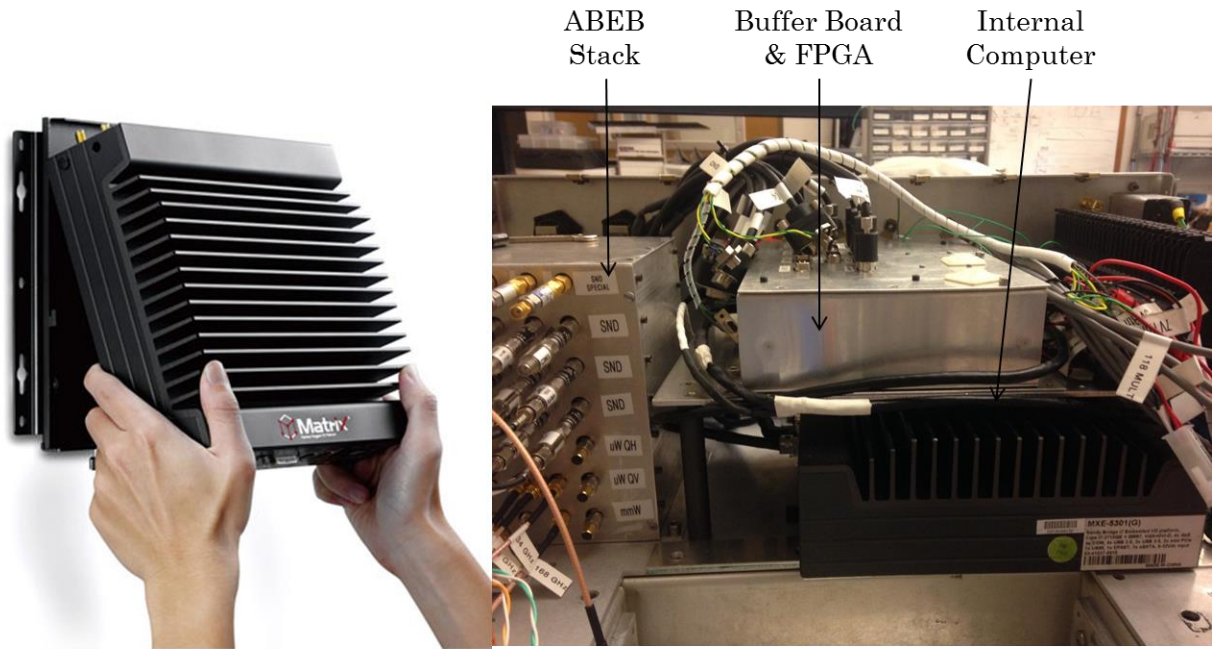

Figure 13: a) MXE-5301 Internal Computer [23] and b) Internal Computer Mounted in HAMMR

A thermal control system, consisting of a thermal controller and TO-220 power resistors, is used to maintain the high-frequency radiometers near a fixed temperature. It is especially important to control the temperature of these radiometers since they are located closest to the aperture of the HAMMR system and may be prone to thermal gradients caused by air flow in the cavity. The thermal controller is a dual-zone, proportional-integral-derivative (PID) thermal controller from Omega Engineering, shown in Figure 14 [24]. It independently regulates the physical temperature of the millimeter-wave window and sounding radiometers. The TO-220 power resistors, located near the radiometers, are switched on and off by the thermal controller as needed to maintain the set temperature (near room temperature of 300 K) for each zone [25].

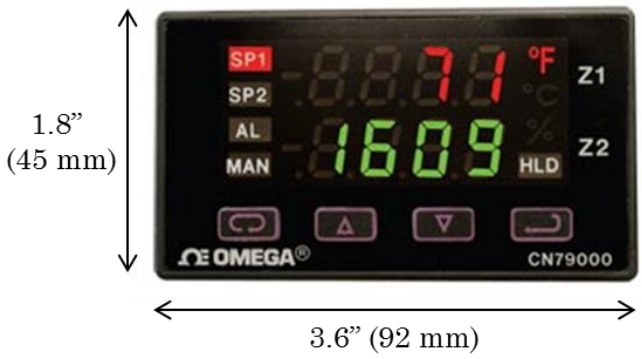

Figure 14: CN79000 Dual-Zone Temperature Controller [24]

All of HAMMR's subsystems are powered from standard 120 V, 60-Hz alternating-current (AC) power. The AC power is rectified into direct current (DC) by HAMMR's internal power supplies before being distributed to the subsystems.

3.1.2 HAMMR Chassis and Assembly

An outer chassis houses the radiometers and subsystems of the HAMMR instrument and is used to interface the instrument with an aircraft. The outer dimensions of the chassis are 31” x 29” x 21” (78 x 74 x 53 cm) and were determined by the size of the port in the Twin Otter aircraft that the HAMMR instrument would be mounted in as well as to ensure that HAMMR fits into the nose pod of a Global Hawk Unpiloted Airborne Vehicle (UAV). A side view of the physical computer aided design (CAD) model of the HAMMR chassis and internal components is given in Figure 15.

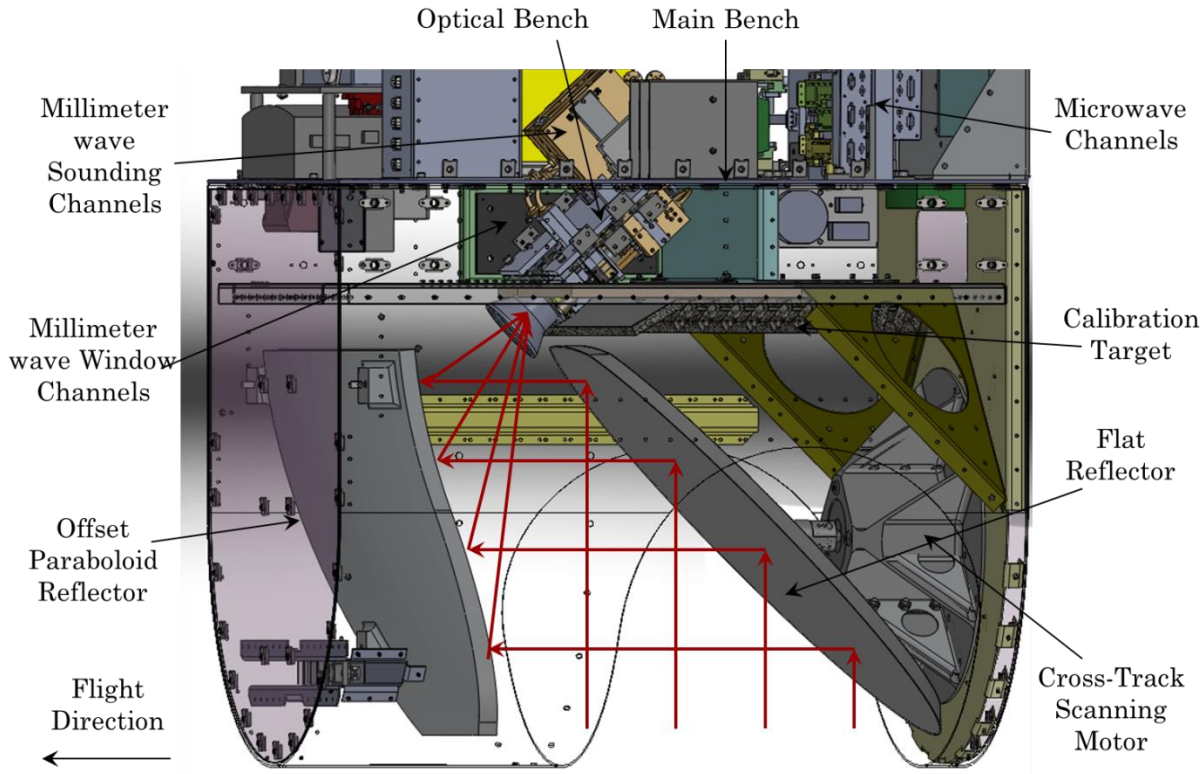

Figure 15: Side View of HAMMR CAD Model in Nadir-Viewing Position

The flat reflector is positioned at the aperture of the HAMMR instrument and is angled to reflect the incoming atmospheric emissions onto the offset parabolic reflector when within approximately ±60° of the nadir direction. The calibration target is mounted directly above the flat reflector so that its emission is reflected onto the offset parabolic reflector when within approximately ±40° of the zenith direction. The parabolic reflector is mounted opposite to the flat reflector and focuses the reflected radiation onto the three radiometer feed horns on the optical bench.

All three radiometer feed horns as well as the millimeter-wave window and sounding channels are mounted on the optical bench. As shown in Figure 15, the optical bench is mounted at an angle with respect to the main bench. This angle was determined by the alignment of the bore sight directions of the feed horns with the foci of the offset parabolic reflector. The rest of the subsystems are mounted to the main bench and are arranged as shown in Figure 16.

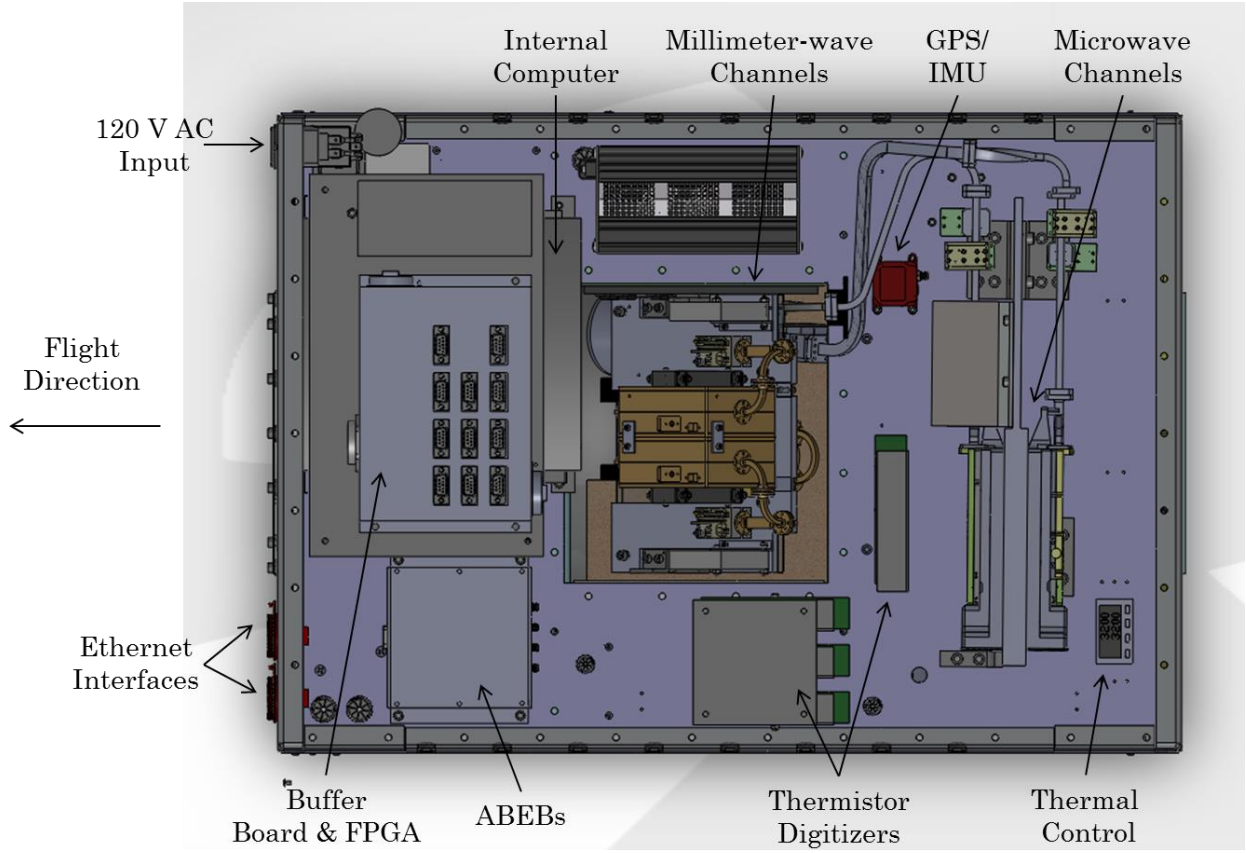

Figure 16: Top View of HAMMR Solidworks Model

The components on the main bench include the microwave channels, power supplies and distribution, back-end system, GPS/IMU, thermistor ADCs, thermal control,

and internal computer. The interfaces of the HAMMR instrument are Ethernet and 120 V AC to the external computer and power input from the aircraft. They are mounted in feed throughs on the front face of the HAMMR instrument. A top lid is mounted above the main bench and closes the HAMMR instrument.

3.2. Microwave Radiometer Channels

The lowest frequency radiometer channels in HAMMR are the microwave radiometer channels from 18-34 GHz. The technology development of the microwave radiometer channels in this IIP-10 project was comparatively minor and was completed at JPL. Therefore, no work was completed for this thesis in the development of the microwave radiometer channels. The microwave radiometer is discussed in some detail in this section.

3.2.1 Microwave Radiometer Overview

The microwave radiometer frequency set has six channels with center frequencies of 18.7, 23.8, and 34.0 GHz that measure both quasi-horizontal (QH) and quasi-vertical (QV) polarization. The cross-track scanning rotates the polarization basis during the scan. Therefore, the two orthogonal polarizations are not always H and V. The purpose of including the microwave radiometer channels in the HAMMR instrument is to have a set of accurate brightness temperature measurements that are well understood from experience with the Advanced Microwave Radiometer (AMR) instrument on OSTM/Jason-2. Well-characterized algorithms have been

developed to retrieve wet-tropospheric path delay from Jason-1 and Jason-2 microwave radiometer brightness temperature measurements. The HAMMR microwave radiometer brightness temperature measurements will be used to determine the capability of and potential for improvement in spatial resolution from the new mm-wave window channel radiometer measurements.

The 23.8 GHz channel is near the water vapor absorption line of 22.235 GHz, and is one of the least sensitive frequencies to pressure broadening of this absorption line [26]. Therefore, it is often used to determine integrated water vapor in coordination with other channels, such as 31 to 34 GHz. The lowest frequency channel, 18.7 GHz, has the least amount of absorption due to water vapor and, therefore, is more sensitive to the sea surface. It helps the algorithm to compensate for surface effects such as roughening due to wind at the sea surface and other features, including whitecaps. The highest frequency channel, 34.0 GHz, has the greatest absorption due to cloud liquid water of the three channels and is used to correct for non-precipitating clouds [27]. Additionally, both QV and QH polarizations are measured at all three frequencies. The ratio of the polarized brightness temperatures helps to validate the off-nadir sea surface microwave emission using well-understood models that take into account the sea surface wind speed and related factors [28].

3.2.2 Microwave Radiometer Block Diagram

The microwave radiometer channels are direct-detection Dicke radiometers, as shown in the block diagram in Figure 17. The feed horn input to the radiometer is followed by an orthomode transducer (OMT) which separates the QV and QH polarizations. The microwave radiometer feed horn and OMT assembly was purchased from Microwave Engineering Corporation (MEC) [29].

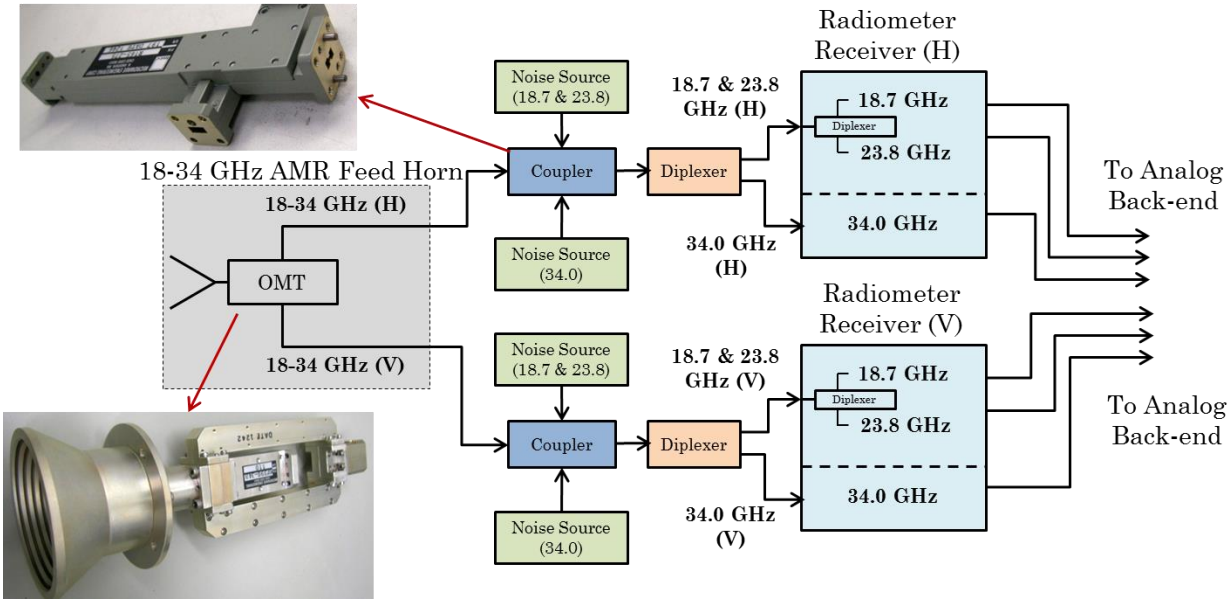

Figure 17: Microwave Radiometer Channel Block Diagram [30]

A directional coupler is used to couple in the outputs of two noise sources, one for 18.7 and 23.8 GHz and the other for 34.0 GHz. The noise sources are used for internal calibration to establish a linear relationship between output voltage and measured antenna temperature in addition to determining the noise of the receiver. The signal is then split by a diplexer into two waveguide bands, WR-42 for 34.0 GHz

and WR-28 for 18.7 and 23.8 GHz. These two output signals are then input into their respective receivers. The QH and QV receivers are identical. A populated receiver is shown in Figure 18.

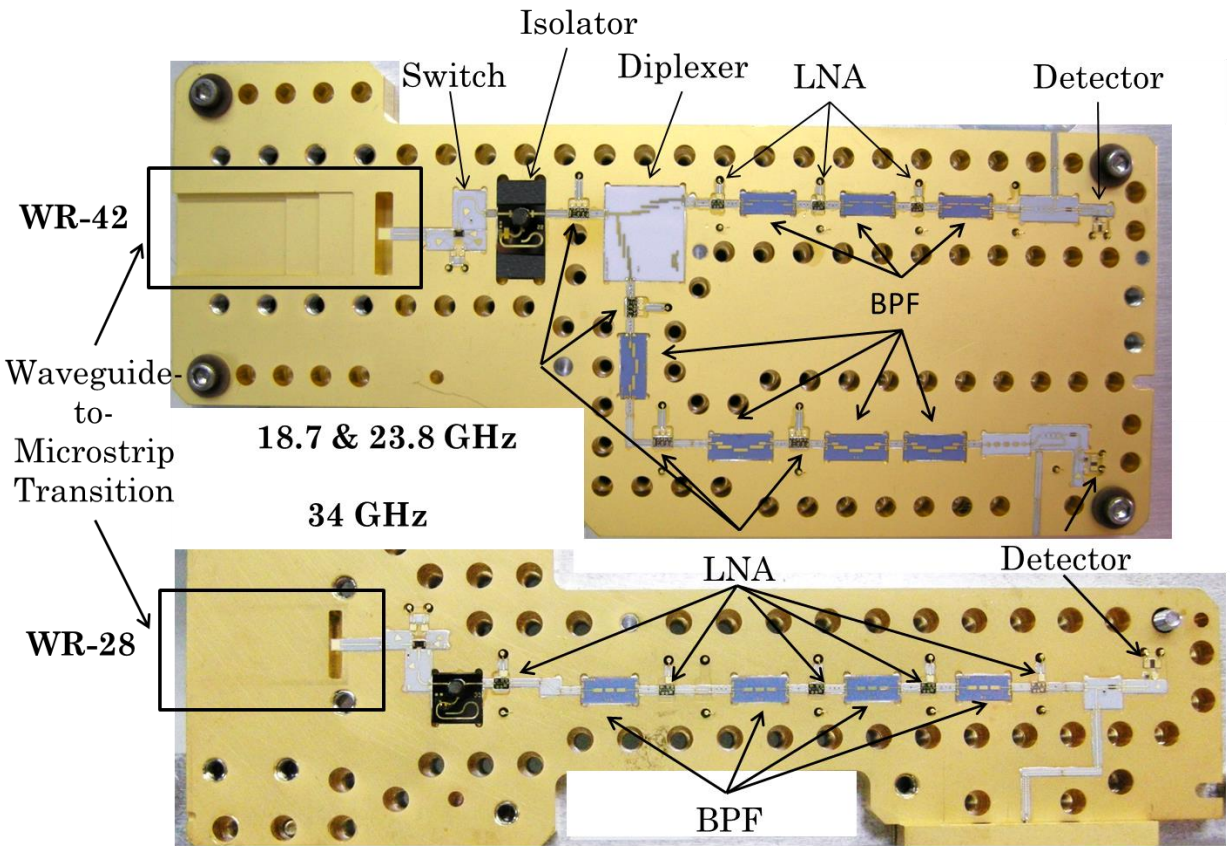

Figure 18: Populated Microwave Radiometer Channel Receiver [30]

After the signal is converted from waveguide to microstrip, it is input to a Dicke switch. Band pass filters (BPF) are added between the LNAs for band limiting to avoid saturation. The insertion loss of the BPFs also helps to set the correct power level for the detector diodes. The detector diodes are at the end of the RF chain. The output of each of the detector diodes is input to a video amplifier, not shown in

Figure 18, for additional amplification at baseband. The outputs of the microwave radiometers are connected to the inputs of the analog back end board (ABEB) using coaxial cables.

3.2.3 Microwave Radiometer Channel Performance

The CAD model in Figure 19 shows the microwave radiometer channels integrated into the HAMMR instrument. The two receivers for each polarization have identical components and are mounted as mirrored images of one another. The only difference between the operation of the radiometers that the QH polarized signal is input into one of them, and the QV polarized signal is input into the other.

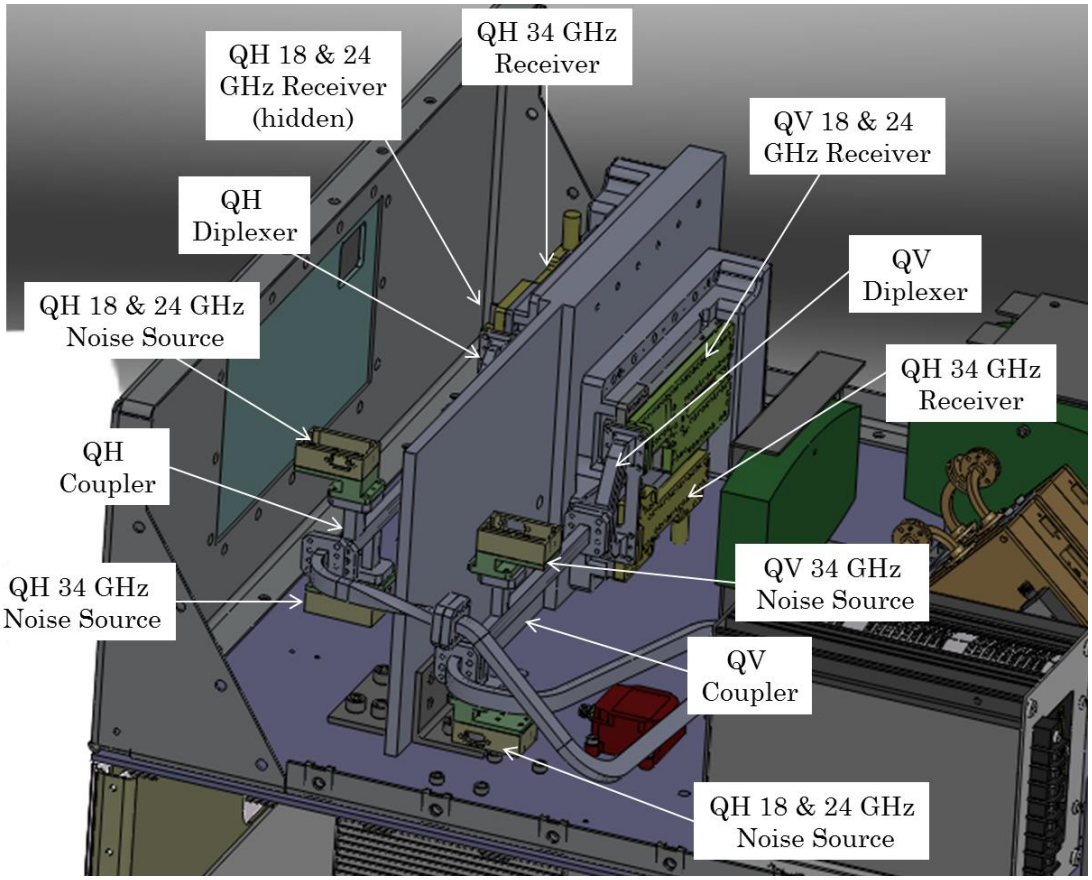

Figure 19: CAD Model of HAMMR Microwave Radiometer Channels

Their measured performance of the QH and QV polarized radiometers is provided below in Table 1 and Table 2, respectively. Because they consist of identical components, which would are expected to differ only due to manufacturing tolerances, the two receivers have nearly the same performance, as expected.

Table 1: QH-Polarization Microwave Radiometer Performance (Measured)

Frequency (GHz)	Receiver Noise Temperature (K)	3 dB Bandwidth (MHz)
18.7	550	192

23.8	570	368
34	620	767

Table 2: QV-Polarization Microwave Radiometer Performance (Measured)

Frequency (GHz)	Receiver Noise Temperature (K)	3 dB Bandwidth (MHz)
18.7	550	187
23.8	570	471
34	620	753

These values are used in determining the radiometric resolution of the radiometers. At the time this thesis was written, the radiometric resolution of the receivers had not been calculated yet.

3.3. Millimeter-Wave Radiometers

There are two sets of high-frequency millimeter-wave radiometer channels in the HAMMR instrument, i.e., the millimeter-wave sounding channels and the millimeter-wave window channels. The technology for these two sets of radiometer channels was developed and implemented as part of the IIP-10 project.

3.3.1 Millimeter-Wave Sounding Channels

The millimeter-wave sounding radiometer has two channel sets near the oxygen and water vapor absorption lines at 118.75 GHz and 183.31 GHz, respectively. The

118.75 GHz frequency set has eleven channels (of which only eight are digitized) at frequencies above the oxygen absorption line at 118.75 GHz. Each channel further away from the oxygen absorption line at 118.75 GHz can penetrate deeper into the atmosphere, resulting in a vertical temperature profile of the scene under observation. The temperature of the atmosphere can be measured on the oxygen absorption line because the volume mixing ratio of oxygen is essentially independent of location and time; therefore, any changes in the measured brightness temperature will be due to changes in the physical temperature of the atmosphere [31]. For this reason, the 118.75 GHz receiver is referred to as the temperature sounder.

Similarly to the 118.75 GHz receiver, the 183 GHz uses eight channels offset at frequencies below the 183.31 GHz water vapor absorption line. Channel frequencies further from 183.31 GHz penetrate deeper into the atmosphere, resulting in a vertical profile of the water vapor content of the atmosphere. For this reason, the 183.31 GHz receiver is referred to as the water vapor sounder. The development of the sounding channels is discussed in Chapter IV.

3.3.2 Millimeter-Wave Window Channels

The millimeter-wave window channels are in the frequency "windows" between the millimeter-wave absorption lines. The three millimeter-wave center frequencies, chosen to have maximum information content on wet-tropospheric path delay, are

90 GHz, 130 GHz, and 168 GHz. These "window" regions are sensitive to integrated water vapor, closely related to tropospheric wet path delay, and much wider bandwidths are available compared to both the microwave and millimeter-wave sounding channels. Although both the microwave and millimeter-wave window channels measure integrated water vapor, their measured brightness temperatures are quite different. This is because the atmosphere has much lower absorption (and therefore emission) due to water vapor in the microwave frequencies than in the millimeter-wave frequencies, as shown in Figure 3. Therefore, the microwave channels will be more sensitive to surface emission than the millimeter-wave channels will. The development and testing of the millimeter-wave window channels is discussed extensively in Chapter IV.

3.4. Twin Otter International Aircraft

The principal goal of the IIP-10 grant is to demonstrate the operation of the HAMMR instrument aboard an aircraft. After consideration of various aircraft that could be used for the airborne demonstration of the HAMMR instrument, the Twin Otter research aircraft was chosen [21].

3.4.1 Twin Otter Aircraft

The Twin Otter is a short takeoff and landing utility aircraft which will be flown at a nominal cruising altitude of 3 km [32]. This will provide 6 km swath for viewing the surface at incidence angles of up to ±45°. A Twin Otter and the cross-track

scanning swath of the HAMMR while it is mounted in the airplane are shown schematically in Figure 20.

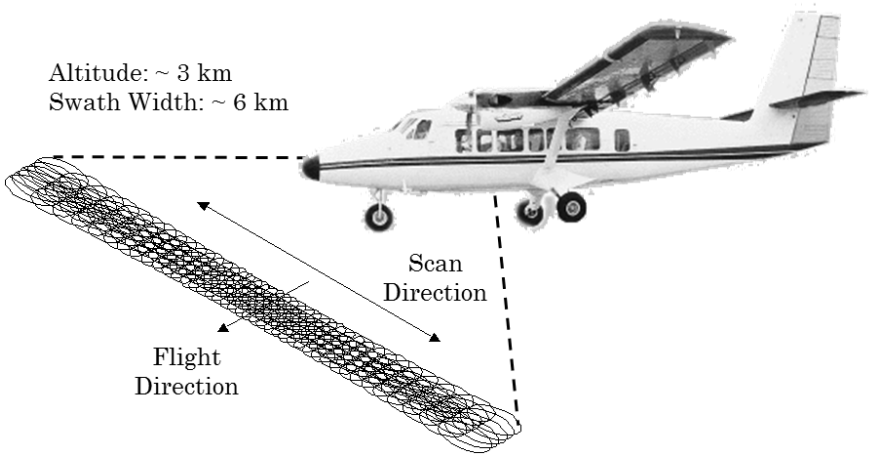

Figure 20: Twin Otter Aircraft Swath [14]

The rotation speed of the flat reflector was chosen as 60 rotations per minute (RPM) to maintain contiguous footprints on the surface at an altitude of 3 km above ground and a cruising speed of 33 m/s (about 65 knots) [21].

3.4.2 HAMMR in a Twin Otter Aircraft

The HAMMR instrument is mounted in a port in the bottom of the aircraft's fuselage. The opening in the instrument chassis is completely outside of the aircraft to avoid obstructing the field of view of the scanning flat reflector. The HAMMR instrument mounted in the Twin Otter aircraft is shown in Figure 21.

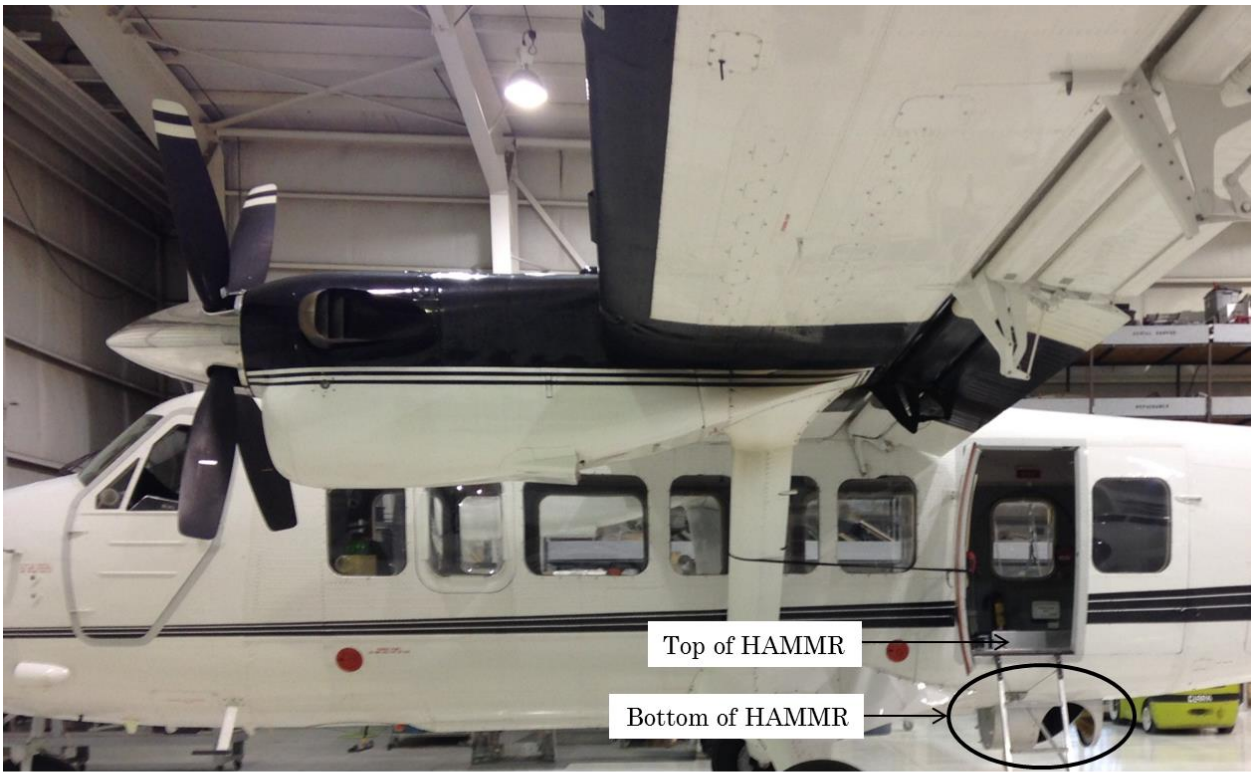

a)

b)

c)

Figure 21: a) HAMMR Instrument Mounted in Twin Otter b) Rear View of HAMMR in Twin Otter Aircraft and c) Side View of HAMMR Mounted in Twin Otter Aircraft

The top of the instrument is mounted in the cabin of the aircraft where most of the electronics can be accessible to the science crew if necessary. The science crew that operates the HAMMR instrument sit in the cabin of the aircraft during flight. CSU team member Thaddeus Johnson is shown in Figure 22 while working on the instrument in the Twin Otter aircraft.

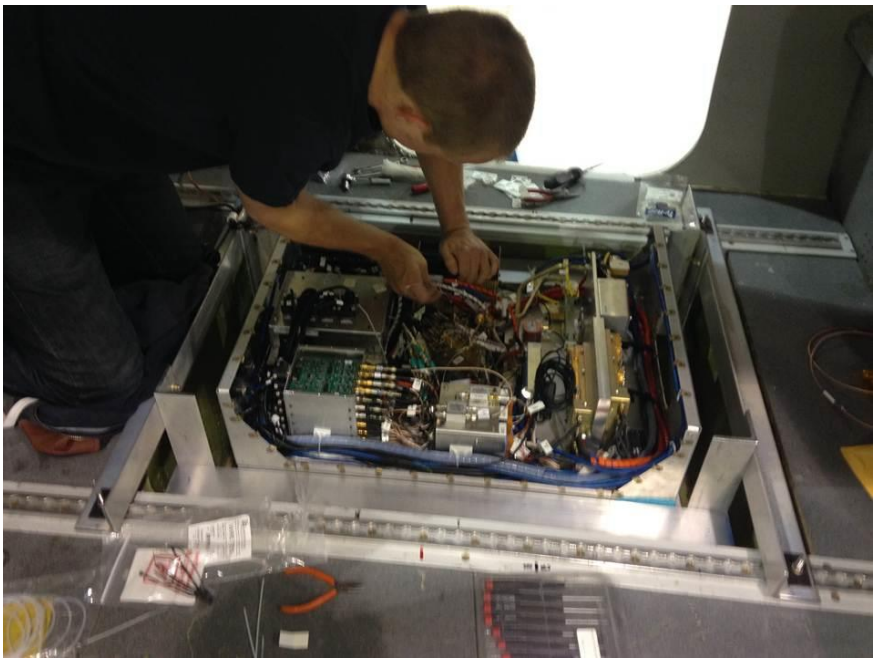

Figure 22: CSU Team Member Thaddeus Johnson working on HAMMR in Twin Otter

The HAMMR instrument was mounted in a Twin Otter aircraft at Twin Otter International in Grand Junction, Colorado on July 8, 2014. Airborne demonstration took place during the subsequent three days from July 9 – July 11, 2014. The process of integration and results from these flights are discussed in Chapter VI.

Chapter IV Millimeter-Wave Sounding Radiometers

The millimeter-wave sounders consist of two radiometers near the oxygen and water vapor absorption lines at 118.75 GHz and 183.31 GHz, respectively. These two sounders provide measurements for retrieval of vertical profiles of physical temperature and water vapor, respectively. These two sounders are commonly referred to as the 118 GHz (temperature) and 183 GHz (water vapor) sounders in this thesis. This chapter discusses the development, integration and initial testing of the millimeter-wave sounding radiometers.

4.1. Millimeter-Wave System Overview

The block diagram of the millimeter-wave sounders is shown in Figure 23. Unlike the microwave radiometer and millimeter-wave window channels, the sounder radiometers have a super-heterodyne topology. The quad-ridge feed horn, designed by JPL as a single antenna for both 118 and 183 GHz receivers, is at the input of the millimeter-wave sounders.

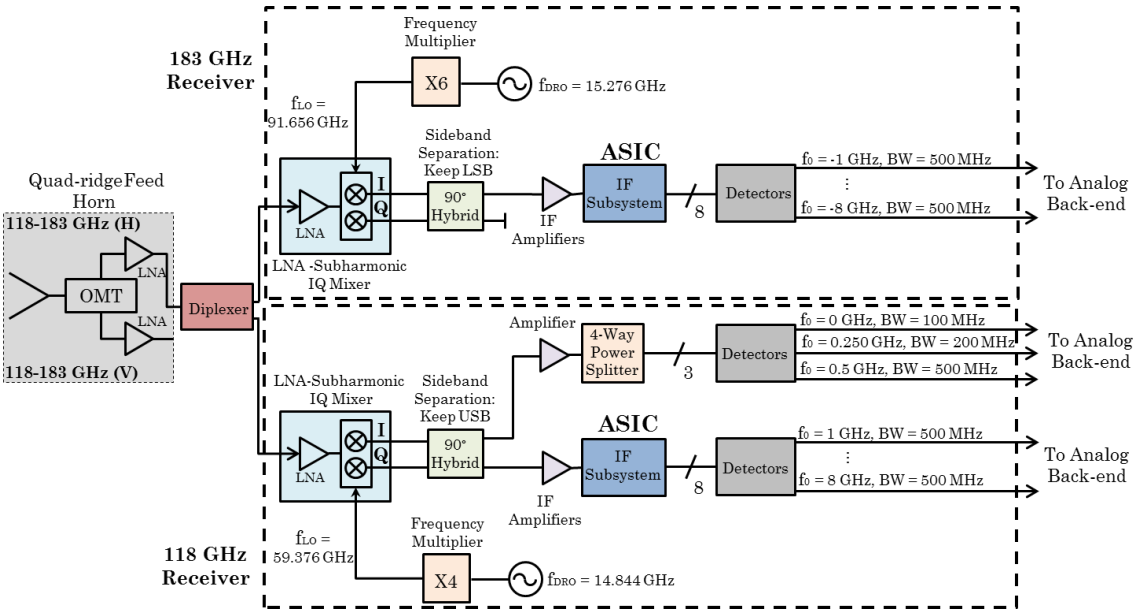

Figure 23: Millimeter-Wave Sounding Radiometer Block Diagram

The quad-ridge horn is connected to a block containing both an orthomode transducer (OMT) and two low-noise amplifiers (LNAs), as shown on the left side of Figure 24. The OMT is a polarization diplexer that splits the signal into horizontally (H) polarized and vertically (V) polarized signals. Each of the H and V polarized signals are then amplified by an LNA. In HAMMR, only one of the two signals is input to the two sounding receivers, and the other output is left disconnected.

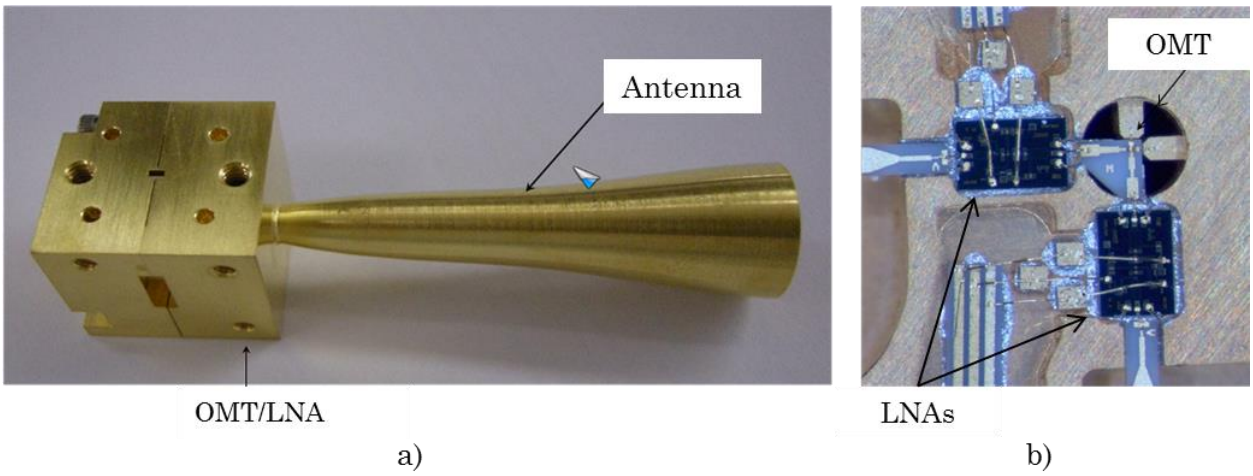

Figure 24: a) Quad-Ridge Horn and b) Inside Quad-Ridge Horn Receiver

The output signal from the quad-ridge horn LNA is split by a waveguide diplexer into the two bands that lie near118.75 and 183.31 GHz. After the signals are split, they are sent to the respective receivers for further amplification, down conversion, and power detection. Although the receivers have different components that operate at their respective frequencies, their functions are identical and the discussion that follows will discuss only one of the modules for clarity.

Once the signal enters the sounder receiver, it is input to a small housing referred to as the miniature monolithic microwave integrated circuit (MMIC) low mass/power radiometer (MIMRAM) [33]. The MIMRAM was developed as part of the Geostationary Synthetic Thinned Aperture Radiometer (GeoSTAR) IIP project and is shown in Figure 25.

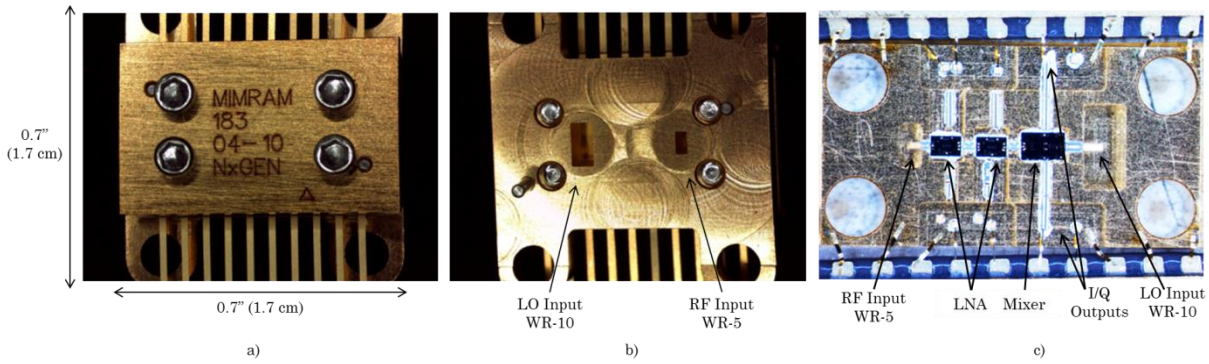

Figure 25: a) Top of 183 GHz MIMRAM b) Bottom of 183 GHz MIMRAM c) Populated 183 GHz MIMRAM

The MIMRAM has two inputs: the RF input from the quad-ridge horn and the local oscillator (LO) input for the sub-harmonic IQ mixer. In between the RF and LO inputs are the MMIC components, i.e. two RF LNAs and the sub-harmonic IQ mixer used for down-conversion. The mixer produces a double side-band signal (DSB); however, the 118 GHz receiver only uses the upper side band (USB) and the 183 GHz receiver only uses the lower side band (LSB). It is desired to remove the unused sidebands since they could add unwanted noise to the system. To remove the unused sideband for each receiver, the sub-harmonic IQ mixer first splits the signal into two outputs 90° out of phase with each other [9]. The IQ outputs are output from the MIMRAM to the IF board, shown in Figure 26.

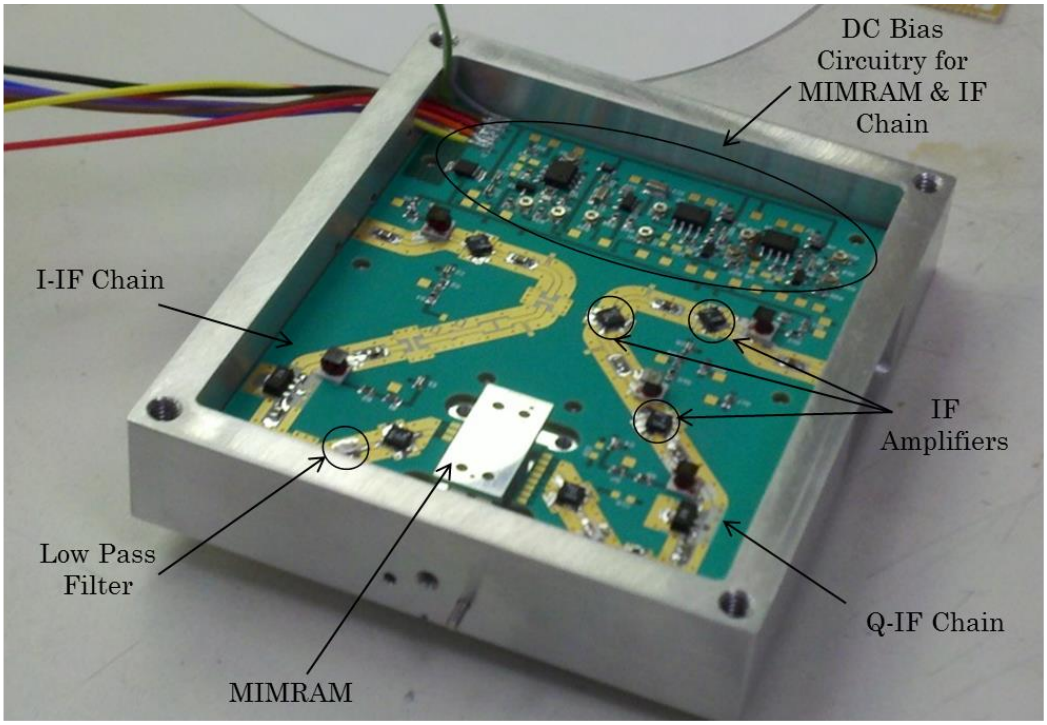

Figure 26: Millimeter-Wave Sounder Radiometer IF Board

There are two identical IF chains, one for the I signal and the other for the Q signal. Each IF chain has a low pass filter and three IF amplifiers. At the output of the IF board, the signals travel equal lengths to a 90° hybrid coupler [34]. The 90° hybrid coupler achieves image rejection through phase cancellation of the I and Q signals resulting in two single sideband (SSB) signals (one USB, one LSB) at the two outputs of the 90° hybrid coupler. Depending on which sideband is used for the respective sounding radiometer, the corresponding output of the 90° hybrid coupler is sent to the application-specific integrated circuit (ASIC) spectrometer.

The ASIC spectrometer was developed by Prof. Behzad Razavi of the University of California Los Angeles (UCLA) as part of the IIP-10 project. The ASIC divides the

spectrum of the output signal from the hybrid coupler into eight frequency bands that are offset in increments of 1 GHz from the center frequencies of 118.75 and 183.31 GHz, as shown in Table 3 and Table 4, respectively.

Table 3: Temperature Sounding ASIC Offset Channel Frequencies

Frequency Set	Channel	Offset Frequency
118.75 GHz	1	+1 GHz
	2	+2 GHz
	3	+3 GHz
	4	+4 GHz
	5	+5 GHz
	6	+6 GHz
	7	+7 GHz
	8	+8 GHz

Table 4: Water Vapor Sounding ASIC Offset Channel Frequencies

Frequency Set	Channel	Offset Frequency
183.31 GHz	1	-1 GHz
	2	-2 GHz
	3	-3 GHz
	4	-4 GHz
	5	-5 GHz
	6	-6 GHz

	7	-7 GHz
	8	-8 GHz

Band definition filters of 500 MHz width are used at the ASIC outputs, followed by attenuators to set the power level so that the detector diodes that follow operate in the square-law region. The detected signals are input to the back-end system to be integrated, digitized, and stored.

As mentioned previously, the 118 GHz sounder has eleven channels, of which only eight are output from the ASIC. The other three channels come from the previously unused output of the 118 GHz 90° hybrid coupler. This output of the 90° hybrid coupler is divided into three signals using a power divider, and each is filtered to yield three additional channels with offset frequencies of 0 GHz, 0.25 GHz and 0.5 GHz above the 118.75 GHz absorption line. Because only eight channels can be digitized by the ABEB for each sounding radiometer, three channels from the ASIC with least information content are chosen to remain unused.

4.2. Waveguide Diplexer

The quad-ridge horn is used for both the 118 and 183 GHz sounding radiometers. Before the signal is sent to its respective receiver, it needs to be separated into its two bands. To accomplish this, a diplexer is used directly after the quad-ridge horn.

4.2.1 Previous Work

The tri-frequency horn from the mm-wave channels has an integrated triplexer to divide the 90, 130 and 168 GHz channels and output them in WR-10, WR-08 and WR-05 waveguide outputs, respectively. Shown in Figure 27, the 90 GHz band first is divided from the incoming signal. Then a diplexer is used to divide the remaining two channels centered at 130 and 168 GHz.

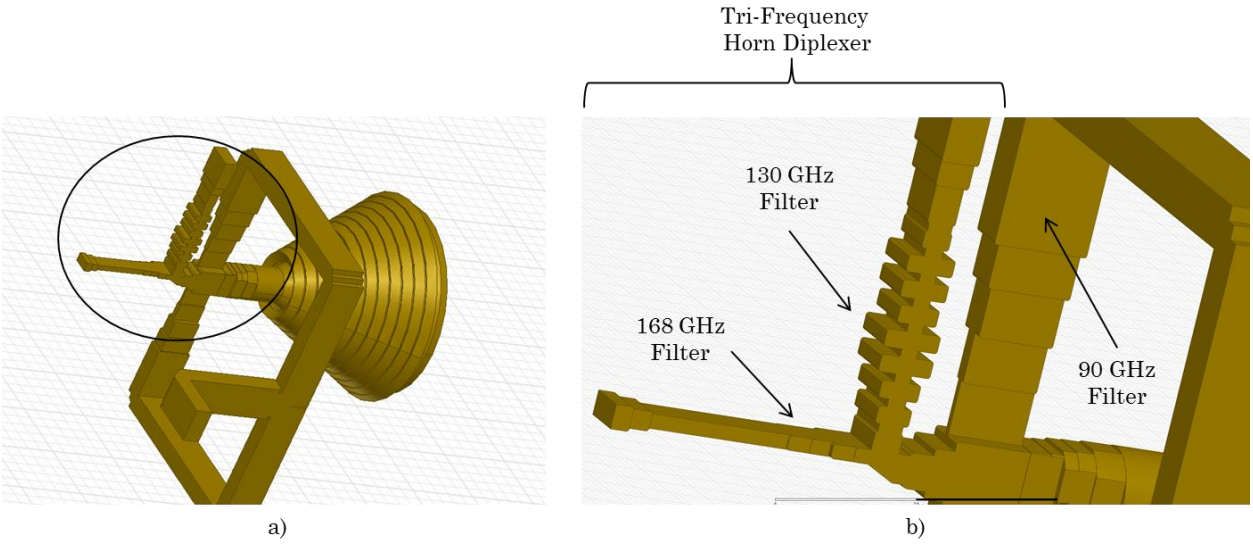

Figure 27: a) Triplexer in Tri-Frequency Horn and b) Close up of Diplexer Section of Tri-Frequency Horn

Because 130 GHz is similar in wavelength to 118 GHz and 168 GHz is similar in wavelength to 183 GHz, the diplexer from the tri-frequency horn was used as an initial design for the 118/183 GHz diplexer.

4.2.2 Diplexer Performance Goals

The diplexer has two outputs whose performances need to be considered separately. The diplexer separates two frequency bands of 116 – 124 GHz (8 GHz bandwidth) and 174 – 184 GHz (10 GHz bandwidth). The two waveguide outputs are WR-6 for the 118 GHz band and WR-5 for the 183 GHz band. Within each of the bands, it is desired to have a low insertion loss. Insertion loss values in the bands over 1 dB are acceptable; however, it is desired to still minimize these losses.

Because the diplexer separates the signals in these two frequency bands, the insertion loss outside each of their respective bands should be very high. A goal of 40 dB insertion loss was set for the frequencies in the other band, i.e. 174 – 184 GHz for 118 GHz and 116 – 124 GHz for 183 GHz. This ensures that only the correct frequency band gets to the respective output and any other signals are sufficiently attenuated.

With only one input to the diplexer, high return loss is required, resulting in minimal reflections back into the quad-ridge horn. The goal for the return loss was greater than 15 dB in both of the two frequency bands of 116 – 124 GHz and 174 – 184 GHz. Outside of these two bands the return loss should be as close as possible to 0 dB.

4.2.3 Diplexer Tuning and Design Changes

The design of the 118/183 GHz diplexer started from the diplexer in the millimeter-wave window channels' tri-frequency horn. The design file was provided by JPL to be simulated in ANSYS's High Frequency Structure Simulator (HFSS) software. The powerful software uses the finite element numerical method to model a design's physical structure and predict its performance [35]. The HFSS simulated response of the initial diplexer design in the tri-frequency horn is shown in Figure 28.

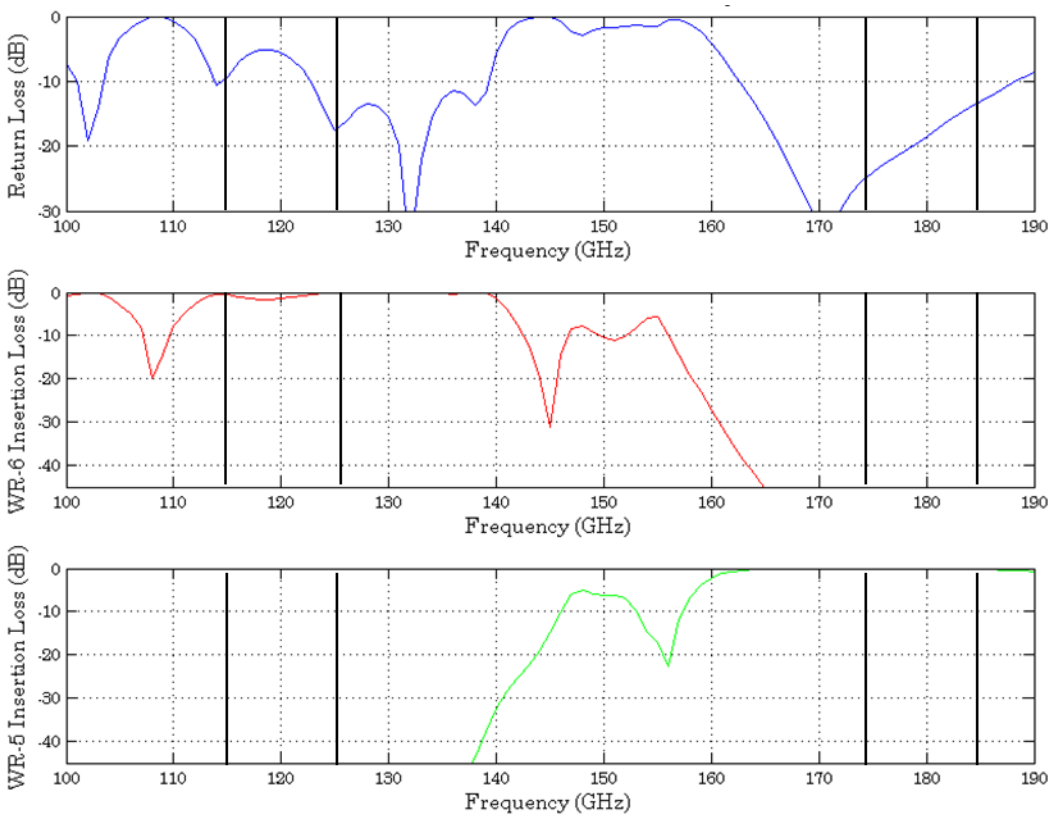

Figure 28: Simulated Performance of Millimeter-Wave Window Channel Tri-Frequency Horn Diplexer

The diplexer design in the tri-frequency horn is a good starting point to accomplish

the design goals of the mm-wave sounder radiometer diplexer. All of the goals were met for the water vapor sounding band, the temperature sounding band needed further tuning. The tri-frequency horn diplexer performance lower band return loss is centered almost 15 GHz higher than what is required for the temperature sounding frequency band and has unacceptably low return loss, less than 10 dB, from 110 – 123 GHz. Additionally, the insertion loss is higher at 118 GHz than anywhere else in the lower passband from 113 – 143 GHz.

All of the hand tuning was done on the lengths between the resonant and coupling cavities on the lower frequency filter. Referencing Figure 29, the spacing between the coupling cavities, l_1, should be one half of the wavelength at center frequency and the spacing between the resonant cavities, l_2, should be one quarter wavelength at center frequency [36]. These two distances essentially set the center frequency of the lower frequency arm of the diplexer.

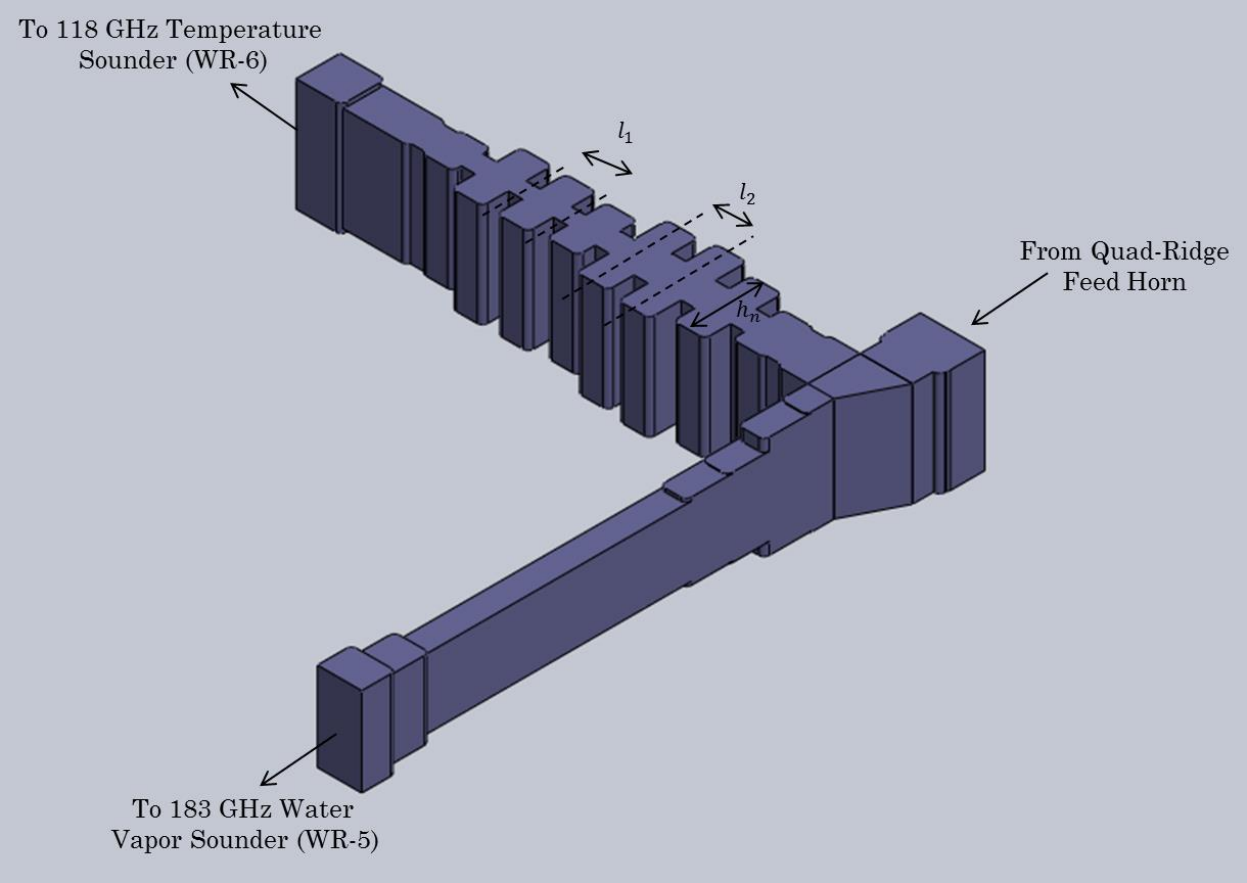

Figure 29: Millimeter-Wave Sounding Radiometer Diplexer Tuning

The two arms and discontinuities in the diplexer introduce parasitic reactances that have to be accounted for. Because of this, l_1 and l_2 are not exactly a half wavelength and a quarter wavelength at center frequency, respectively. Additionally, the heights of the resonant cavities, h_n, were tuned to achieve the performance goals and to account for these parasitics. After hand tuning of these three parameters was exhausted, the HFSS optimization tool was used to further improve the performance.

Other design changes were done on the original diplexer to accommodate the needs of the millimeter-wave sounding radiometers. The lower-frequency arm of the original design had a WR-8 waveguide output and this was modified to be a WR-6 waveguide output to interface with the temperature sounding radiometer. Additionally, the waveguide output of the quad-ridge horn has non-standard waveguide dimensions of 0.059" x 0.037" (1.52 x 0.94 mm). To avoid reflections as a result of mismatched waveguide sizes, the input waveguide dimensions of the newly designed diplexer matched the output waveguide dimensions of the quad-ridge horn. This allowed the diplexer to be mounted directly to the quad-ridge horn. The final, machined diplexer is shown in Figure 30.

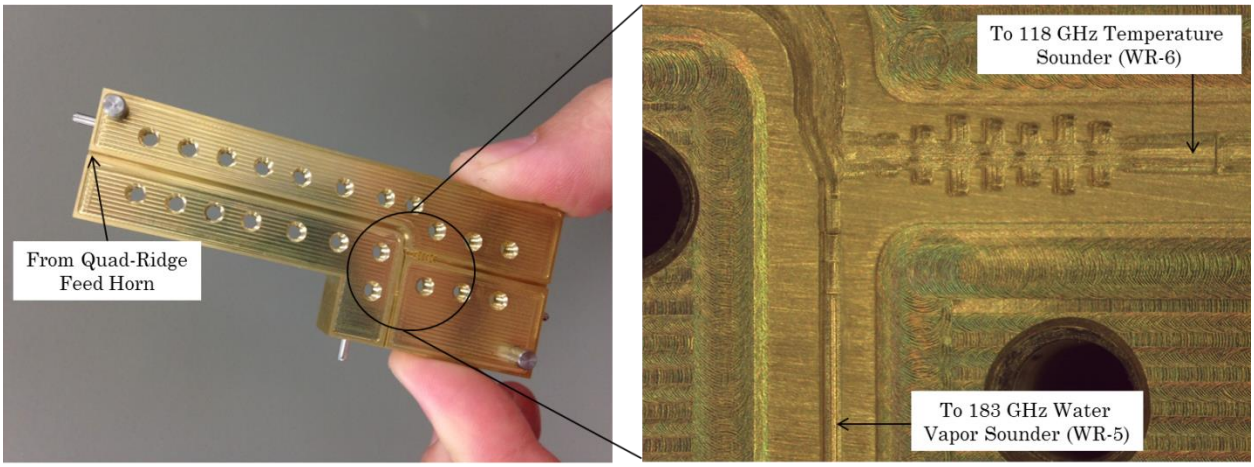

Figure 30: a) mm-Wave Machined Diplexer and b) Zoomed Image of mm-Wave Machined Diplexer

The diplexer was machined out of brass by Zen Machine and then gold plated [37]. As seen in Figure 30, the physical structure of the diplexer takes up only a small portion of the diplexer compared to the lengths of waveguides added to the input

and outputs. These lengths were added to facilitate a more simple assembly the mm-wave sounding radiometers.

4.2.4 Millimeter-Wave Diplexer Performance

The MSL team traveled to JPL in August 2013 to assist with system characterization, including the mm-wave diplexer. Because the diplexer spanned two different electronics industry standard (EIA) standard waveguide dimensions, two different vector network analyzers (VNAs) had to be used to measure the performance over the whole range. The test set up used to measure the performance of the lower frequency temperature sounding band is shown in Figure 31.

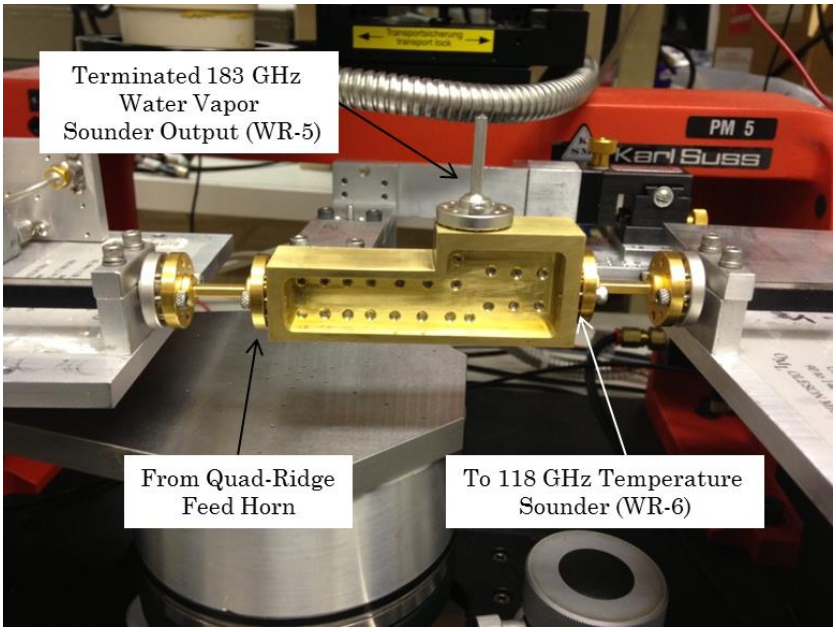

Figure 31: Test Bench to Measure mm-Wave Temperature Sounding Band Diplexer Performance

The measurements done with both VNAs were combined in Figure 32 to show the performance of the mm-wave diplexer over both frequency bands.

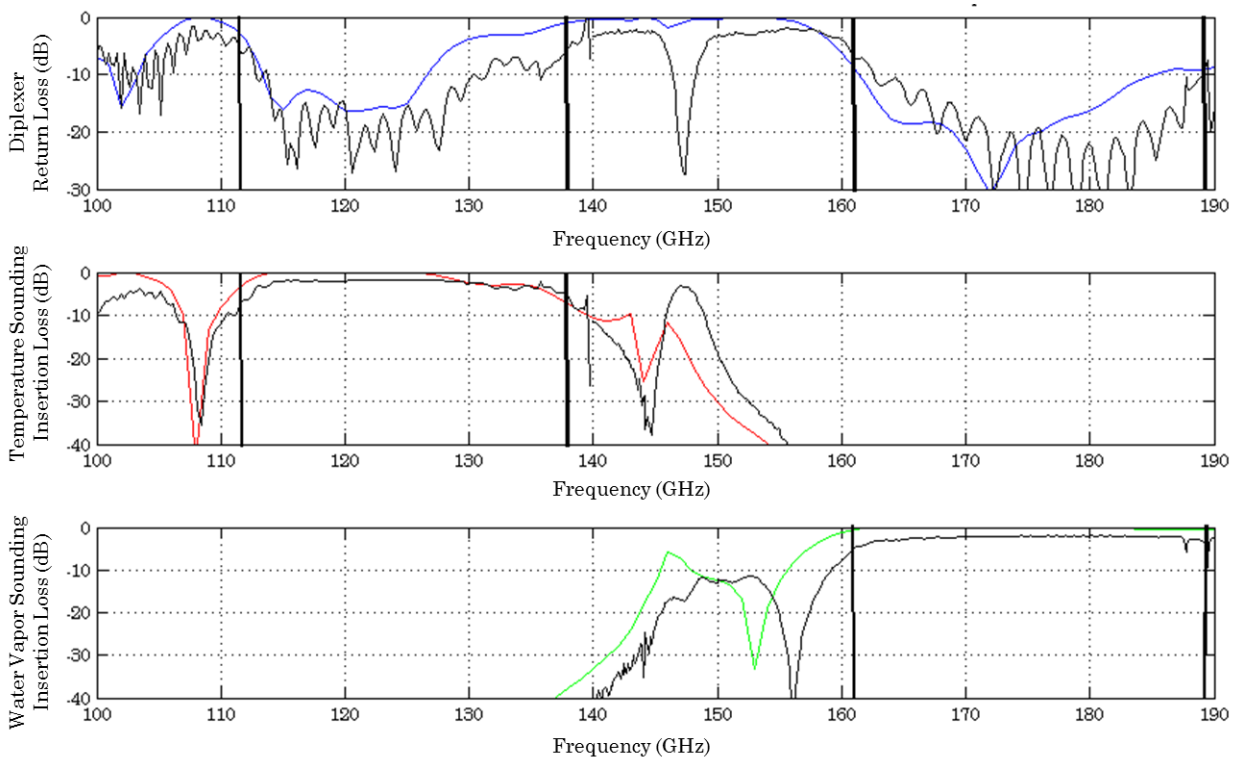

Figure 32: mm-wave Sounding Radiometer Diplexer Measured (black) vs. Simulated (in color) Performance

The measured performance of the diplexer matched the simulated performance of the diplexer very well. The measured return loss of the diplexer had significant ripples that were not seen in the simulated performance. These ripples are believed to be caused by the mismatched waveguide sizes between the input of diplexer and the VNAs. The average performances over both bands are summarized in Table 5.

Table 5: mm-Wave Diplexer Average Measured Performance

Millimeter-Wave Sounding Radiometer	Average Insertion Loss (dB)	Average Return Loss (dB)
Temperature Sounding Band (116 - 124 GHz)	1.9	19.4
Water Vapor Sounding Band (174 - 184 GHz)	2.1	27.3

The average return loss for both bands was greater than 15 dB and the average insertion loss was close to 2 dB which was more than acceptable for the sounding radiometers. Additionally, it can be seen in Figure 32 that 40 dB insertion loss was well exceeded for the frequencies within the other band of each channel, i.e. 174 – 184 GHz for 118 GHz and 116-124 GHz for 183 GHz.

4.3. Design of the 118 GHz MIMRAM

The 183 GHz MIMRAM had been previously designed as part of GeoSTAR, so the design of the 118 GHz MIMRAM was based on the completed 183 GHz MIMRAM. There are four parts that make up the MIMRAM module, as shown in Figure 33.

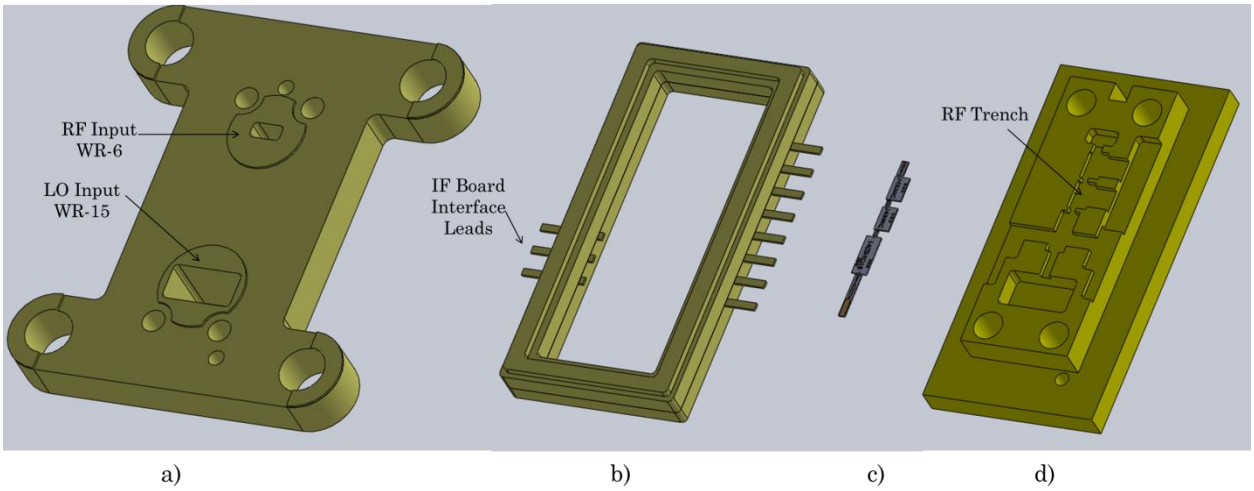

Figure 33: a) 118 GHz MIMRAM Lid, b) 118 GHz MIMRAM Lead Frame, c) 118 GHz MIMRAM RF Receiver Chain, and d) 118 GHz MIMRAM Carrier

The lead frame and MMIC components were designed by JPL and the MIMRAM lid and carrier were designed as part of this thesis. The lid of the MIMRAM interfaces with the RF and LO waveguide inputs from the sounding receiver modules. A circular pressure ridge surrounds each of the waveguide interfaces to ensure a good seal at the junction. The lead frame sits in between the lid and carrier and has leads which are used to interface the outputs of the sub-harmonic I-Q mixer to the IF board and to connect the biasing circuitry on the IF board to the two LNAs and mixer. The MIMRAM carrier contains the RF trench which "carries" the receiver chain MMIC components. The receiver chain, shown in Figure 34, consists of two waveguide-to-microstrip transitions, two LNAs, and the sub-harmonic I-Q mixer.

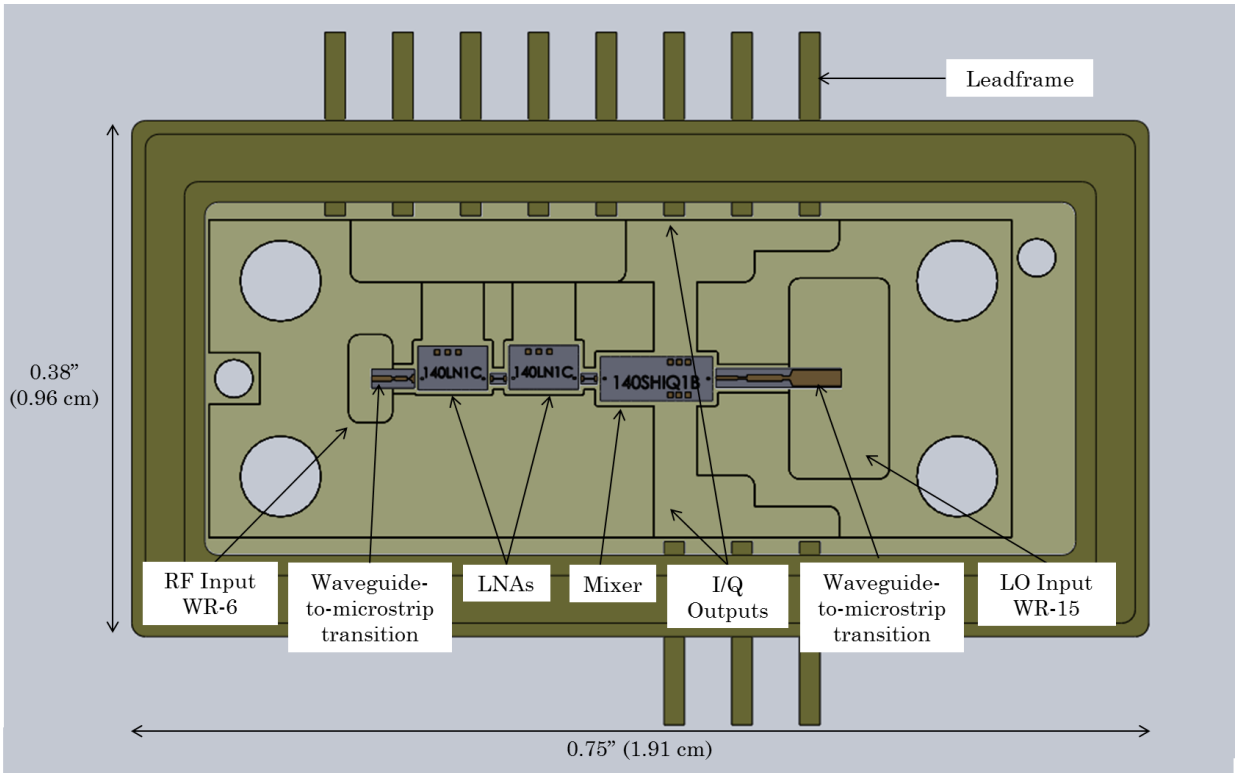

Figure 34: CAD Model of Populated 118 GHz MIMRAM Carrier

The locations of the components and input waveguides were determined by the interfaces between the MIMRAM, IF board, and 118 GHz sounder module. The assembled MIMRAM is mounted with the IF board as shown in Figure 35.

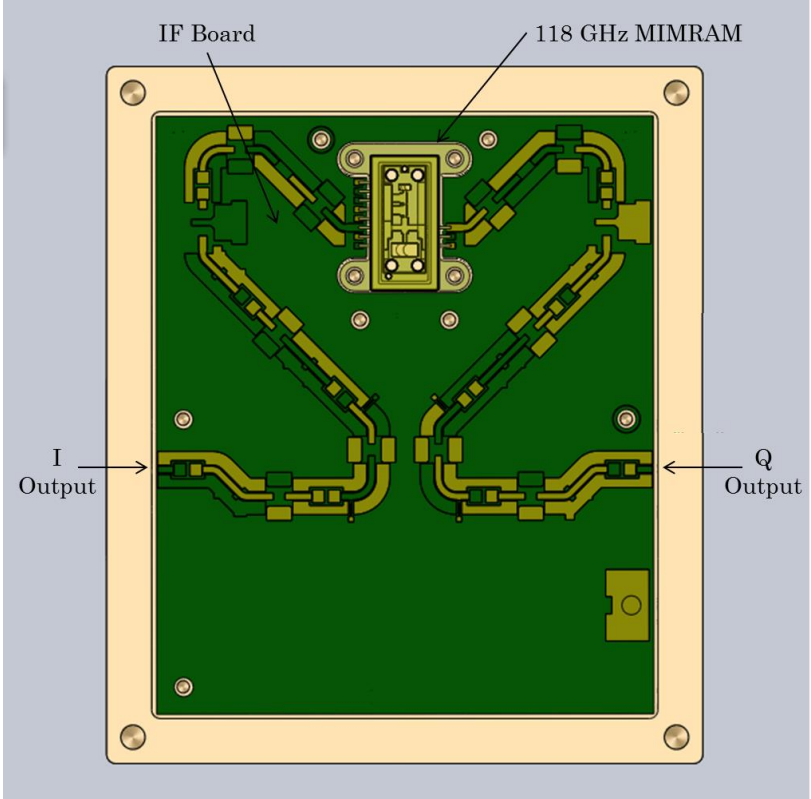

Figure 35: 118 GHz MIMRAM and IF Board

Once the physical MIMRAM design was completed in Solidworks, a computer aided design (CAD) software, it was machined by Zen Machine and populated at JPL.

4.4. Millimeter-Wave Sounder Radiometer Design

The design of the mm-wave sounding radiometers was largely influenced by the minimum size needed to accommodate the IF and ASIC PCBs, how the receivers would be integrated with the rest of the system, and the space available for the recivers in the HAMMR system. This section discusses these design limitations and the final implementation of the mm-wave sounding radiometers.

4.4.1 Millimeter-Wave Sounding Receiver Design

The size of the mm-wave sounding radiometers was largely determined by the space needed to accommodate the IF PCBs which have identical outer dimensions for the two frequency bands. Because of this, the mm-wave sounding receivers are the same size and the temperature sounding band receiver, which is also representative of the water vapor sounding receiver, is shown in Figure 36.

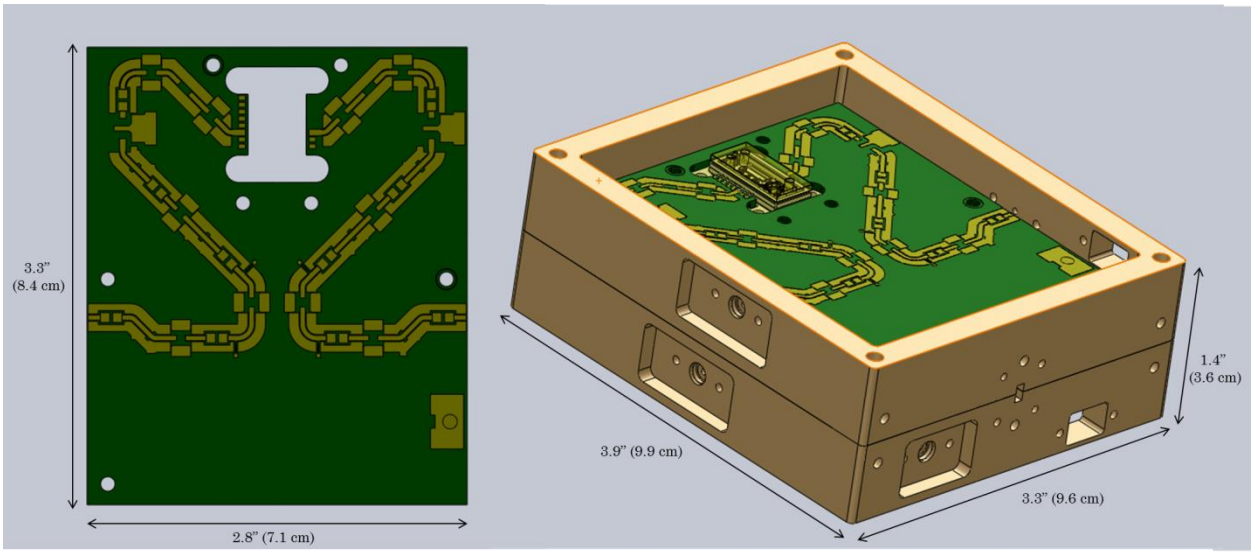

Figure 36: a) 118 GHz IF Board Dimensions and b) 118 GHz Temperature Sounder Receiver Measurements

The locations of other design features of the mm-wave sounding receivers, such as the micro-D and SMA interfaces, were designed to for a simple assembly between the sounding receivers and external components that make up the radiometers.

4.4.2 Millimeter-Wave Sounder Optical Bench Components

Many components external to the mm-wave sounding receivers were needed to complete the mm-wave sounding radiometers. The additional components, shown in Figure 37, include the newly designed waveguide diplexer, dielectric resonant oscillators (DROs) [38], frequency multipliers [39], variable waveguide attenuators [40], 90° hybrid couplers [41], a clock [42] and a 3 dB power splitter [43].

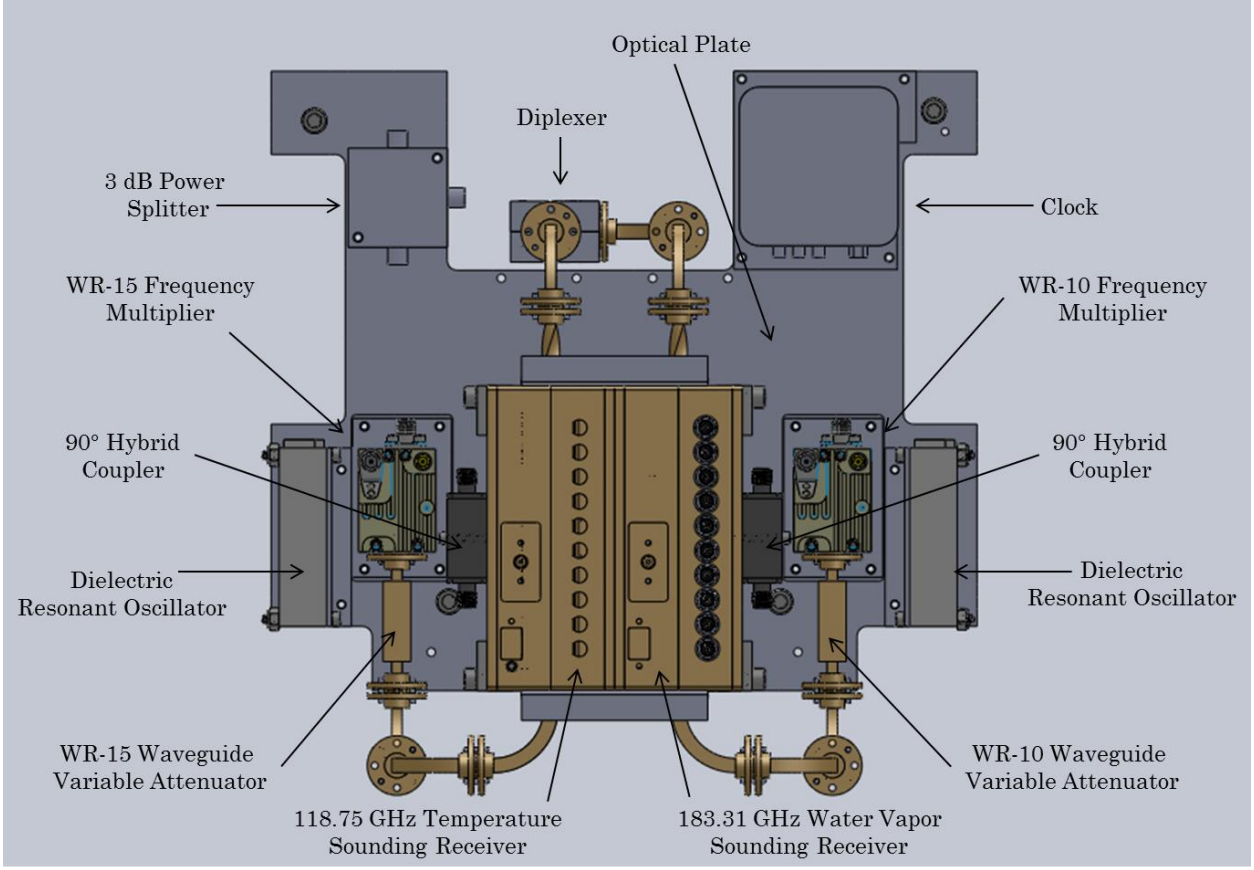

Figure 37: Millimeter-Wave Sounding Radiometer Components

The DROs, frequency multipliers, and variable waveguide attenuators are used to generate the LO signal for the sub-harmonic I-Q mixer in the MIMRAM. As

discussed previously, the 90° hybrid coupler [41] is used to reduce the noise inherit to super-heterodyne radiometers such as the mm-wave sounding radiometers.

The signal from the clock [42] is split equally into two signals by the 3 dB splitter [43]. The two signals are then sent to the temperature and water vapor sounding receiver ASICs. The locations of the interfaces between all of these components and the sounder receivers are shown in Figure 38.

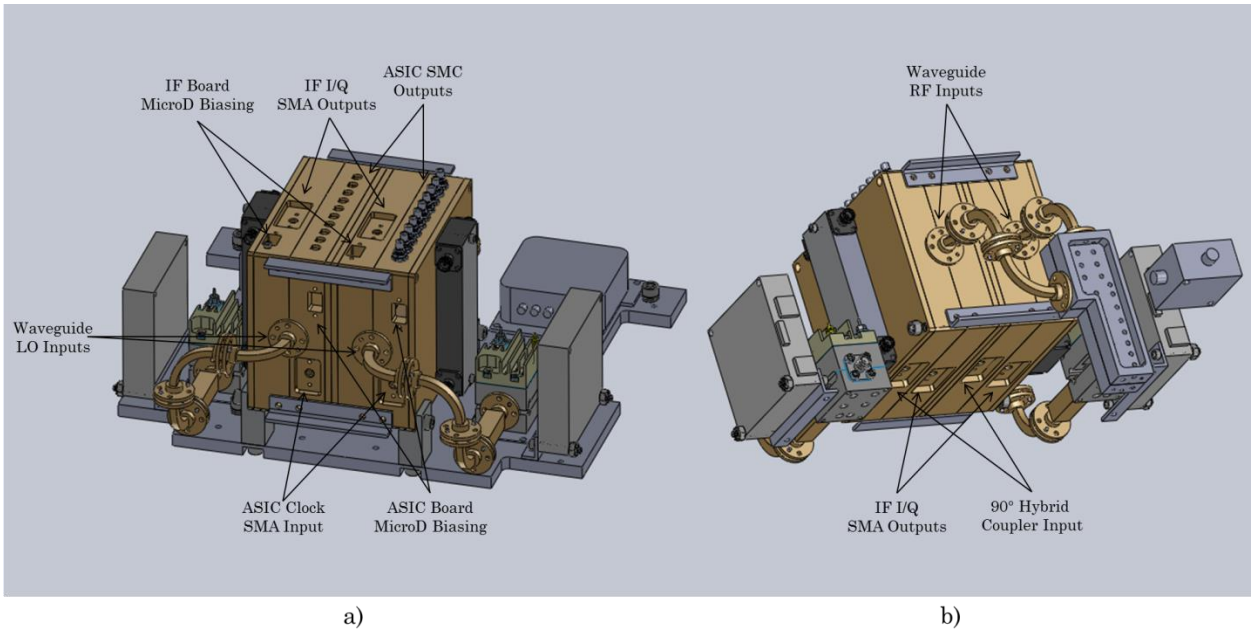

Figure 38: a) mm-Wave Sounding Radiometers Front Face Inputs b) mm-Wave Sounding Radiometers Back Face Inputs

The components that connect to the sounder receivers by waveguides, such as the diplexer and frequency multiplier, were positioned on the optical bench so standard waveguide sizes could be used. This eliminated additional costs and time associated with custom waveguides.

There are ten outputs from each of the ASICs (although only eight are digitized) that are located on the top faces of the sounding receivers and interfaced by SMC connectors [44]. Although all of the other components used in the millimeter-wave sounders have SMA interfaces, SMC connectors were used for the ASIC outputs as they are smaller than SMA connectors and all of the outputs could be placed on one sounder face.

Once the sounder receiver designs were completed, they were machined by Zen Machine and sent to JPL to be populated with the MIMRAMs, ASICs, IF boards, and connectors. The completed sounder receivers mounted in the HAMMR instrument are shown in Figure 37.

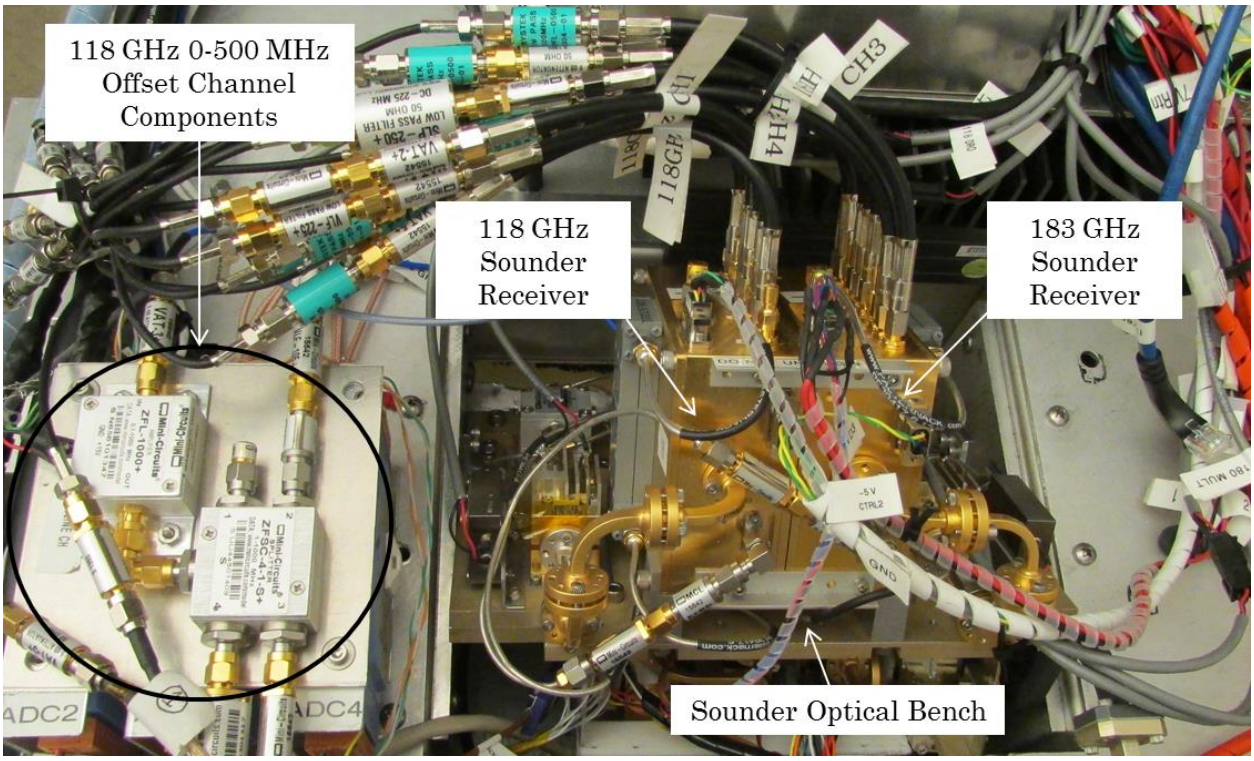

Figure 39: Assembled Millimeter-Wave Sounders in HAMMMR

The assembled sounder channels consist of additional hardware that was added after the design of the millimeter-wave sounders and optical bench. These additional components, labeled '118 GHz 0-500 MHz Offset Channel Components' in Figure 39, allow three additional channels to be measured directly out of the 90° hybrid coupler port as discussed previously. To do this, the output of the hybrid coupler that was originally terminated was sent to a 17 dB amplifier [45] and then separated into four channels by a power splitter [46]. Only three of the channels were used and filters were used to create offset center frequencies of 0 MHz, 250 MHz, and 500 MHz.

4.4.3 Sounder Receiver Flight Preparation

After the sounder optical bench was assembled, the bandwidths and output power levels needed to be set within the required power level for the diode detectors to operate in the square-law region. The test bench used to measure and set the output powers of the sounding channels is shown in Figure 40.

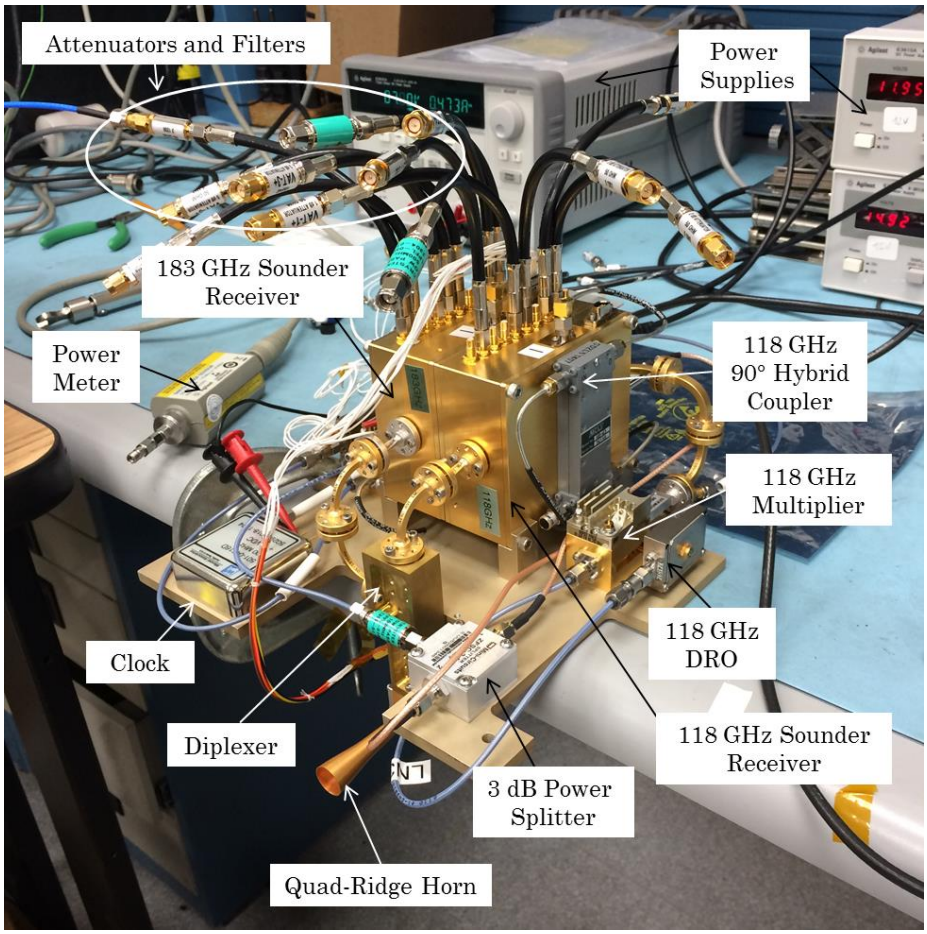

Figure 40: Millimeter-Wave Sounder Power Level Test Setup

After the band definition filters were placed in line with the sounding channel outputs, attenuators were added to maintain a -28 dBm power level input to the

diode detectors. The final measured output powers for the digitized sounding channels are summarized in Table 6.

Table 6: Sounder Receivers' Measured Output Power Levels

Center Frequency	Offset Frequency	Filter Type	Measured Power Level (dBm)
118.75	0 MHz	100 MHz LPF	-27.7
	250 MHz	200 MHz BPF	-27.4
	500 MHz	300 MHz BPF	-27.5
	+1 GHz	250 MHz LPF	-27.5
	+2 GHz	250 MHz LPF	-27.4
	+3 GHz	500 MHz LPF	-27.6
	+4 GHz	500 MHz LPF	-27.6
	+5 GHz	500 MHz LPF	-29.5
	+6 GHz	500 MHz LPF	Not Connected
	+7 GHz	500 MHz LPF	Not Connected
	+8 GHz	500 MHz LPF	Not Connected
183.31	-1 GHz	250 MHz LPF	-28.3
	-2 GHz	500 MHz LPF	-28.1
	-3 GHz	500 MHz LPF	-28.2
	-4 GHz	500 MHz LPF	-27.6

	-5 GHz	500 MHz LPF	-27.6
	-6 GHz	500 MHz LPF	-27.8
	-7 GHz	500 MHz LPF	-27.7
	-8 GHz	500 MHz LPF	-28.7

With the output powers set to the required power level, the sounder receivers are ready to be demonstrated airborne.

Chapter V Millimeter-Wave Window Radiometers

Three frequency channels, located in the "windows" near the mm-wave sounding bands, make up the mm-wave window radiometer. The three channels, which were determined by JPL, are centered at 90, 130 and 168 GHz. The design, testing, and characterization of these millimeter-wave window channels make up a significant portion of the work that was completed for this thesis and this work is described in detail in this chapter.

5.1. IIP-10 Millimeter-Wave Window Radiometer Design

The mm-wave window radiometers are direct detection receivers which were made possible by ground breaking technologies developed under the 2008 advanced component technology grant (ACT-08). The development of these radiometers and the improvements to the ACT-08 lab prototypes are presented in this section.

5.1.1 mm-wave Window Radiometer Block Diagram

The block diagram of the mm-wave window radiometer is shown in Figure 41. This figure should be referenced for the following description. The tri-frequency horn developed under the ACT-08 is used at the front end of the radiometers [47]. The signal from the antenna then enters the multi-chip module (MCM) which houses the majority of the RF components of the radiometer.

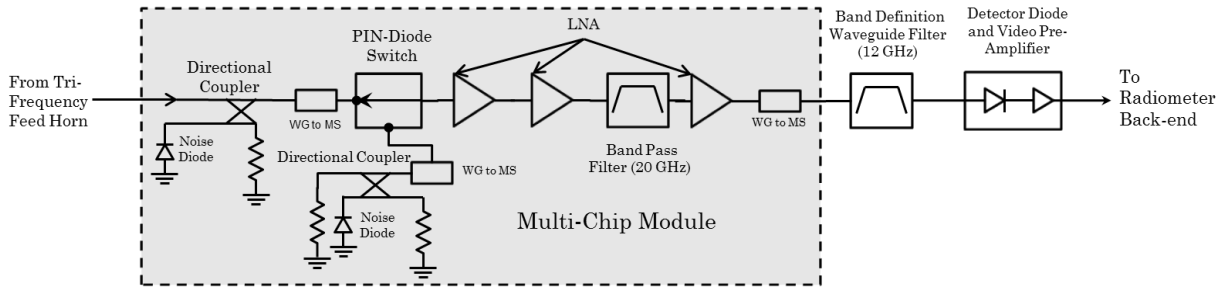

Figure 41: mm-wave Radiometers Block Diagram

At the very input of the MCM is a directional coupler that is used for internal calibration of the radiometer. To accomplish the two-point internal calibration, the directional coupler injects the signal coming from the noise diode at its coupled port, into the receiver front-end. The noise diode is fired on and off and the corresponding noise temperatures of these two states are known values. The difference between the output powers of these two states is called the noise deflection. The two points of the noise deflection are used to characterize linear relationship between the radiometer output voltage and measured brightness temperature [13].

A single-pole double-throw (SPDT) switch follows the coupler. The switch looks at its antenna port, an unknown brightness temperature, and reference port, a known brightness temperature, to calibrate out gain fluctuations. It is ideal for the switch to have identical performance as it switches between the two ports; however, the termination typically used at the reference port loads the switch differently than the input at the antenna port does. To mitigate this imbalance, a coupler and noise diode identical to the one at the antenna port is used at the reference port.

After the switch, the RF signal is passed into three low-noise amplifiers (LNAs) which are separated by a band-pass filter (BPF) used to avoid saturation of the final LNA. The amplified signal is coupled back into a waveguide by a second waveguide-to-microstrip transition.

Directly after the MCM is a waveguide band definition filter which sets the system bandwidth, a key parameter used in characterizing the receiver's radiometric resolution. The filtered RF signal is then input directly into the detector diodes without being down-converted. The direct-detect diodes, operating in the square law region, convert the RF power signal into baseband voltage signal. The baseband signal is then amplified a final time by a video amplifier before being sent to the analog-back-end board (ABEB) where it is digitized and integrated for data processing.

5.1.2 Previous Work

Prof. Steven C. Reising was awarded the Advanced Component Technology (ACT-08) in 2008 [48]. The objectives for the grant were to develop the necessary technology to design, build, and test lab prototypes of the mm-wave window channels from 90-168 GHz. The IIP-10 has continued on this work by developing the critical hardware and systems needed to make the radiometers airborne. Because this project was improving on the mm-wave radiometer lab prototypes,

significant contributions to the IIP-10 airborne radiometers were a result of the work accomplished through the ACT-08 grant.

One of the most significant contributions of the ACT-08 work is the mm-wave window tri-frequency horn. Having a single antenna for all three window channels is advantageous over three separate antennas because all three channels can be equally aligned with the focus of the parabolic reflector. After the antenna, the feed horn contains a triplexer which splits the absorbed atmospheric emission from the antenna into three channels with center frequencies of 90, 130 and 166 GHz. The tri-frequency horn is shown in Figure 42 next to a half dollar.

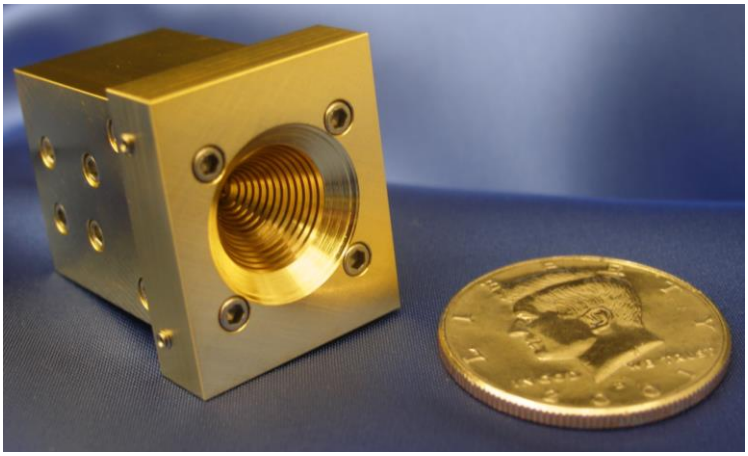

Figure 42: Tri-Frequency Horn [47]

Other technological advancements from the ACT-08 grant included the development of the SPDT switch and LNAs. The ACT-08 SPDT switches showed improved

insertion loss and isolation compared to the previously used switches at these frequencies and its performance is shown in in Figure 43.

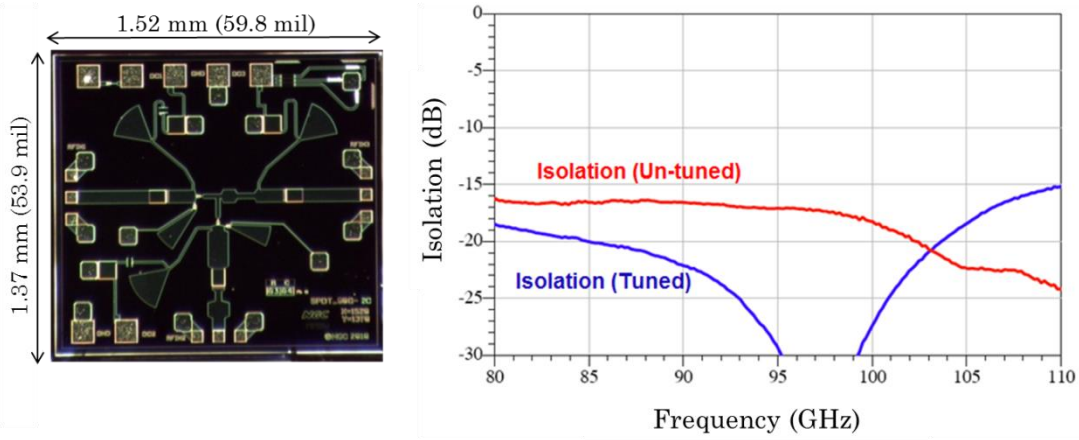

Figure 43: ACT-08 PIN Diode SPDT [49]

The other components that make up the mm-wave window radiometers were designed at CSU. This included attenuators, bandpass filters, waveguide-to-microstrip transitions, matched loads, and lab-prototype multi-chip modules (MCM) that house the RF chain. The assembled 90 GHz multi-chip module (MCM) lab prototype is shown in Figure 44 relative to a dime.

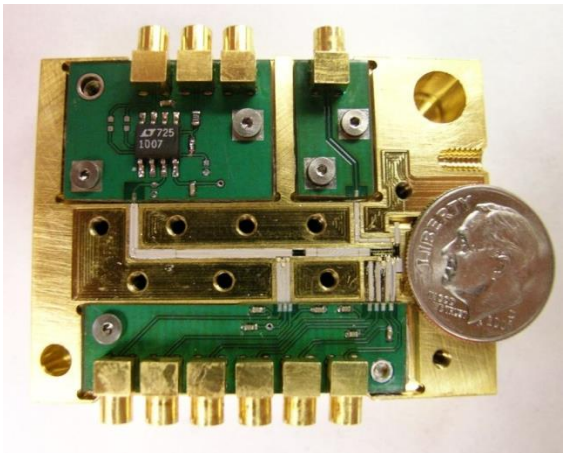

Figure 44: ACT-08 90 GHz Multi-Chip Module Lab Prototype [5], [6]

The tri-frequency horn, LNAs, and SPDT switches developed under the ACT-08 were directly implemented into the IIP-10 airborne radiometers. However, many other components of the mm-wave lab prototypes were modified including the passive components, approach to biasing, and MCMs. These improvements are discussed in detail in the following section.

5.1.3 Improvements from ACT-08 Architecture

There are several, important advancements made from the designs inherited from the ACT-08. The underlying motive for these improvements was to advance the lab prototypes into airborne radiometers. In addition to advancing the radiometers airborne by reducing their mass and footprint, lessons learned from the ACT-08 were used to improve the overall radiometer performance and our ability to characterize the system. These changes are summarized in Figure 45.

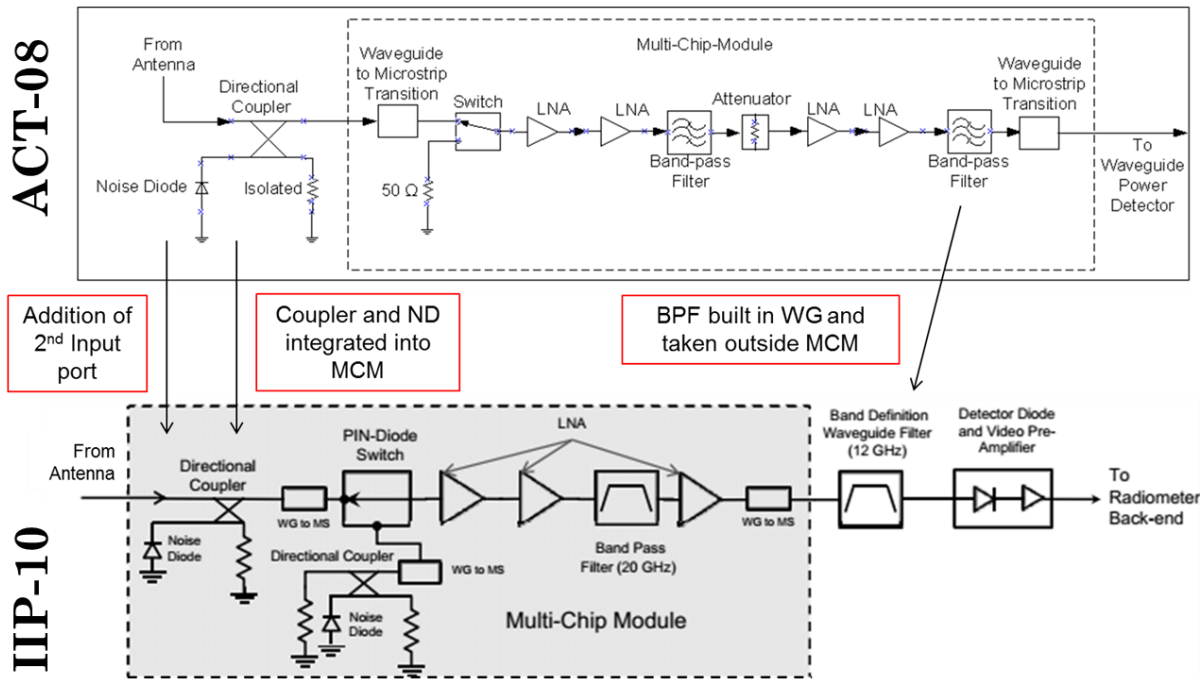

Figure 45: Major Modifications to ACT-08 mm-Wave Radiometers

The first major improvement is a custom-designed 10 dB coupler that replaced the commercially available coupler used the in the ACT-08. This new design had several advantages, the first being a 66% reduction in mass and size of the coupler. With a smaller foot-print and split-block design, the coupler can now be included in the MCM. With the coupler integrated into the MCM, the number of interfaces, and therefore losses before the first gain stage, were reduced.

The performance of the SPDT switch was also improved by the newly designed couplers. In the ACT-08 lab prototype radiometers, a matched load was used at the reference port of the switch which has a different impedance than the load seen at the antenna port of the switch. For the IIP-10 radiometers, the matched load at the

reference port is replaced by a coupler identical to the newly designed directional coupler at the antenna port. This makes the impedance seen at the two ports of the switch nearly identical. The reference port coupler even has its input port taken out to the face of the MCM as the antenna port coupler does. The face of the MCM with the two ports on its face is shown in Figure 46.

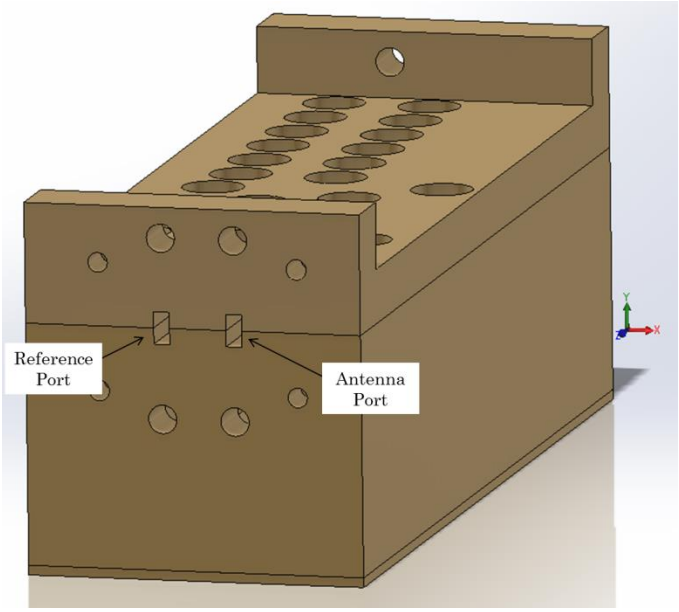

Figure 46: Two Input Ports on 90 GHz MCM

Having identical directional coupler loads with inputs going to the face of the MCM results in two benefits, the first being near identical loads on the switch's ports. Secondly, this allowed for the two ports of the antenna to be used as either a reference port or antenna port by simply terminating one input and feeding the output of the tri-frequency horn to the other input.

Another major improvement to the ACT-08 architecture was the band definition filter. The band definition filters developed under the ACT-08 were edge-coupled microstrip filters built on 5 mil alumina [5], [6]. The measured performance of these filters in air and in a test cavity showed that the filter did not have a flat band across the passband and the out-of-band-rejection had an unacceptably slow roll-off. In addition, band definition filters built in microstrip need to be placed inside the multi-chip modules making it impossible to directly measure their response once inside. This causes uncertainties in the measurements taken in air or a test cavity due to the significant impact on the filter's performance by other microstrip devices, wire bonds, lid height, and cavities in the trench. Accurately knowing the bandwidth of the system in its final configuration is critical for characterizing and analyzing the radiometer's performance [9].

For the IIP-10, the microstrip band definition filter was replaced by a custom-designed waveguide band definition filter. The waveguide filter showed significant improvements in performance and, more importantly, allowed direct measurement of its bandwidth in its final configuration in the radiometer.

5.2. Coupler Design and Measurement

Directional couplers were designed at the millimeter-wave radiometer center frequencies of 90 GHz, 130 GHz, and 166 GHz for integration into each multi-chip module. In the front-end of each radiometer, just after the antenna, a coupler is

used to couple a noise source of known output power into the radiometers for internal calibration. Previously in the ACT-08, commercially-available waveguide 10 dB couplers from ELVA were used and are shown in Figure 47 [50].

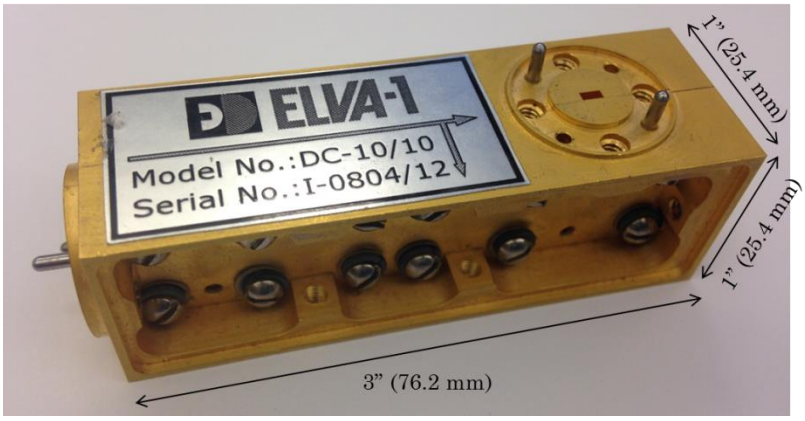

Figure 47: WR-10 ELVA 10-dB Directional Coupler

Although these couplers meet the performance specifications, they were quite bulky and added an additional interface, and therefore loss, between the tri-frequency horn and the MCM. It was desirable to replace these couplers with custom-designed couplers that would reduce the size of the couplers and the losses they introduce before the first LNA.

5.2.1 Coupler Fundamentals

As its name implies, a directional coupler serves to couple two signals together at a specified level. A directional coupler can be modeled as a four-port network, as shown in Figure 48. The signal entering into the input port propagates to the output, or through port, just as it would in a standard waveguide. The signal at the

coupled port is coupled with the incoming signal. The power of the signal that is coupled to the incoming signal is specified by the coupling factor, in this case 10 dB. Because the coupler is mirrored about the center, 10 dB of the incoming signal will also be coupled to the isolated port in addition to the remaining part of the coupled port signal that isn't coupled to the through port. To avoid reflections back into the coupler, the isolated port is terminated with a matched load.

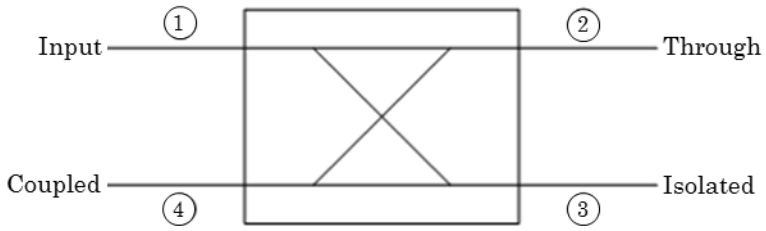

Figure 48: Layout of a 4-Port Directional Coupler

In the IIP-10 mm-wave radiometer implementation, the coupled port is terminated with a noise diode, the isolated port is terminated in an integrated matched load, the input port is connected to the antenna, and the through port is connected to the monolithic microwave integrated circuit (MMIC) RF receiver chain at the front-end of the radiometer.

5.2.2 Design Considerations

Since the coupler is inserted before the low-noise amplifiers, minimizing insertion loss was critical. The previously used ELVA waveguide couplers have a specified

insertion loss of 1.2 dB and a return loss of 43.1 dB [5], [6]. The measured performance of the WR-10 ELVA coupler is shown below in Figure 49.

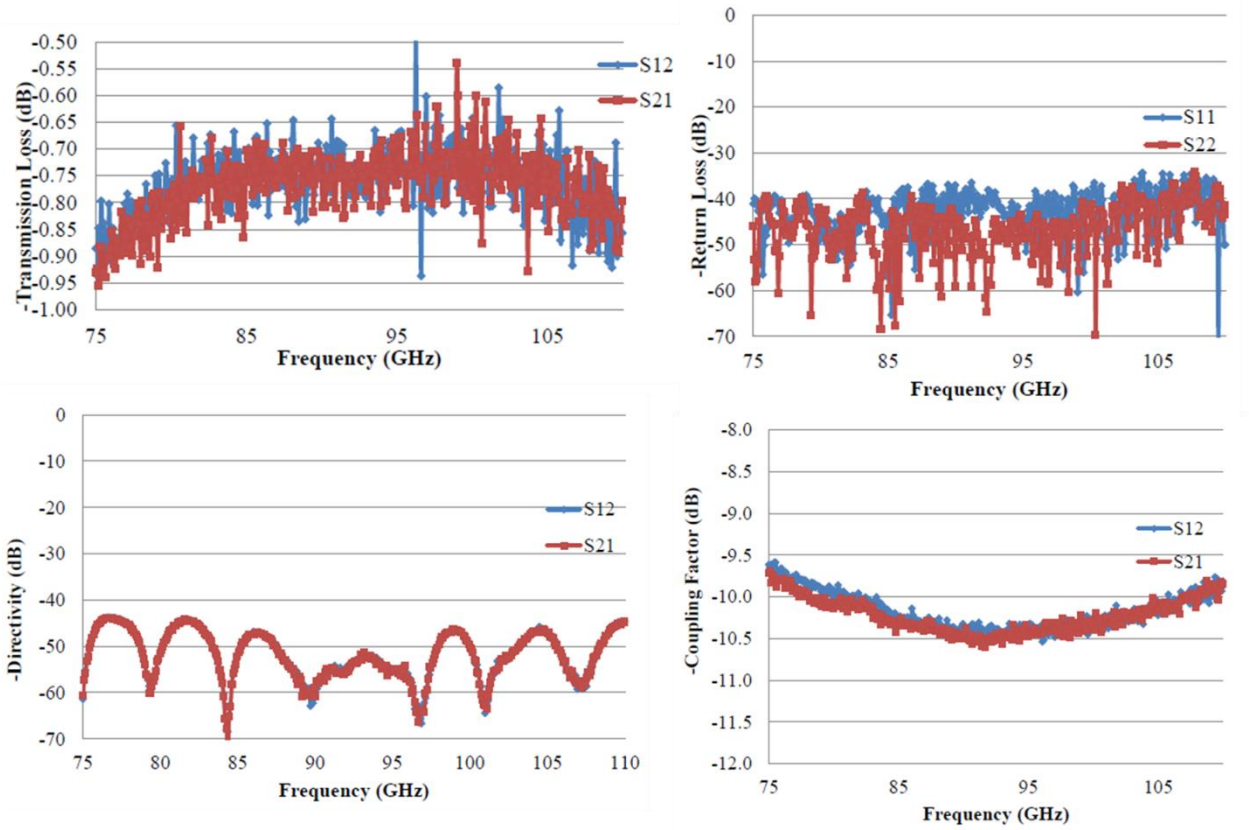

Figure 49: Measured Performance of ELVA WR-10 Coupler [5], [6]

It was required to further reduce the insertion loss to less than 1 dB and maintain, if not improve, the return loss. The last design requirement was to have very high isolation as it can degrade the radiometric resolution. Assuming there is a 10 K fluctuation from the matched load, an isolation of 40 dB would be needed to keep the fluctuation seen by the output port to 0.001 K.

Initially, both waveguide and microstrip directional coupler implementations were considered. Different numbers of sections were simulated using ANSYS Designer in order to do an initial comparison of their respective performances [51]. The results of these simulations are summarized in Table 7.

Table 7: Comparison of Simulated Performance for 90 GHz Couplers

Type of Coupler	n (sections)	Insertion Loss (dB)	Coupling (dB)	Isolation (dB)	Return Loss (dB)	Total Length
Microstrip Directional Coupler	1	0.54	10.8	27.7	20.6	0.01" (0.33 mm)
	3	0.67	10.5	13.4	19.1	0.04" (0.98 mm)
Waveguide Branch-line Coupler	1	0.5	10.9	16.4	26.4	0.11" (2.92 mm)
	4	0.46	10.1	52.8	50.8	0.2" (5.08 mm)

Although the waveguide based couplers take up significantly more space, in some cases up to five times more, the microstrip couplers failed to meet the design goals. Even though the initial simulated waveguide branch-line coupler seems quite large at 0.2" (5.08 mm), it still significantly reduces the mass and size when compared to the previously used ELVA DC-10 coupler which is over 75 mm in length. Taking these factors into consideration, it was decided to proceed with the with the waveguide branch-line coupler design.

5.2.3 Design Process

A directional coupler consists of two main, parallel transmission lines coupled by perpendicular branch lines and is symmetric about its center. Figure 50 shows the physical E-plane cross-section of a four section coupler where the main lines are horizontal across the page and the branch lines are vertical across the page.

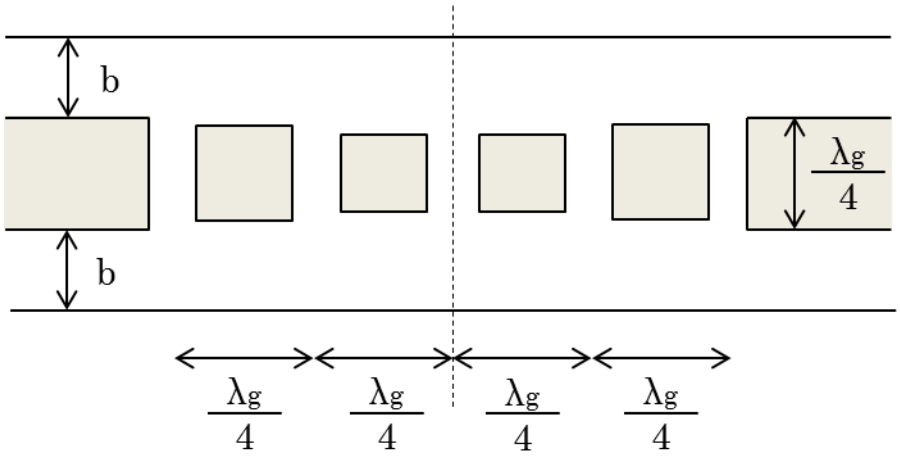

Figure 50: E-Plane Cross Section of a Four Section Branch-Line Coupler

The branch lines are separated from each other by a distance equal to one quarter wavelength at center frequency, $\lambda_g/4$. The two main lines are also separated by $\lambda_g/4$. These distances set the center frequency of the coupler. The impedance of each branch is set by varying the height of the waveguide in each branch, b_n, where b_0 is the standard height for a WR waveguide and all others heights are determined by the desired coupling and number of sections. The width of the waveguides, a, always remains the standard dimension of the WR waveguide.

ANSYS's High Frequency Structure Simulator (HFSS) was used for all electromagnetic (EM) analyses for the work described in this thesis [35]. By building the coupler model in HFSS as a function of variables it streamlined the process of analyzing different numbers of branches with varying impedances. Although increasing the number of branches improved the performance of the coupler across the band of interest, the spacing between the sections became too small to be physically machined. It was found that n=2, or three branches, met all the design requirements and could still be easily machined.

The waveguide heights were hand-tuned to account for the effect the waveguide junctions had on the performance. Once the design could no longer be improved by hand tuning, the optimization tool on HFSS was used to further improve this performance. The E-plane cross section of the HFSS coupler prototype model is shown below in Figure 51. The blue shows the air filled waveguide and the yellow box surrounding this is the gold-plated brass housing surrounding the coupler. In future designs and simulations, the outside housings for structures were not simulated as it significantly increased the time it took for a simulation run. Instead, boundary conditions were set on the faces of the air filled waveguide.

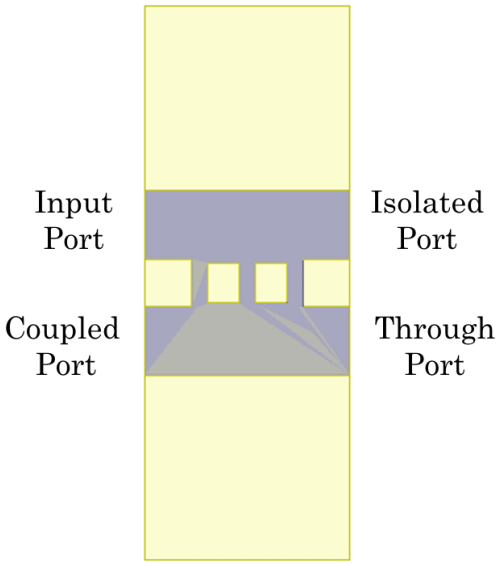

Figure 51: E-Plane Cross Section of HFSS Coupler Model

Once the desired performance was achieved in HFSS, the physical computer-aided design (CAD) structures were built in Solidworks [52]. The CAD model for the 90 GHz coupler prototype is shown in Figure 52. The coupler was designed to be machined in split block. A split block design consists of two halves that connect to form the complete coupling structure. The couplers were split in the middle along the E-plane to minimize its impact on performance.

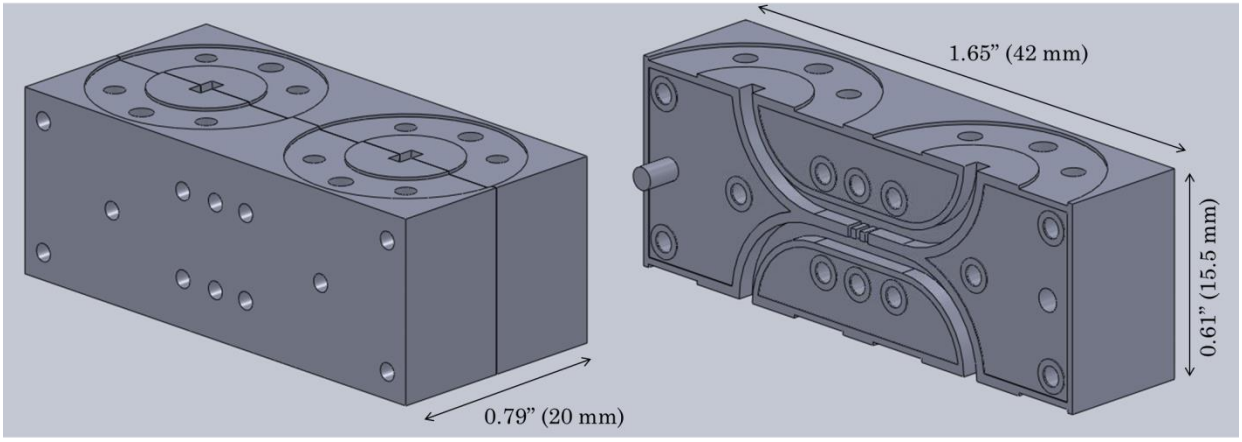

Figure 52: Solidworks CAD Model of the Split-Block 90 GHz Coupler Prototype

The physical size of the couplers had to be increased to accommodate the waveguide flanges necessary to connect the coupler with other components and measure its performance. Each of the four ports needed to be interfaced with a circular waveguide flange which measures 0.75" (19 mm) in diameter. Because the spacing between the ports of the waveguide coupler is not large enough to accommodate the flanges, straight lengths of waveguide and 90° bends were added to the design. The coupler with the additional arms was re-simulated in HFSS to verify it would not negatively impact the performance.

The CAD model was then finalized in Solidworks and sent to Zen Machine to be manufactued [37]. The machined 90 GHz coupler prototype is shown below in Figure 53.

Figure 53: Machined 90 GHz Coupler Prototype

The split-block couplers were machined in brass and then gold plated. Gold plating is critical to reduce conductor losses in the coupler since it comes before the before the first gain stage in the radiometer. The resistive losses are directly proportional to the surface resistivity of the material. As defined by the relationship in (V.1), the surface resistivity, and therefore conductor losses, can be reduced by using a material with higher conductivity.

$$R_s = \sqrt{\frac{\omega\mu_0}{2\sigma}} \tag{V.1}$$

where ω is the angular frequency, μ_0 is the permeability, and σ is the conductivity of the material. The conductivity of brass is σ_{brass}=2.564 x 10^7 S/m and the

conductivity of gold is σ_{gold}=4.098 x 10^7 S/m which reduces the conductor losses by 26%. In addition, gold plating is good for reducing corrosion.

5.2.4 First Coupler Prototype

The purpose of the first prototype at 90 GHz was to characterize the performance of the coupler before integrating it in the MCM where it cannot be directly measured. Because this was the first component designed using the HFSS software, it was also of interest to compare the simulated and measured results to conclude how accurate the HFSS simulations were. The coupler measurements were done at the Microwave Systems Laboratory (MSL) using a two port vector-network analyzer (VNA) with WR-10 waveguide extensions. One of many test benches used to measure the coupler performance is shown in Figure 54.

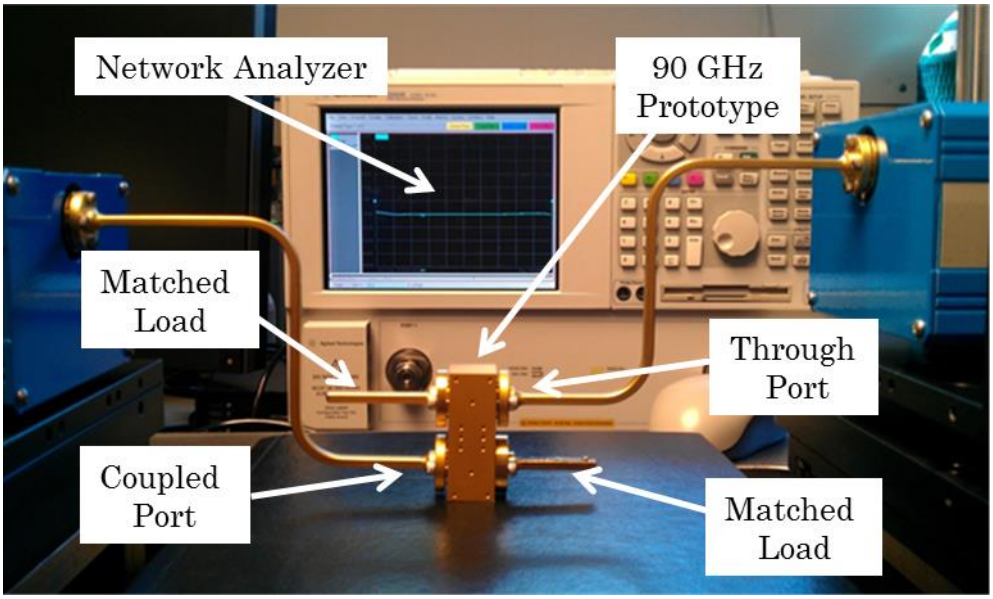

Figure 54: 90 GHz Coupler Test Bench Set Up to Measure Coupling

Since a two-port network was being used to measure a four-port device, multiple measurements were needed to fully characterize the coupler. The test setup to measure coupling, shown in Figure 54, has the isolated and input ports terminated and the through and coupled ports connected to the VNA. Various configurations of this test setup were needed to measure return loss, coupling, isolation, and insertion loss. The results of these measurements, compared to the simulated results, are presented in Figure 55.

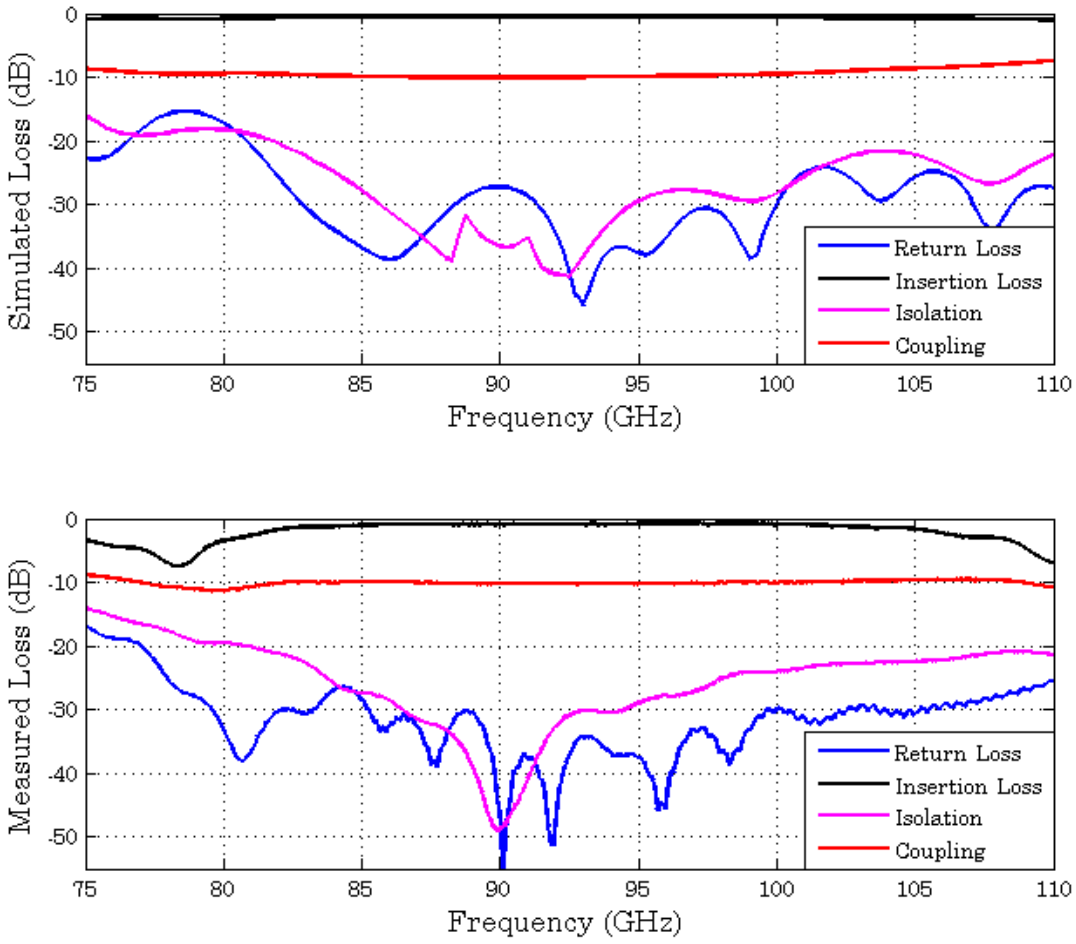

Figure 55: 90 GHz Coupler Prototype Simulated and Measured Performance

The measured and simulated performances are very similar verifying the accuracy of the HFSS software. The measured performance has met and exceeded all design goals stated in 5.2.2. The average values for insertion loss, return loss, isolation, and coupling over the band of interest, 85 GHz to 95 GHz, is summarized in Table 8.

Table 8: Summary 90 GHz Coupler Measurements

	Design Goal (dB)	IIP-10 Coupler (dB)	ELVA Coupler (dB)
Insertion Loss	< 1	0.57	1.2
Coupling	10	10.2	10
Isolation	> 25	36.1	N/A
Return Loss	> 25	36.9	43.1

In addition to the 66% reduction in mass of the newly designed coupler compared to the previously used, commercially available ELVA coupler, the performance of the 90 GHz coupler prototype also showed improved performance in terms of insertion loss and had comparable performance in all other specifications. To further improve the coupler design, an integrated matched load needed to be designed to internally terminate the coupler's isolated port.

5.2.5 Integrated Matched Load

The isolated ports on the newly designed couplers need to be terminated with a matched load. Commercially available terminations can be quite large and are external to the device's port they are terminating, as seen in Figure 56. The newly designed couplers are to be contained within the MCMs which meant that traditional matched loads would not work for this application.

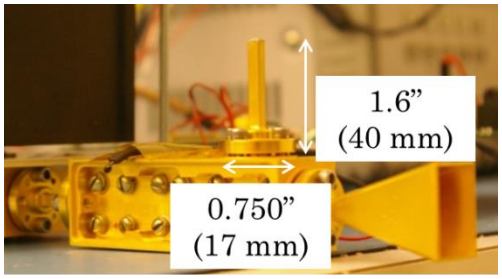

Figure 56: Commercially Available Termination

To this end, integrated matched loads were designed to internally terminate the isolated port of the coupler. As an initial design, a compact WR-10 waveguide load designed by the Atacama Large Millimeter/submillimeter Array (ALMA) project was referenced. This design is described in [53] and shown below in Figure 57. This design can be easily scaled for the WR-8 (130 GHz) and WR-5 (168 GHz) MCMs.

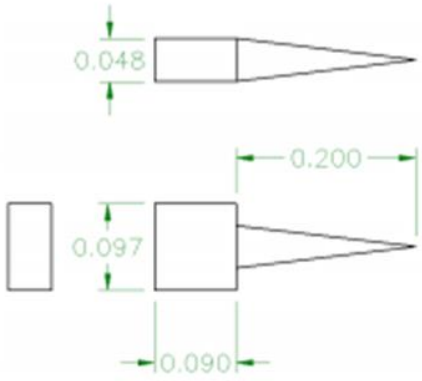

Figure 57: ALMA Compact WR-10 Waveguide Load, Dimensions in Inches [53]

Although the ALMA internal matched load design served as a good starting point, improvements were needed to make the design more robust with respect to machining tolerances. Because the ALMA designed load has a tip directly center in

the waveguide where the electric field is at its maximum, the ability to machine a small tip is crucial. If the tip in the center gets cut incorrectly resulting in a duller tip, it could potentially send reflections back into the coupler. For this reason, the design was modified to have a flat tip that rests in the corner of the waveguide.

Another improvement to the ALMA design is that the square body of the newly designed termination does not need to completely fill the waveguide cavity. There is approximately a 10 mil gap between the termination and the broadside wall at the thickest part of the termination. This modification showed improved performance with respect to machining tolerances in this dimension. These modifications are illustrated in Figure 58.

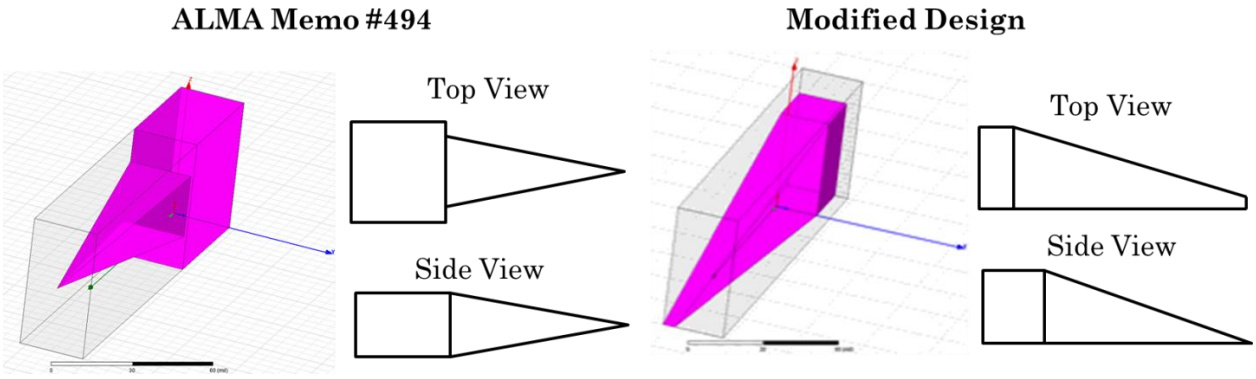

Figure 58: Comparison of ALMA Termination and New Modified Termination

The newly designed terminations were simulated in HFSS using Eccosorb MF116 material [54]. All three simulated loads showed greater than 35 dB return loss over the bands of interest. The largest of the three modified terminations is the WR-10

load which has the dimensions 0.359" x 0.088" x 0.039" (9.1 x 2.2 x 1 mm). Compared to the commercial load with dimensions 1.6" x 0.75" x 0.75" (40 x 19 x 19 mm), the custom designed terminations significantly reduce the size of this component without sacrificing performance. The final Solidworks models of the WR-10, WR-8 and WR-5 loads are shown in Figure 59.

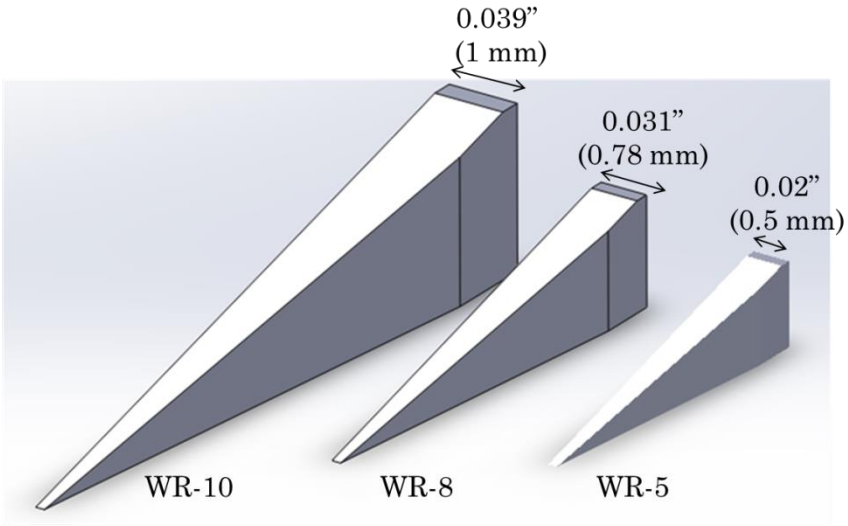

Figure 59: WR-10, WR-8, and WR-5 Internal Matched Loads

To physically measure the performance of these waveguide terminations and verify the simulated results, a test cavity was needed. Additionally, it was also of interest to measure the impact the internal matched load had on the coupler performance. To this end, a second coupler prototype at 168 GHz was designed to include the internal matched load.

5.2.6 Second Coupler Prototype

A second coupler prototype was designed to measure the performance of the coupler with the newly designed internal matched load placed at the isolated port. The second prototype was designed for the 168 GHz channel as it was expected to be more sensitive to machining tolerances compared to the 90 GHz coupler prototype due to its smaller dimensions. The HFSS model for the 168 GHz coupler prototype with an internal matched load is shown in Figure 60 and the corresponding Solidworks CAD model is shown in Figure 61.

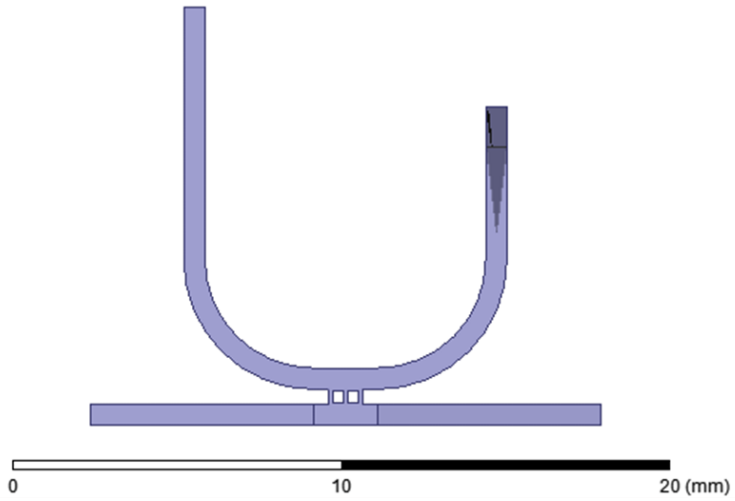

Figure 60: 168 GHz Coupler Prototype HFSS Model

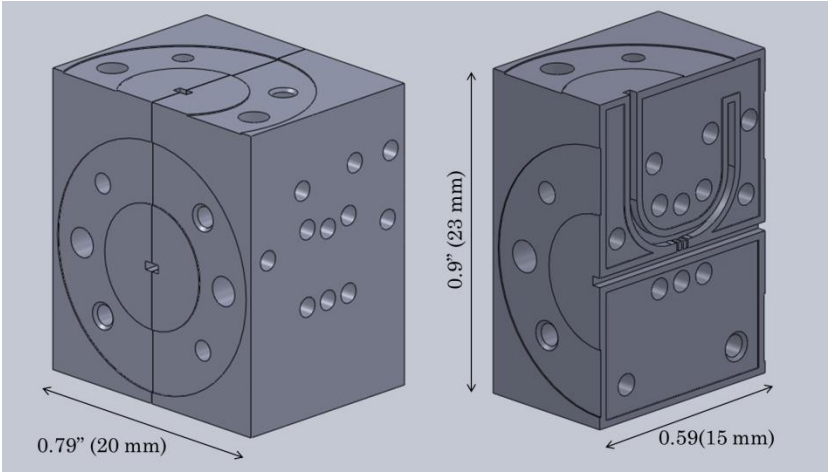

Figure 61: 168 GHz Coupler Prototype Solidworks Model

This coupler was designed to be machined in split block and the completed prototype is shown in Figure 62. Note that the 168 GHz coupler prototype only has three ports unlike the 90 GHz coupler prototype which has four ports. The

measurements were completed at JPL since MSL has facilities to measure only up to 110 GHz.

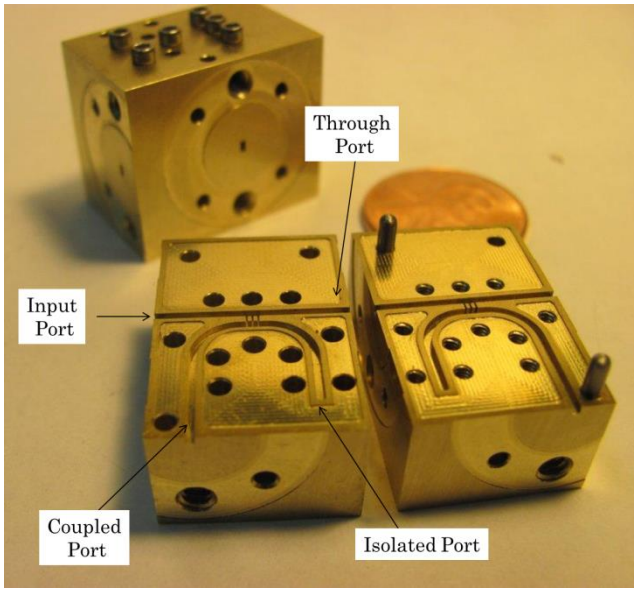

Figure 62: Machined 168 GHz Coupler Prototype

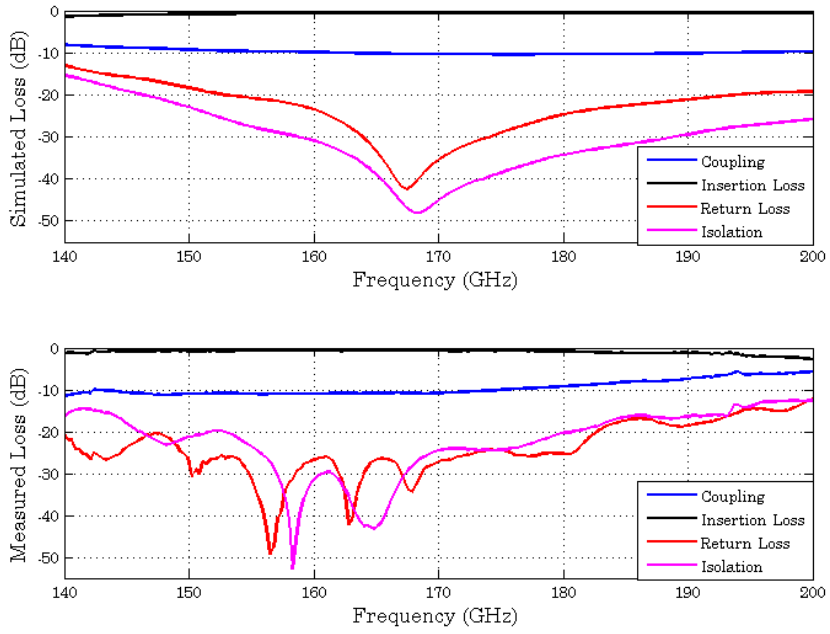

Figure 63: 168 GHz Coupler Prototype Simulated and Measured Performance

The measured and simulated results were fairly similar; however, it is quite obvious that there is a ~10 GHz shift in center frequency between the two results. As discussed in 5.2.3, the spacing between each of the branches in the coupler is designed to be one quarter wavelength at the center frequency. Because the shape of the measured performance matched closely to the simulation with just a shift in center frequency, it was suspected that the branch spacing was the culprit for this discrepancy. Upon further investigation, it was discovered that the spacing between the two main-line branches in the Solidworks model was mistakenly made to be 25.5 mils, which is the short wall dimension in a WR-5 waveguide. One quarter wavelength at 166 GHz (center frequency at the time of the design) in a WR-5 air-filled waveguide is 17.75 mils. This error in the model is highlighted in Figure 64. Because this distance, and therefore quarter wavelength, was longer than intended, the center frequency was shifted down. This conclusion was verified in HFSS.

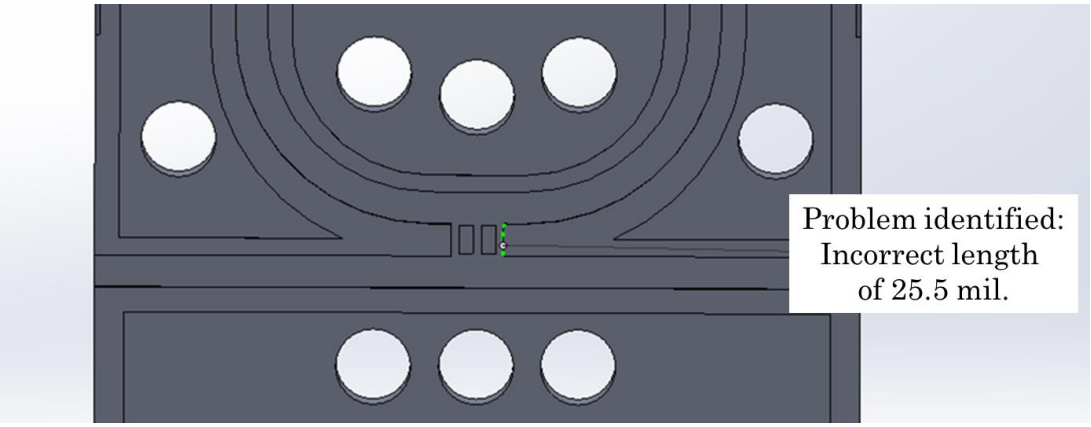

Figure 64: 168 GHz Coupler Prototype Solidworks Model Error

All subsequent designs after the 168 GHz coupler made in HFSS were directly imported into Solidworks which eliminated the possibility of this error happening again. Although the center frequency was shifted, the average performance over the band of interest, 162 GHz to 174 GHz, still met and exceeded the design goals summarized in Table 9.

Table 9: Summary of Measured Performance of the 168 GHz Coupler Prototype

	Design Goal (dB)	**Measured (dB)**
Insertion Loss	< 1	0.68
Coupling	10	10.6
Isolation	> 25	31.3
Return Loss	> 25	29.2

In addition to characterizing the 168 GHz coupler measured performance, the 90 GHz and 168 GHz measurements were also compared in order to determine the impact the internal load had on the overall performance.

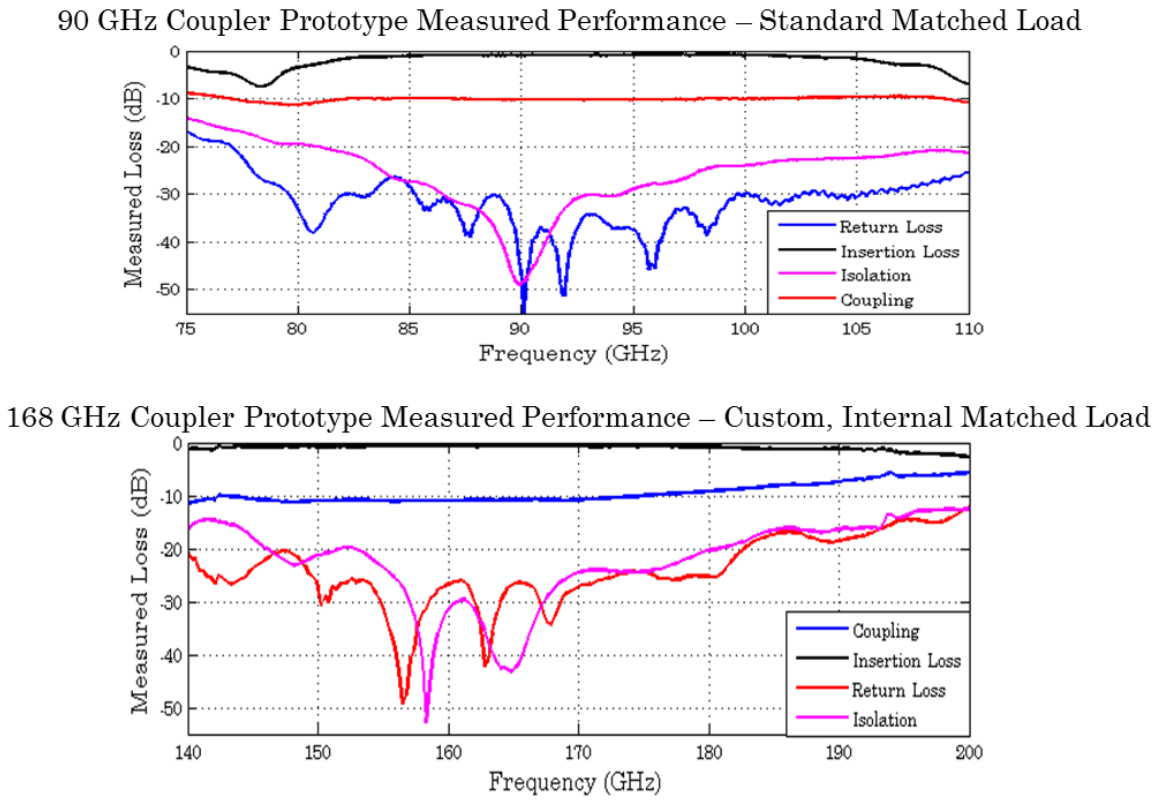

Figure 65: Comparison of 90 GHz and 168 GHz Couplers' Measured Performances

Comparing the measured performance of the two coupler prototypes in Figure 65, it can be seen that the couplers have similar performance. From this it can be concluded that the internal load does not introduce ripples or negatively impact the coupler performance.

5.3. Band Definition Filter Design and Measurement

Band definition filters were designed at the millimeter-wave radiometer center frequencies of 90 GHz, 130 GHz, and 168 GHz. After the amplification stage in the mm-wave radiometers, the power signal is filtered before being sent to the detector

diodes and converted into a voltage signal. In addition to the bandwidth defining the radiometric resolution of the receiver, it also limits the power input to the detector diode so it operates in the square law region [13].

As part of the work that was done under the ACT-08, band definition filters were designed. These filters were manufactured on 5 mil thick polished alumina with an edge coupled microstrip topology [5], [6]. The filter design was done in HFSS and the model accounted for the lid height of the RF trench it would be placed in. Although the simulations predicted a satisfactory performance, the microstrip design presented several difficulties that made it unattractive for the IIP-10 mm-wave radiometers.

The most notable problem was that the filter performance could never be directly measured in its final configuration. Because these types of filters are sensitive to other substrates in the same cavity, lid height, cavities in the trench and wire bond length, it would be difficult to confidently predict the bandwidth with just HFSS simulations. As an attempt to obtain these measurements of the band definition filters, test fixture blocks were machined to approximate the final configuration. The results of these measurements, and its comparison to the modeled performance, are shown below in Figure 66.

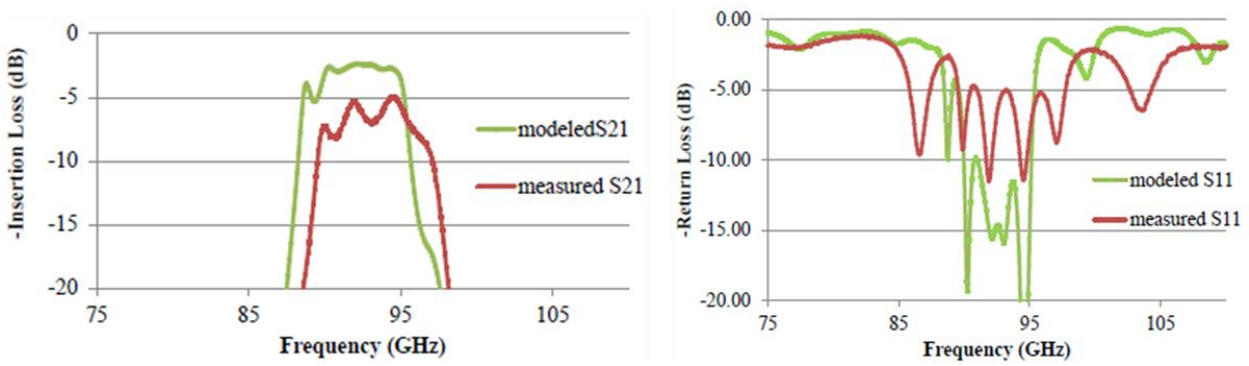

Figure 66: ACT-08 90 GHz Band Definition Filter

Measured and Simulated Performance in Test Block [5], [6]

It was found that the measured performance in the test block was significantly worse than the modeled performance in HFSS. The insertion loss over the pass band was approximately 3 dB higher than the modeled performance and contained large ripples. Similarly, the measured return loss differed from the simulations by a large increase in the designed bandwidth and was on average 5 dB lower than what it was modeled to be. Due to these inconsistencies between the measured and simulated results, and the desire to directly measure the bandwidth of the filter in its final configuration, it was decided to venture away from the edge coupled microstrip approach for the IIP-10 airborne radiometers.

5.3.1 Waveguide Filter Fundamentals

The IIP-10 band definition filters were to be designed in waveguide. The waveguide approach has several advantages over the microstrip implementation. This includes less insertion loss, ability to directly measure the bandwidth in its final configuration, and a more simple design. The microstrip edge-coupled filter couples

the signal between isolated transmission lines. The coupling between these lines is very sensitive to fabrication tolerances and fringing effects at this frequency. The waveguide filter uses discontinuities, referred to as irises, that protrude into the transmission path in the waveguide which and are seen as the circuit elements shown in Figure 64.

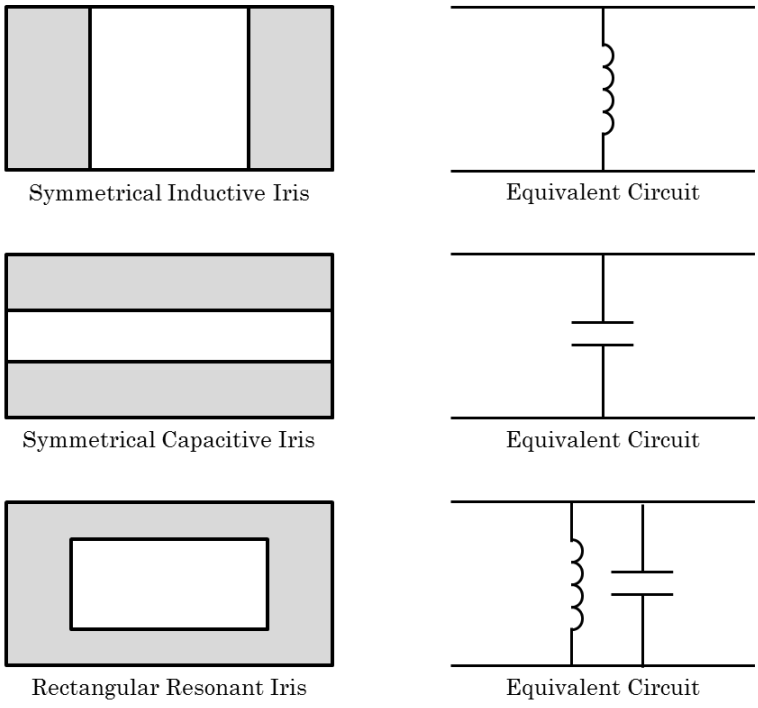

Figure 67: E-Plane Cross Section of Waveguide Iris Geometries and Their Equivalent Circuit

Taking advantage of this effect of irises on the impedance of the waveguide, multi-section filters can be easily made in waveguide. The dimensions of the irises are large in comparison to the coupled edge microstrip restructure and are, therefore, less sensitive to machining tolerances. Additionally, past experience has shown that

HFSS tends to more accurately predict the performance of a waveguide component over a passive microstrip component.

5.3.2 Design Considerations

The bandwidths of the filters were to be designed as 8 GHz, 12 GHz, and 12 GHz for 90 GHz, 130 GHz, and 168 GHz, respectively. These bandwidths are quite narrow with respect to their channel center frequency which makes the waveguide-iris filter a great choice to do its ability to easily achieve narrow bandwidths [36].

Although some of the geometries shown in Figure 67 should, theoretically, have better performance than others, other factors were taken into consideration before the final design was chosen. Most notably, the machinability and assembly were a top consideration for this choice. Since the filter was to be machined in split block, which cuts the waveguide in half along the broadside wall, designs with irises spanning this wall were eliminated as options. This is because manufacturing tolerances could cause the irises to be spaced differently on each half of the split block which could result in misalignment of the two halves of the irises with respect to each other. With the other iris design choices removed as options, an inductive iris geometry was decided on as the basis for this design.

5.3.3 Design Process

Once the geometry of the irises was chosen, other properties, such as type of filter and number of sections, still need to be decided on. Comprehensive tables for various types of filters and sections are included in [36]. The tables include filters up to 15 sections for Chebychev, Buttersworth, and other various architectures. Provided with these tables are equations relating the waveguide impedance, and therefore physical dimensions, to the desired inductive iris values. These tables and relationships were built into a MATLAB script, attached in [Appendix], which quickly generated physical dimensions given different filter architectures.

HFSS models were built in conjunction with the MATLAB script. The physical structures in the HFSS model were defined by a series of variables whose values were obtained from the output of the MATLAB program. Together, the MATLAB program and HFSS models formed a streamlined process through which many different configurations were quickly designed and simulated. After some initial designs were simulated, it was evident that a Butterworth filter was a better choice over a Chebychev filter due to its characteristic maximally flat pass band response. The Chebychev filters did show a steeper roll off outside the pass band; however, this could be compensated for in the Butterworth filter by increasing the number of sections. Table 10 shows a summary of the simulated performance of Butterworth filters with different number of sections and Figure 68 shows the results for the 90 GHz filters.

Table 10: Simulated Performance of Various Configurations of a Maximally-Flat, Inductive Iris, Butterworth, Waveguide Band Pass Filter

n	Center Frequency (GHz)	Average Insertion Loss (dB)	Average Return Loss (dB)
3	90	0.84	11.49
	130	1.07	16.45
	168	1.5	15.2
6	90	0.64	12.8
	130	0.99	15.6
	168	0.8	15.1
8	90	0.41	16.8
	130	0.67	20.64
	168	0.62	23.6

At first glance of Table 10, it would appear that there is little advantage of having six sections compared to three sections and eight sections compared to three sections. However, by inspection of Figure 68 it becomes evident that the filter with six sections has a much steeper roll off than the three-sectioned filter

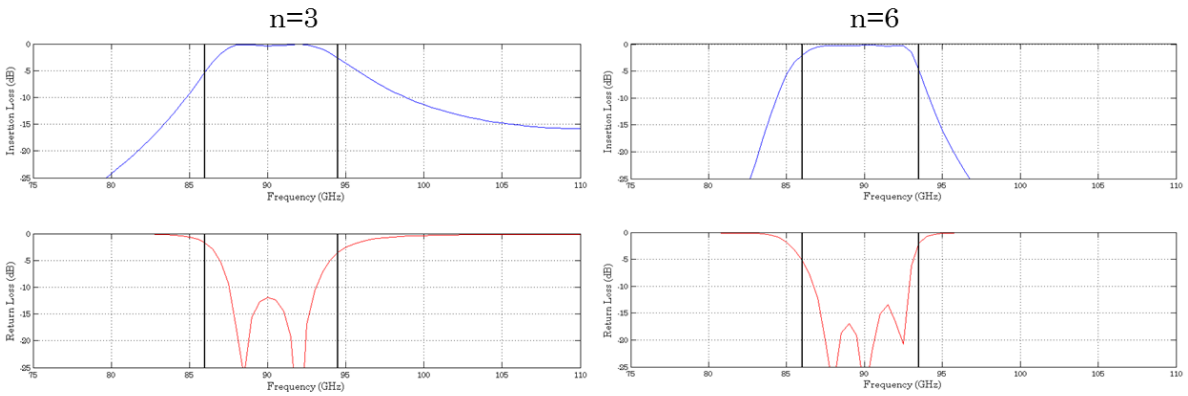

Figure 68: 90 GHz Waveguide Filter Simulated Results for Varying Number of Sections

Comparison of the eight section filter to the six section filter did not show signification improvements similar to Figure 68 and was not considered further. The HFSS model for the six-sectioned, 90 GHz filter is shown in Figure 69.

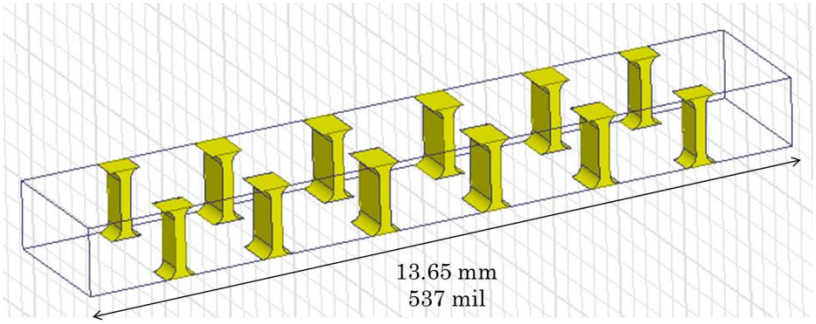

Figure 69: HFSS Model of a Six-Section, Maximally Flat, Inductive Iris, 90 GHz Waveguide Filter

Once the filter designs were completed in HFSS, the models were imported into Solidworks and the physical housings were designed. Figure 70 shows the three filter prototype models in Solidworks. Each filter measures approximately 0.75" x 0.75" x 0.6" (19 x 19 x 15 mm).

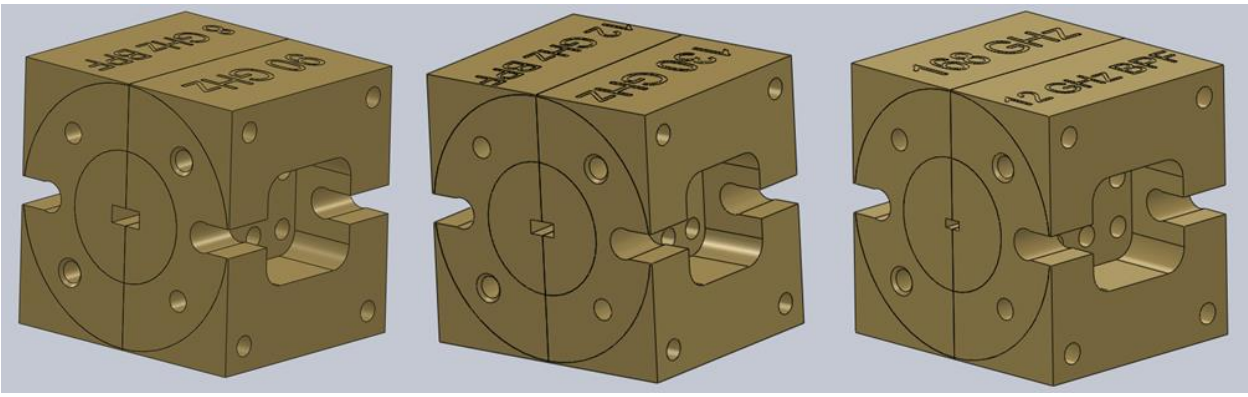

Figure 70: Band Definition Filter Prototype Solidworks Models

The filter housings were designed as prototypes which could also be used in the final assembly if the measured performances meet the requirements, saving both money and time. One feature of the filters is the pockets on each of the two sides allowing the waveguide capture screws, which attach the filters to other components, to be mounted from two different directions. This eliminated the need for extra waveguides between the MCMs and filters if the prototypes were to be used in the final assembly. Once the prototype designs were completed in Solidworks, the filters were machined at Zen Machine. The filters were made from out of brass and gold plating was not necessary as attenuation was not critical to avoid at this stage.

5.3.4 Band Definition Filter Measurements

The completed 90 GHz waveguide BPF prototype is shown in Figure 71. The 90 GHz filter was measured at CSU and the 130 GHz and 168 GHz were measured at JPL where VNAs up to WR-5 were available. Since the filters are two-port

networks, a simpler test bench was needed in comparison to the coupler test bench where matched loads and multiple measurements were needed to fully characterize the component.

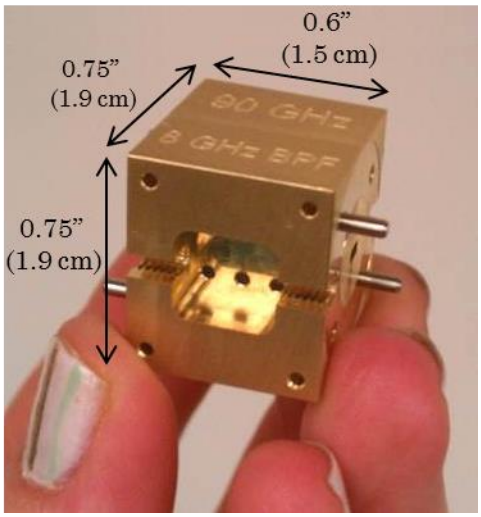

Figure 71: Machined 90 GHz Band Definition Filter Prototype

The measured results compared with the simulated performances are given in Figure 72, Figure 73, and Figure 74 for the 90 GHz, 130 GHz, and 168 GHz BPF, respectively.

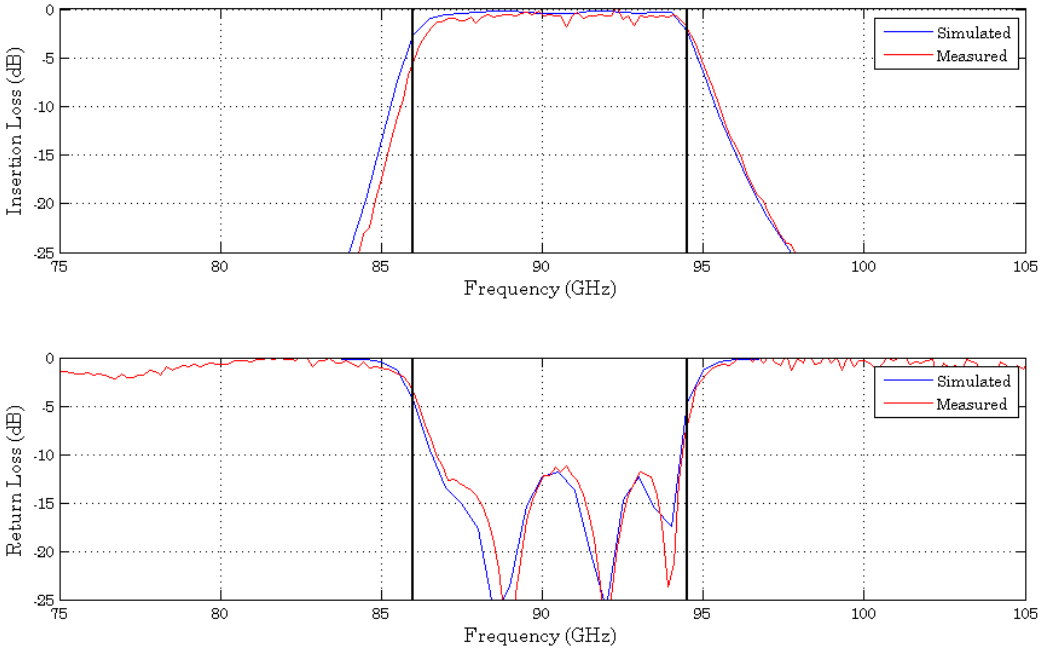

Figure 72: 90 GHz Waveguide BPF Measured vs. Simulated Performance

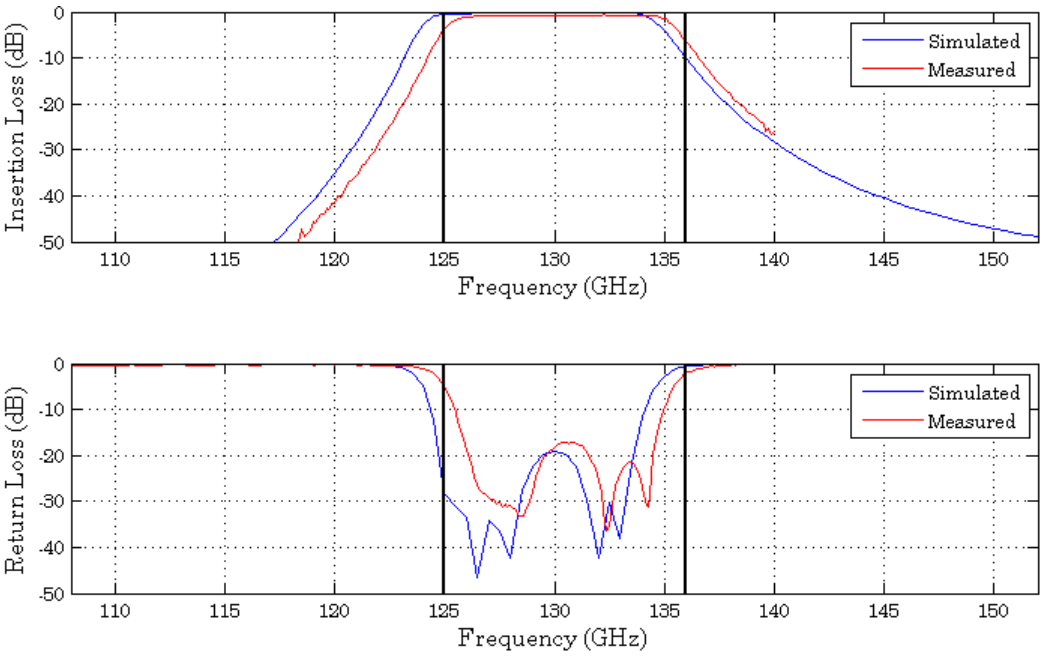

Figure 73: 130 GHz Waveguide BPF Measured vs. Simulated Performance

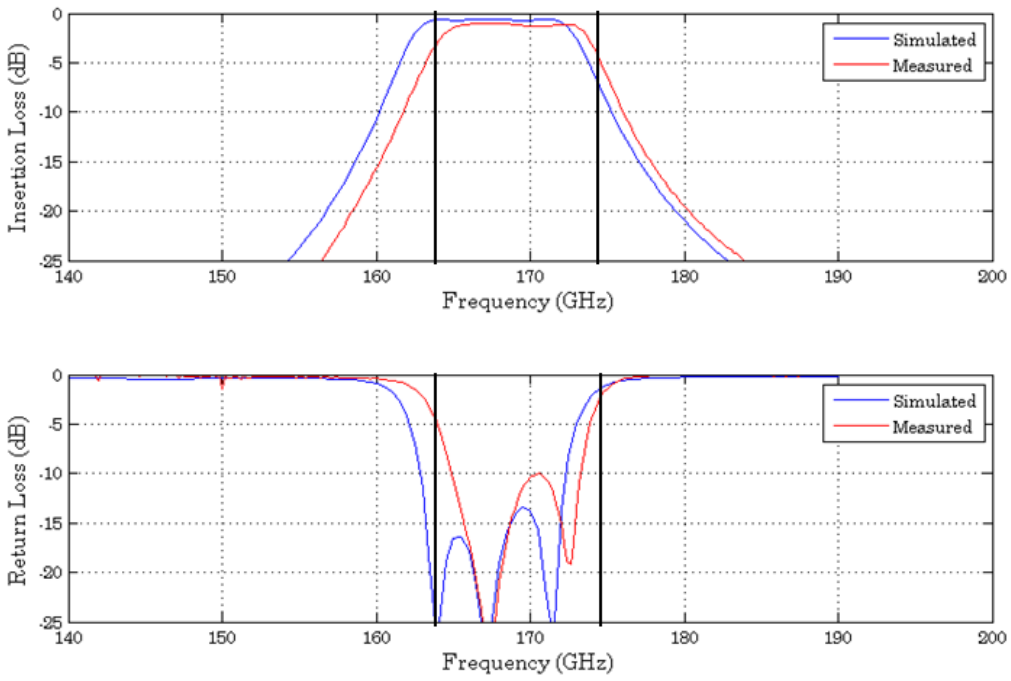

Figure 74: 168 GHz Waveguide BPF Measured vs. Simulated Performance

The measured and simulated performances of the filters matched very well for the 90 GHz and 130 GHz filters. Both showed sharp roll off and flat passbands as predicted in the HFSS simulations. Both filters had approximately 1 dB insertion loss and greater than 10 dB return loss over the pass band. The 168 GHz filter did not match as well to its simulated results as the lower frequencies did. After further investigation, burrs were discovered on some of the irises of the filter like the one in Figure 75.

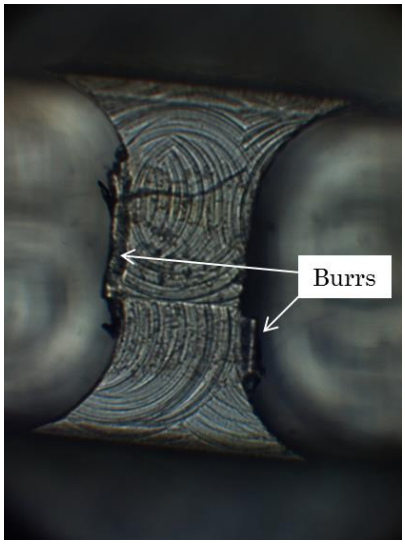

Figure 75: Burrs on Iris of 168 GHz BPF

Although the measured performance of the 168 GHz BPF filter did not exactly match the simulated results, its performance is sufficient for this project. The insertion loss is approximately 1.3 dB and the return loss is greater than 10 dB across the passband.

5.4. Detector Diode Modules

Directly after the band definition filters are the detector diodes and video amplifiers. Modules were designed to house the detector diodes, their biasing circuit and video amplifiers. The RF input to the detector diodes in waveguide and the output is feedthroughs used to interface the detector diode block with the ABEB.

5.4.1 Background

The diode detectors are used to convert the output power of the radiometers into a corresponding voltage which is the signal that is sent to the digitizer. Though the diode detector is the last component in the RF chain, the output voltage is dependent on the performance of the diode detectors and the components that precede it as seen in (V.2).

$$V_{out} = kBG\beta T_{sys} \tag{V.2}$$

where k is Boltzmann's constant, B is the bandwidth defined by the band definition filters, G is the overall gain of the MCMs, β is the diode detector sensitivity, and T_{sys} is the noise temperature of the system. The diode detectors used for the mm-wave channels were purchased from Virginia Diodes, Inc. and have a sensitivity of $\beta = 2$ mV/μW [55].

5.4.2 Design Considerations and Machining

These diode detectors typically come in a prepackaged unit; however, because of the strict size constraint custom housings needed to be designed. The diode detector housings are quite simple in that they only consist of an input waveguide, trench for waveguide-to-microstrip transition and a single diode detector and its biasing, printed circuit board (PCB), and output feedthroughs. The input waveguide and diode detector are quite small and only take up about 1/3 of the space in the

modules. The overall size of the diode detector blocks is ultimately driven by the PCB that provides biasing and post-detector amplification as seen in Figure 76 for the 90 GHz detector block.

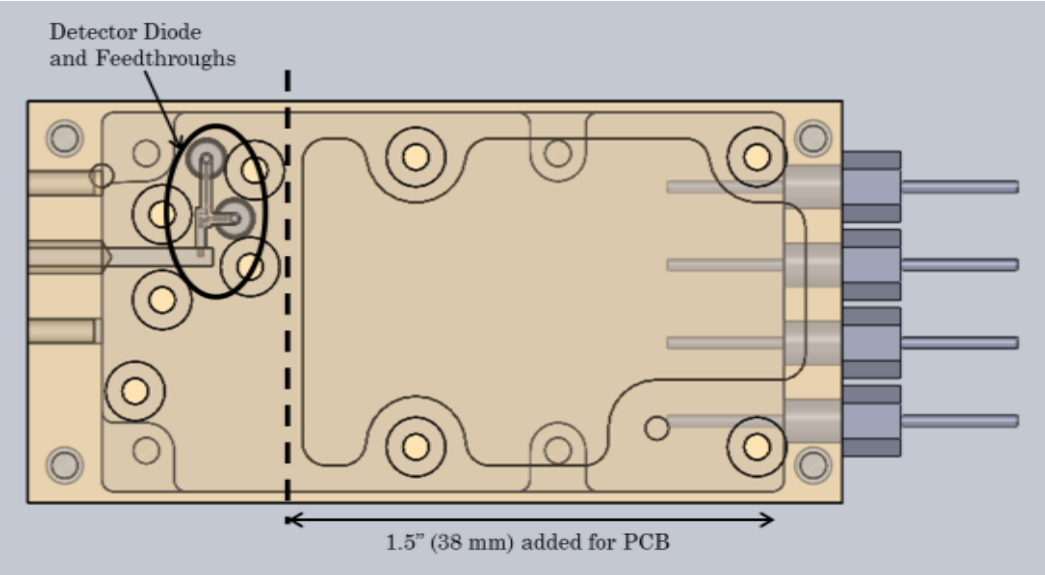

Figure 76: 90 GHz mm-Wave Diode Detector Block with Added Length for PCB

Due to the simplicity of these detector diode modules, many of the features could be made identical on all three blocks. These features were the outer dimensions, PCB mounting posts, capacitive feedthrough outputs and part of the screw patterns that hold the two halves of the split-block together. The only differences between the modules were the input waveguides, RF trenches, and biasing feedthrough locations. Although these may seem like moot points, these identical features allow the machinist to write one computer numerical control (CNC) program for most of the machining that needs to be done. Additionally, the same PCB design was used for all three modules.

5.5. Multi-Chip Module Design

The multi-chip modules (MCMs) house the monolithic microwave integrated circuits (MMIC) of the radiometer. The input to the MCMs is from the tri-frequency horn, which comes before the MCMs, splits the signal into three frequency bands for the 90 GHz, 130 GHz, and 168 GHz MCMs. The components that populate MCMs amplify and filter the incoming single, perform internal calibration, and cancel out gain fluctuations.

5.5.1 MCM Design Considerations and Process

The MCM designs were quite complex and many different parameters needed to be taken into consideration and accommodated for in their design. Design efforts focused on minimizing the mass and footprint size of the mm-wave MCMs and to improve on the ACT-08 MCM designs. All three MCMs, in terms of performance and physical dimensions, are summarized at the end of this chapter and the 90 GHz MCM is used as an example throughout this section. The conclusions taken from the 90 GHz MCM examples can be applied to the 130 GHz and 168 GHz MCMs as well.

5.5.1.1 MCM Inputs, Outputs, and Outer Dimensions

The first step in designing the MCMs was deciding where they needed to be mounted in the system and how they would connect with the other components that make up the radiometers. The radiometers needed to fit on an 8.9” x 7” (226 x 178

mm) plate that also holds the antennas for the microwave and sounding radiometers. This restriction in size is discussed in Chapter II. The tri-frequency horn main beam was optically aligned with the foci of the parabolic reflector so there was no flexibility in the placement of the feedhorn. The MCMs are the next component in the RF chain after the feedhorn and their placement was largely decided on by the location of the three outputs of the tri-frequency horn. This resulted in the configuration shown in Figure 77 with the 168 GHz module stacked on the 130 GHz module and the 90 GHz module next to the 168 GHz module. The path length between the antenna output and first gain stage in the MCM needed to be minimized in order to keep the receiver noise low so custom waveguides were designed.

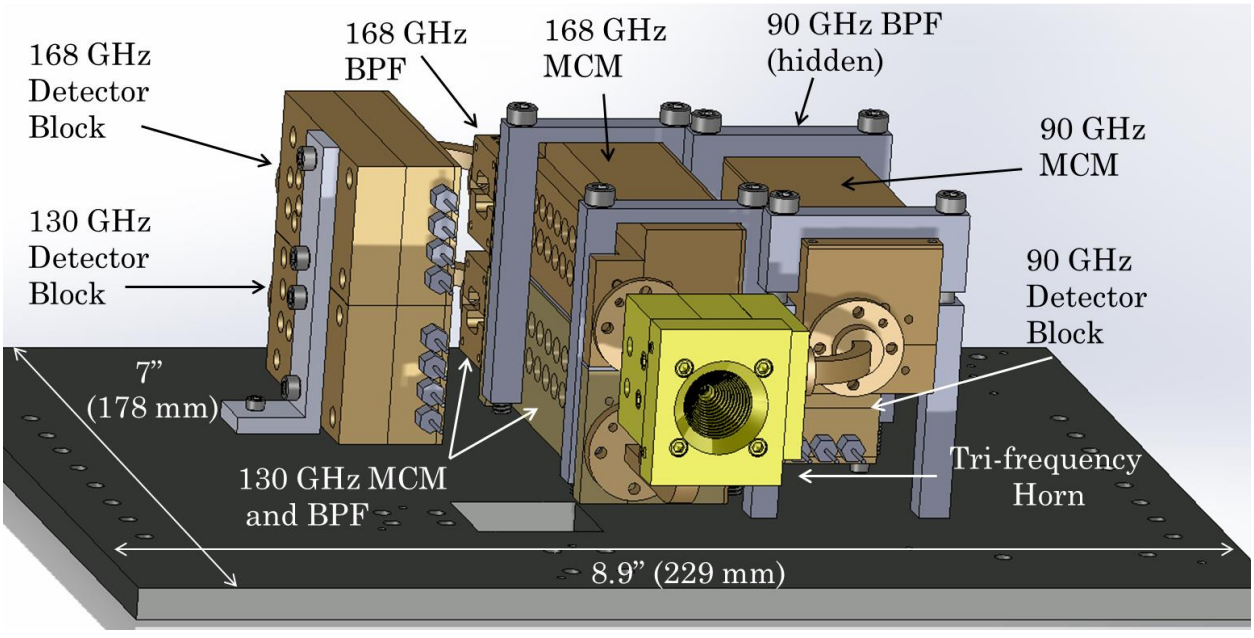

Figure 77: mm-Wave Optical Bench Layout

The inputs locations of the MCMs were determined by several factors. They needed to be close enough to one another to minimize their footprint but spaced out enough to make assembly possible. The addition of the second input to the MCMs also needed to be accommodated for. Typical waveguides and split-block components have a standard UG-387 face, shown in Figure 78 [56]. The alignment pins mitigate the risk of misaligning the two mating rectangular waveguides which can cause reflections, standing waves, and additional losses especially at higher frequencies [57].

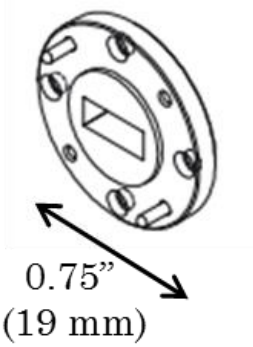

Figure 78: Standard UG387 Rectangular Waveguide Face [56]

However, because the two inputs to each of the MCMs were spaced so close to each other, some of the alignment pins had to be removed. If spaces for all of the alignment pins had been designed into the MCM housings, it would have significantly increased the mass and size of each MCM.

The band definition filters, discussed in Section 5.3, were designed to be mounted directly to the MCMs. The brackets holding the MCMs to the optical plate do not connect directly to the modules, but instead clamp them in place as can be seen in Figure 77. This allowed the 90 GHz diode detector block to be mounted under the 90 GHz module. The 130 GHz and 168 GHz diode detector blocks are stacked similar to their respective MCMs and sit adjacent to the modules.

5.5.1.2 RF and Biasing Trenches

The inputs to the MCMs are in waveguide and the MMIC components that follow are in microstrip and a waveguide-to-microstrip transition was used to interface these two different methods of propagation. Starting at the waveguide-to-microstrip transition, and encompassing the following microstrip components, is a cavity referred to as the RF trench. Adjacent to the RF trench are the biasing trenches which house the transmission lines and feedthroughs used to bias the components. The RF and bias trenched are defined in Figure 79.

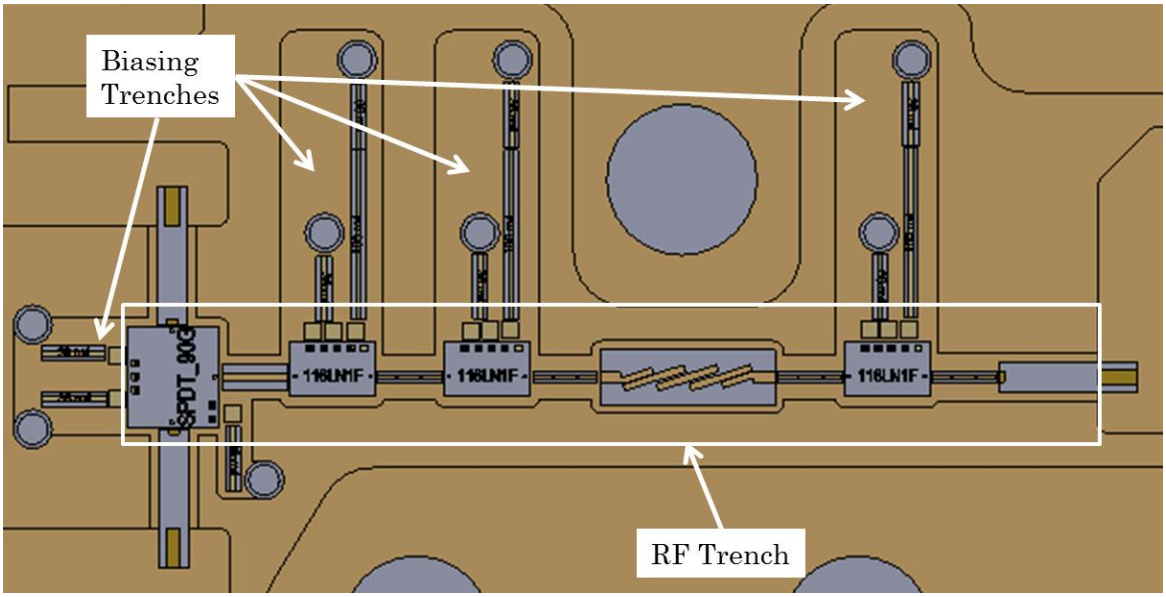

Figure 79: 90 GHz MCM RF and Bias Trenches

Once the two halves of the split-block are assembled, the RF and bias trenches can act as a waveguide which has multiple effects on the performance of the components. If the dimensions of the trench are not carefully designed so that the waveguide's cutoff frequency is far above the MCMs operating frequency, a feedback path can be created in the amplifiers causing them to oscillate [5], [6]. The RF trenches adjacent to the RF trench can act as resonators as well. These concerns were addressed by making the cavity thinner in between each amplifying stage in order to increase the cutoff frequency and the biasing trenches were stuffed with absorber after fabrication.

A final concern introduced by the cavity dimensions was the lid height. The lid height can significantly impact the performance of the mm-wave components by changing their capacitance per length, and therefore, their impedance [58]. This

effect on impedance is quite complex and was therefore was primarily modeled, and corrected for, in HFSS.

5.5.1.3 RF Chain Customization

The height of the cavity can impact the LNAs and their gain was expected to slightly differ than the measurements done in a test cavity. To mitigate the risks associated with this uncertainty, it was desired to have the flexibility to change the gain. The RF chains in the MCMs were designed to each have three pockets to fit their respective LNAs. The sizes of the pockets were designed in such a way that it could fit an LNA, transmission line, or attenuator. This allowed the ability to modify the final RF chain, and therefore, customize the overall gain, within limits, to match the needed output power to the diode detectors.

5.5.1.4 Biasing and PCB Space Allocation

The printed circuit boards (PCBs) that bias the mm-wave components in the MCM are enclosed in the bottom half, or carrier, of the MCM split-blocks. The features of the integrated PCBs are shown in Figure 80 and should be referenced for the following description. The PCB cavity is separated from the input waveguide and trench with a thick layer of brass. In the case of the 90 GHz MCM, the separation between the PCB cavity and input waveguide was 120 mils. Feedthroughs are used to connect the PCB biasing pads to the microwave components.

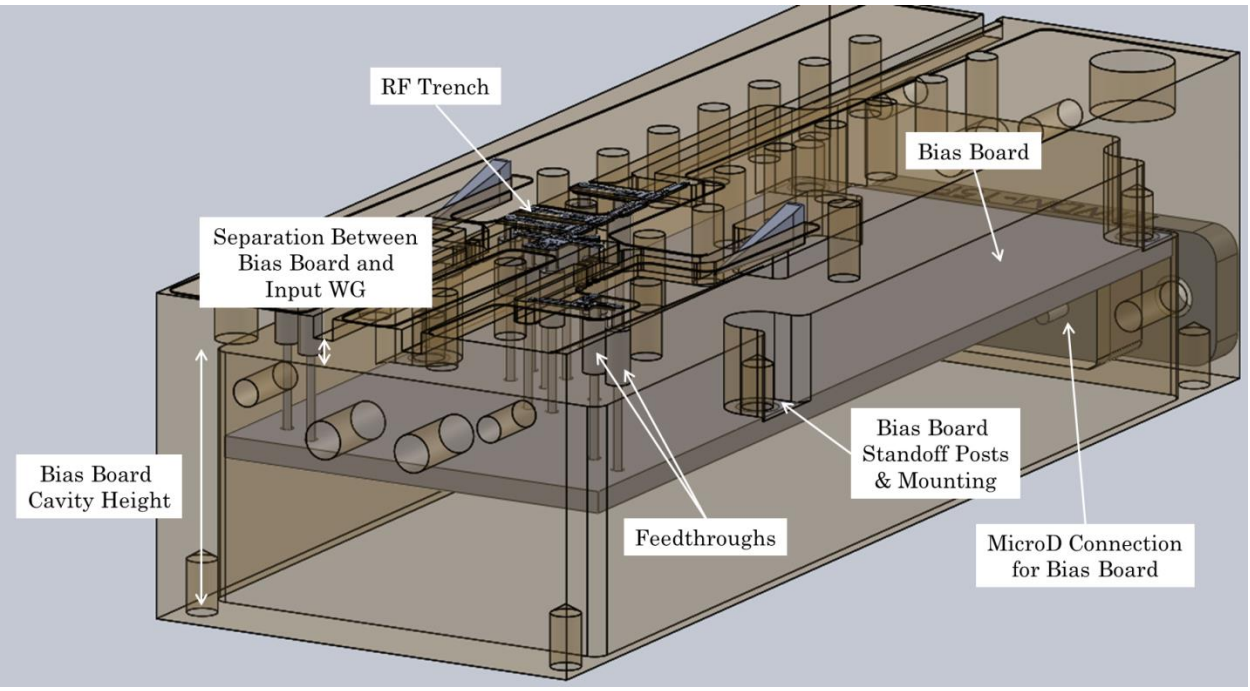

Figure 80: MCM Bias Board Diagram

Observed in Figure 80, the PCBs significantly increased the size of the MCMs. The height of the cavity had to be large enough to fit the components on both sides of the board and the microD connector that powers and controls the board [59]. Standoff posts were added to lift the PCB off the base of the cavity for the components on the backside and the microD connector was positioned above the bias board which left ample room for the components on the top side of the board. The total cavity height for the 90 GHz MCM is 0.575" (14.6 mm).

The sizes of the mm-wave components are quite small at the mm-wave operating frequencies and take up very little space as desired. The newly designed and integrated couplers, described in Section 5.2, are located before the RF components

and are also relatively compact. The combined length of the input waveguide, coupler, and RF trench in the 90 GHz MCM totals to 1.45" (36.8 mm). The bias board on the other hand is 2.56" (65.1 mm) in length. Figure 81 shows the impact that the length of the PCB had on the overall length of the MCM.

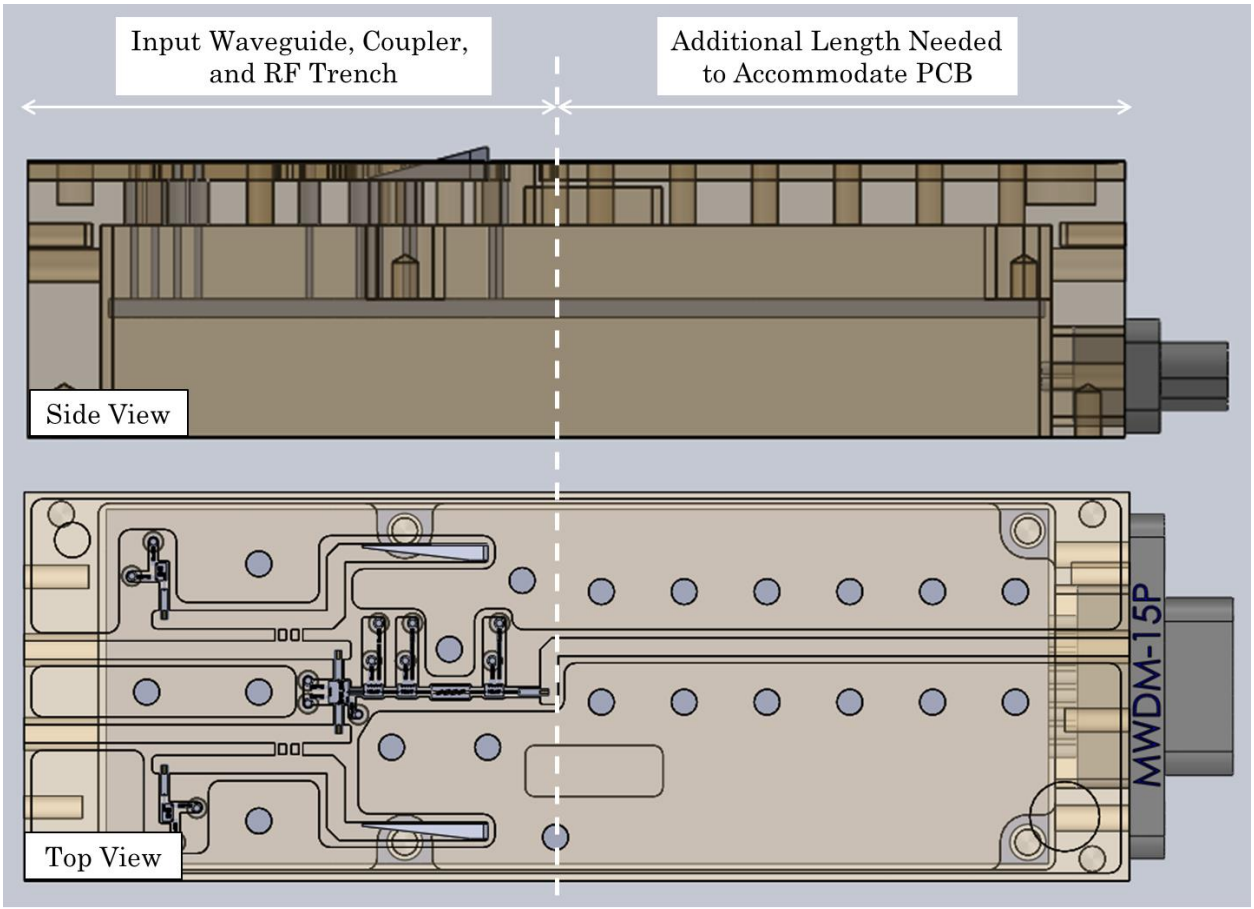

Figure 81: Transparent View of 90 GHz MCM Added Length Due to PCB

The inclusion of the PCB into the MCMs approximately doubled their size. To accommodate this additional length, part of the internal structure of the MCM had to also be modified. The input waveguide and couplers were not modified because

additional length could add losses before the first gain stage compromising the performance of the radiometers. To accommodate the PCB length with minimal impact, the output waveguides were lengthened.

5.5.1.5 Split-block Interface

The MCMs were designed to be machined in split-block and ultimately needed to be mated together. The quality of the interface between the two halves has a significant impact on the performance of the MCMs. A bad interface can add extra losses to the waveguide portion of the MCM and affect the performance of the microstrip components due to their sensitivity of cavity dimensions. A few design features help reduce these risks associated with the interface of the split-block design. Two alignment pins are used so the features on the two halves line up correctly. The screws used to compress and hold the two halves together closely follow the shape of the interior features as can be seen in Figure 82.

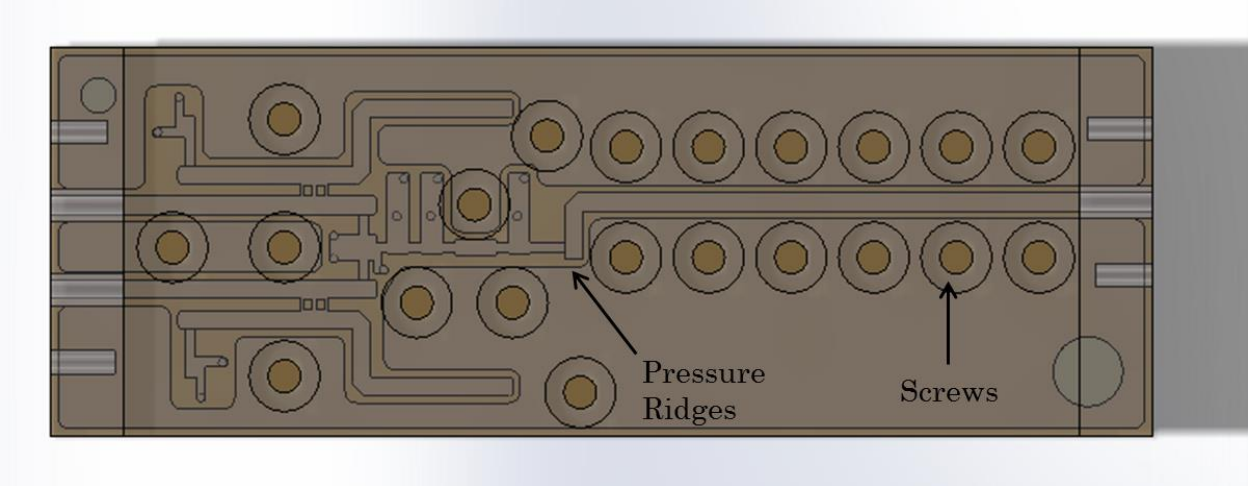

Figure 82: 90 GHz MCM Screw Pattern

The addition of pressure ridges surrounding the waveguides and trench localize the compression force of the screws around these critical areas ensuring a good seal where the two halves interface.

5.5.1.6 Machining Considerations

The physical limitations and cost factors of machining were also taken into consideration in the MCM designs. In addition to the minimum tolerances that the machinist can accomplish, the drill bits used to machine split-blocks are circular and have a defined diameter that can be seen in the machined features. The diameter of the drill bit needs to be included in the design and simulated in HFSS as it can have an impact on the radiometer performance. To minimize costs associated with machining, a strict tolerance of 0.001" (0.0254 mm) and small-diameter drill bits were specified to be used in the waveguide and RF trench features only. All of the other features, such as the PCB cavity and pressure ridges,

did not require these strict guidelines and, therefore, allowed the machinist to use larger drill bits and less strict tolerances in these areas.

5.5.1.7 Completed MCMs

After the MCMs were machined and gold plated they were sent to JPL for population. Experts at JPL were needed for this important step because if the components are not properly installed, the performance of the MMIC components could be negatively impacted [13]. In addition to the difficulty that arises with the small size of the components, the wire bonds can be made too long and act as an inductor Additionally, if excess epoxy is used to attach the MMICs to the trench the lid height can be reduced. A close up image of the 168 GHz populated MCM is shown in Figure 83 compared with the original block diagram design.

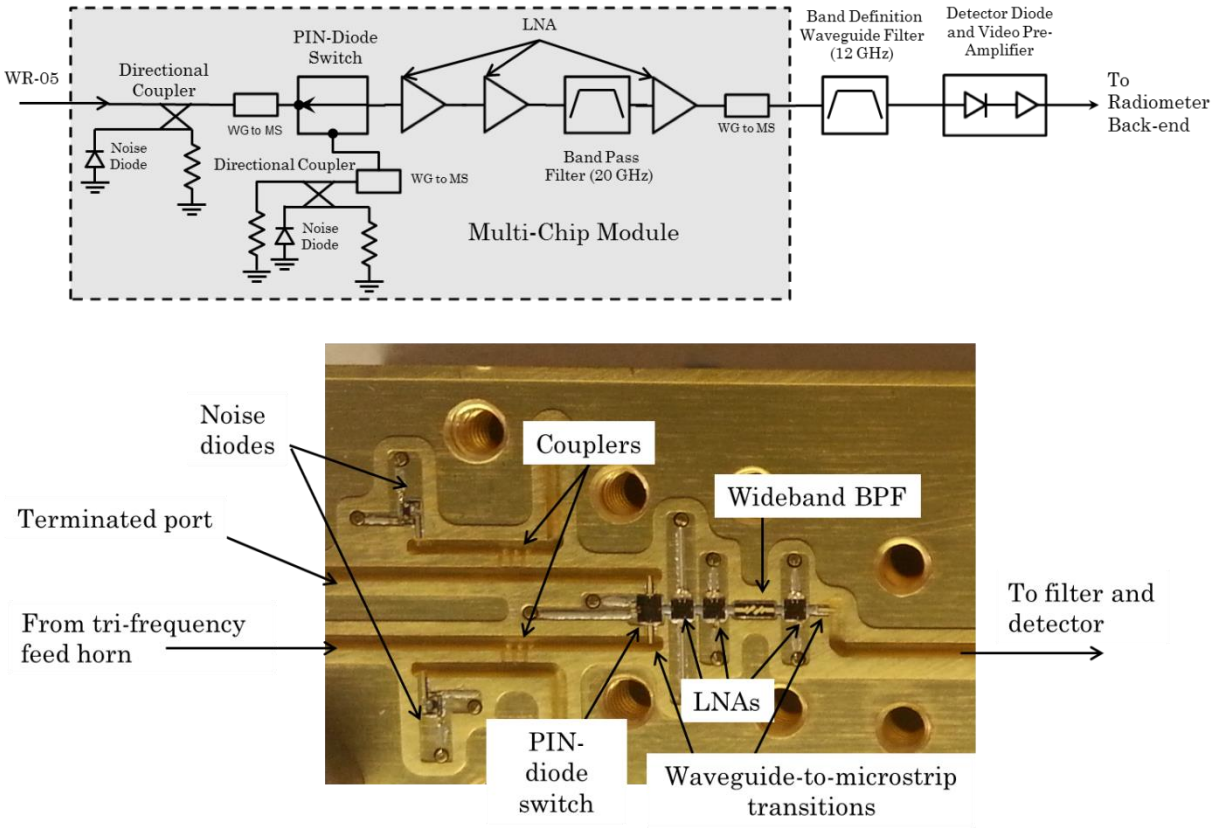

Figure 83: 168 GHz Populated MCM and Original Block Diagram Design

The complete, populated MCMs carriers at 90, 130 and 168 GHz are shown in Figure 84. Additional absorber was placed in some of the biasing trenches to minimize standing waves at the LNAs.

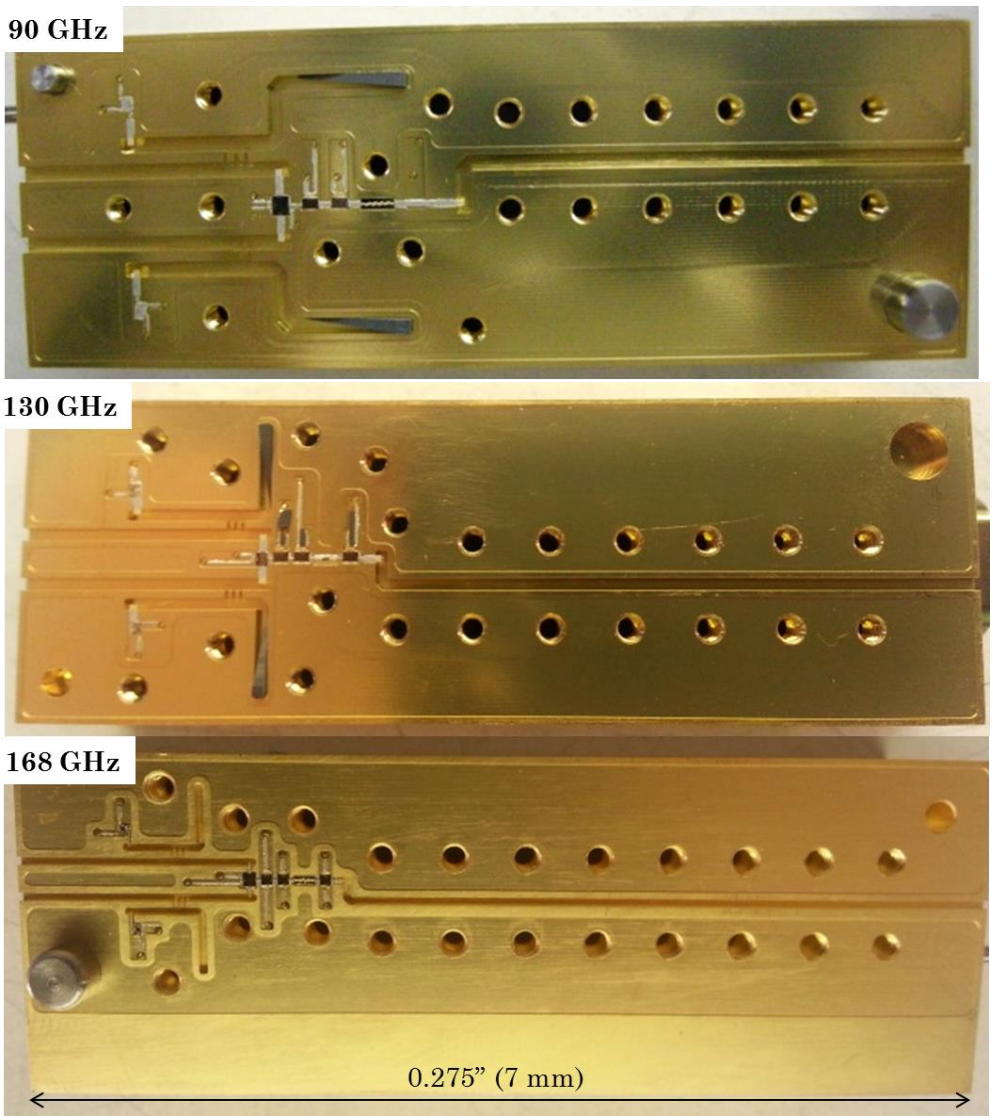

Figure 84: Assembled mm-Wave Multi-Chip Modules

The outer dimensions and final weights of the three MCMs are given below in Table 7.

Table 11: Outer Dimensions and Weight of mm-Wave MCMs

Radiometer Center Frequency	Length	Width	Height	Weight (g)
90 GHz	2.9" (74 mm)	1.1" (28 mm)	1.1" (28 mm)	523
130 GHz	3.0" (76 mm)	1.0" (25 mm)	1.1" (28 mm)	522
168 GHz	3.0" (76 mm)	1.1" (28 mm)	1.1" (28 mm)	498

After the MCMs were completed, they were tested and characterized at JPL.

5.5.2 MCM Measurements and Characterization

Once the MCMs were finished at the machine shop, they were sent to JPL to populate and perform initial system measurements. The gain and system noise temperature of the MCMs were characterized across their respective frequency bands. Both of these parameters are important in determining the radiometric resolution of the system and ensuring the output power is correct for the detector diodes to operate in the square-law region.

To measure the MCM before it is put in its final configuration with the rest of the system, a standard gain feed horn was used instead of the tri-frequency horn at the

input. The output signal was down converted and measured by a power detector. Hot and cold loads of known temperature were put at the input of the standard gain feed horn. The temperature of the hot load, T_{Hot}, observed by the receiver is approximately room temperature, 300 K, and the temperature of the cold load, $T_{Cold,}$ is approximately the temperature of liquid N_2, 77 K. Because the radiometers operate in the frequency range where the Johnson-Nyquist approximation can be applied, the linear relationship in Figure 6 between voltage and temperature is used [9].

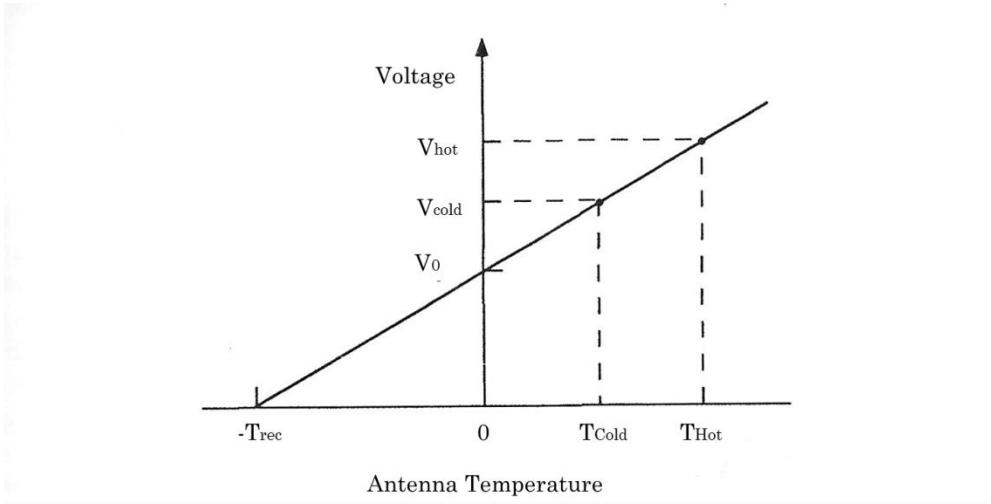

Figure 85: Output Voltage and Antenna Temperature Relationship Used in Calibration [13]

The gain of the device under test (DUT), in this case the MCMs, is found from the linear slope that connects the hot and cold measured output voltages. The noise introduced by the MCM, T_{rec}, can be found find by finding the x-intercept of the line. The typical test bench for the Y-factor measurements is shown in Figure 86.

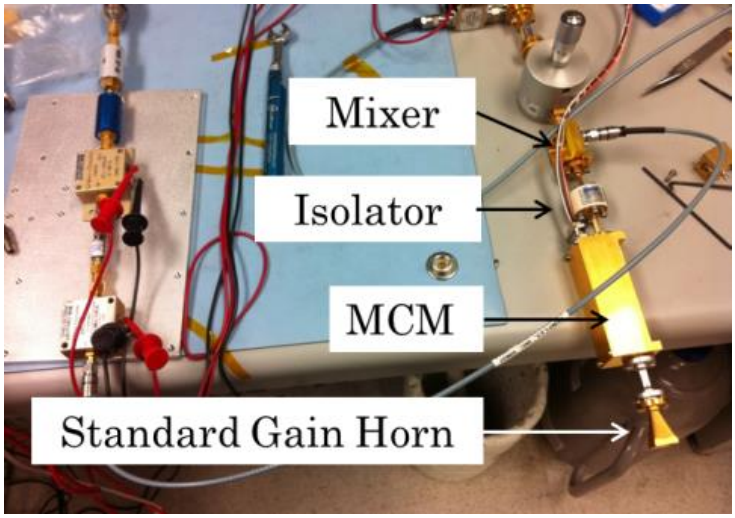

Figure 86: mm-Wave Radiometer Y-Factor Measurements Test Bench

This setup will perform Y-factor measurements across the respected band for each of the three frequencies [13]. After some post-processing of the measured data, the gain and noise temperature can be found for each of the three modules. The results of these measurements for the 90, 130, and 168 GHz MCMs are shown in Figure 87, Figure 88, and Figure 89, respectively.

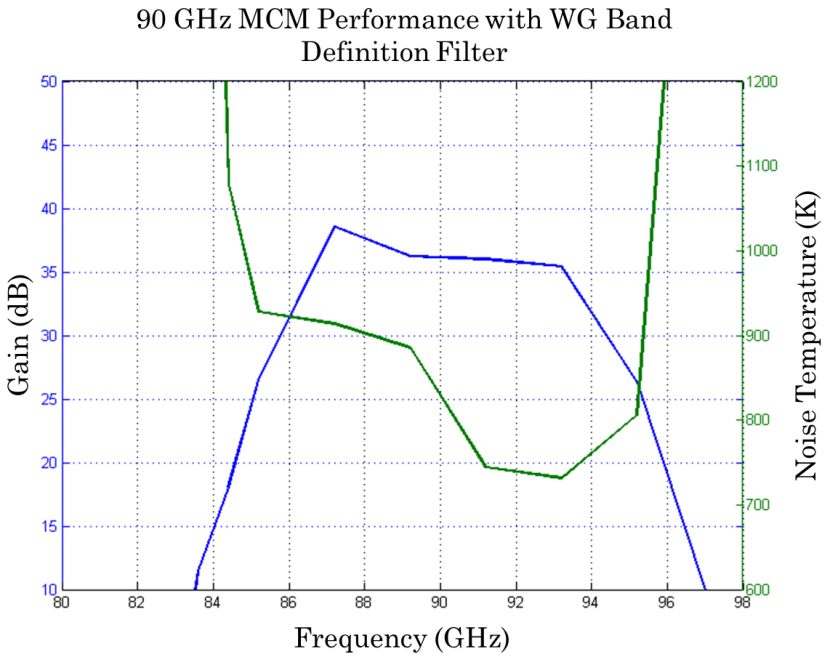

Figure 87: 90 GHz MCM Performance with WG Band Definition Filter

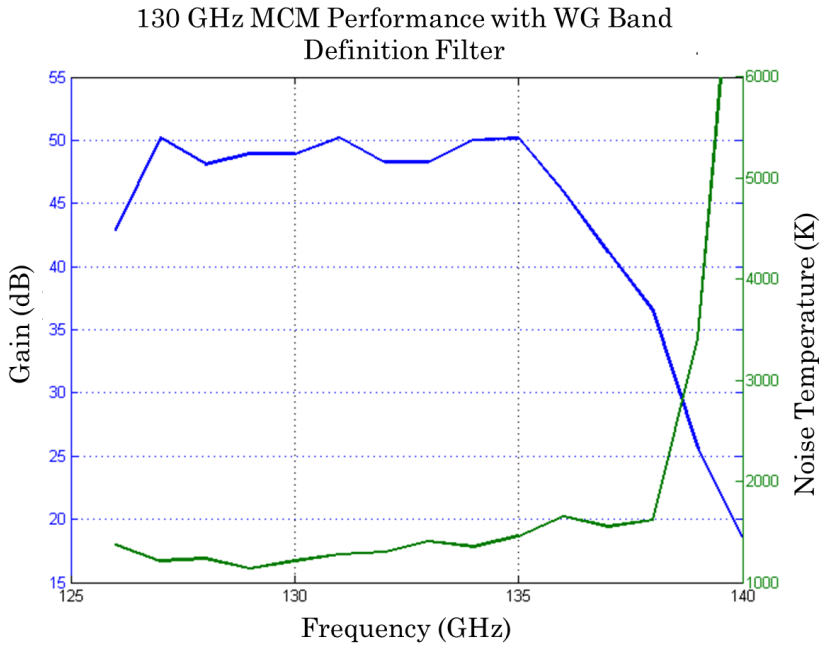

Figure 88: 130 GHz MCM Performance with WG Band Definition Filter

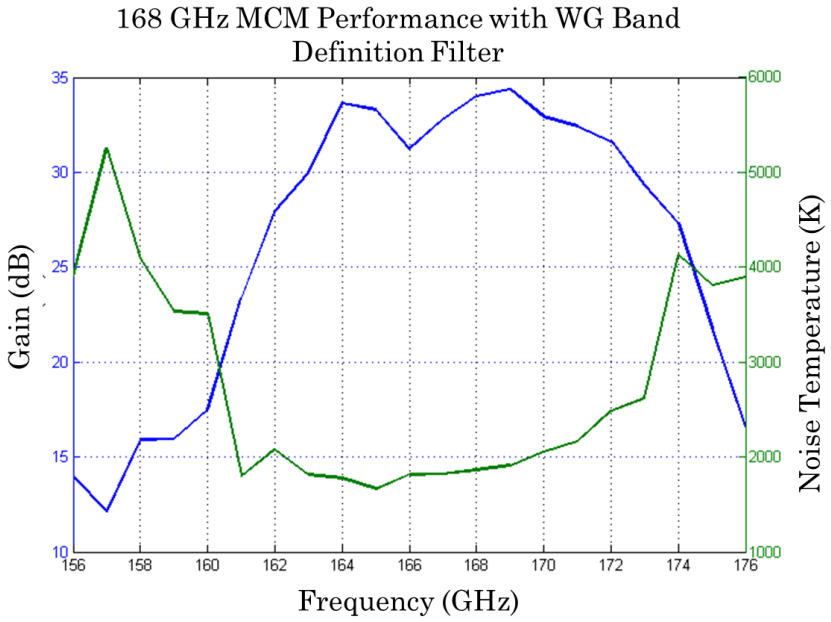

Figure 89: 168 GHz MCM Performance with WG Band Definition Filter

The performances shown in the three plots are summarized in Table 12.

Table 12: Summary of MCM Initial Lab Performance

Channel Frequency (GHz)	Average Gain (dB)	Average Noise Temperature (K)
90	36.5	818.7
130	46.8	1369.5
168	31.1	2142.7

The results of these measurements allowed each of modules' output power to be tuned individually for the detector diodes to operate in the square law region. Additionally, the noise introduced by the receiver, T_{rec}, was found for each MCM.

5.6. Full System Laboratory Measurements

Although, Y-factor measurements were done on the MCMs individually, more comprehensive measurements are needed to characterize the radiometers as a whole.

5.6.1 mm-Wave Radiometer Y-Factor Measurements

The test setup used in the comprehensive laboratory measurements are shown in Figure 90. The components of the mm-wave radiometers, from the tri-frequency horn to the diode detectors, are connected to each other as they would be on the optical plate in their final configuration. The analog back-end board (ABEB) and field-programmable gate array (FPGA) are copies of the versions used in the final system and are used to digitize the data [21].

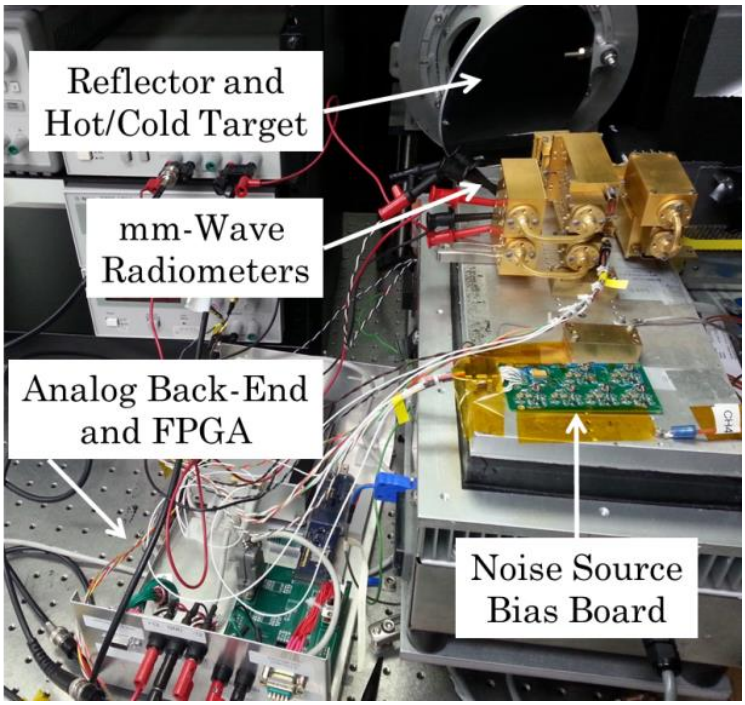

Figure 90: Test Bench for Full System Laboratory Measurements

The noise source bias board is used to fire the noise diodes in the coupled ports inside the MCMs. Using the noise source bias board and the MCM bias board, the SPDT PIN-diode switch and noise diodes were synchronized to produce the following viewing sequence: Antenna (6 ms) > Antenna + Noise Diode (1 ms) > Reference (1 ms) > Reference + Noise Diode (1 ms). During this sequence, the scene observed by the tri-frequency horn was also switched between a hot (T_{hot}≈300 K) and cold (T_{Cold}≈77 K) target. The final results of this test are the digitized output voltages of the diode detector blocks with respect to time. These output voltages are plotted for the 90, 130, and 168 GHz radiometers in Figure 91, Figure 92, and Figure 93, respectively.

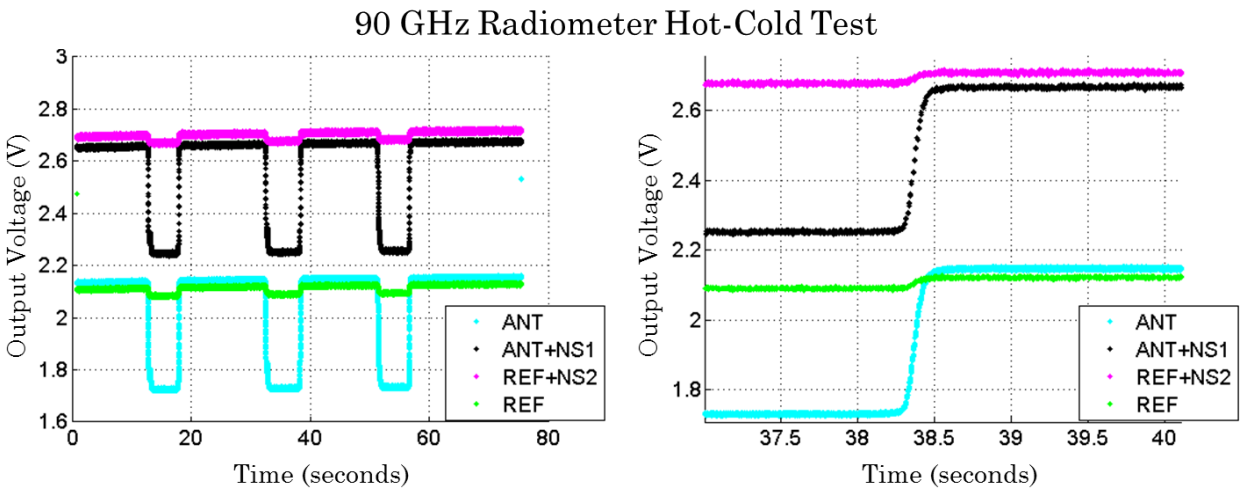

Figure 91: 90 GHz Radiometer

Hot-Cold Measurements with Two Different Time-Scales

The plot on the right of Figure 91 shows a zoomed version of the 90 GHz radiometer output voltage from the left. In this zoomed version, it can be seen that as the noise diodes are fired on each port, ANT+NS1 and REF+NS2, a change can also be seen in the opposite port, ANT and REF, respectively. This behavior shows that the isolation of the switch is not as high as it needs to be. It is expected for the REF and ANT voltage to be the same; however, there is a small discrepancy between these values as can be seen in Figure 91. This variation between the two output voltages is small and is most likely due to small variations between the fabricated noise diodes.

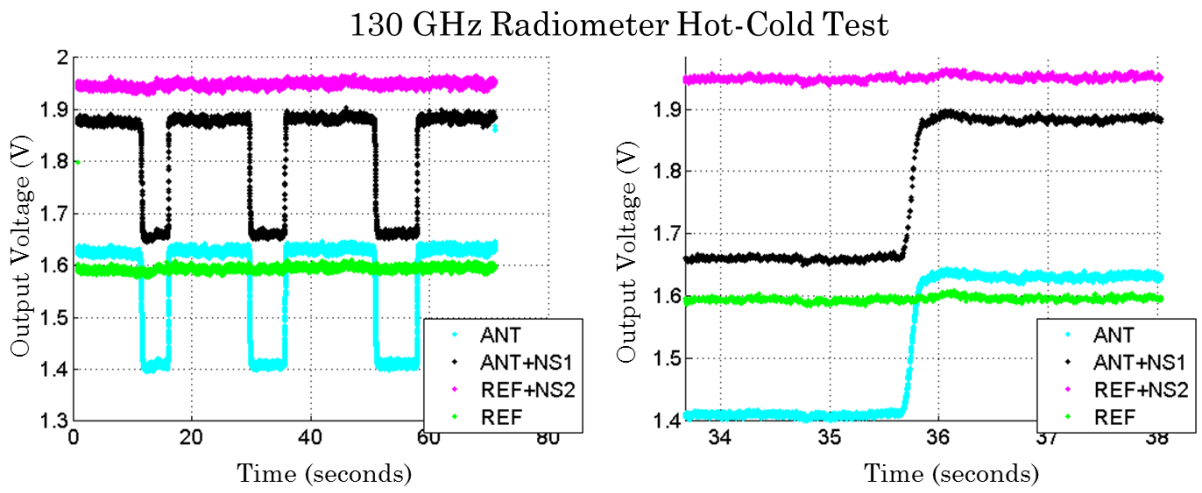

Figure 92: 130 GHz Radiometer Hot-Cold Measurements with Two Different Time-Scales

The plot on the right of Figure 92, which is a closer view of the plot on the left, shows that the 130 GHz switch did not suffer the same isolation problem as the 90 GHz module did. Similar to the 90 GHz radiometer, there is a small discrepancy between the ANT and REF output voltages.

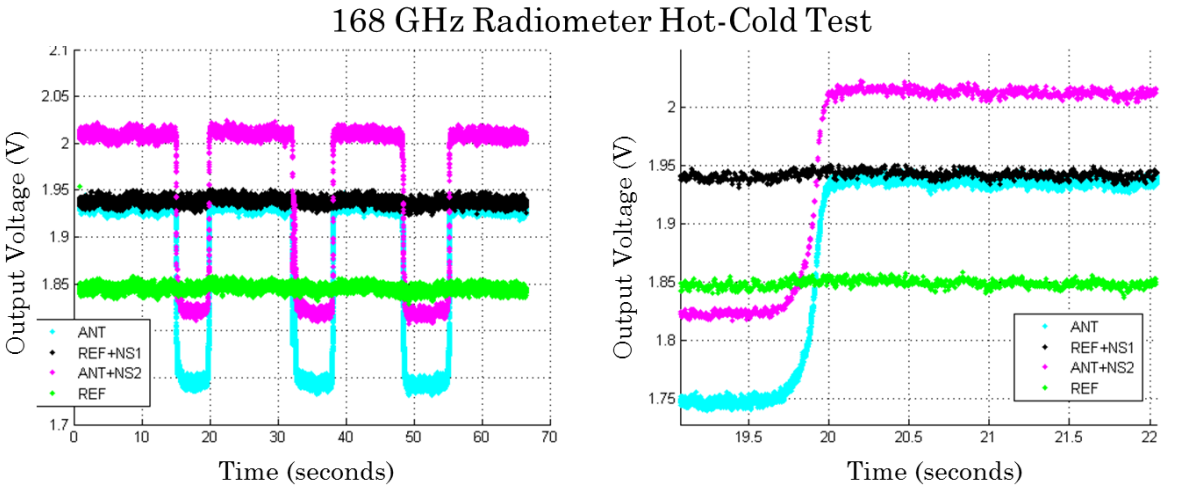

Figure 93: 168 GHz mm-wave Radiometer Hot-Cold Measurements with Two Different Time-Scales

Figure 93 shows the 168 GHz hot-cold measurements on two different time scales. The 168 GHz switch showed no problem with isolation; however, the difference between the ANT and REF output is much larger than what was seen on the 90 and 130 GHz radiometers. Although this discrepancy between the two ports is non-ideal, the results of these hot-cold tests allow these differences to be taken into account during post-processing of the data.

In addition to the information that can be inferred by looking at the behavior of the radiometers as its noise diodes are fired and view scenes are changed, we can use the hot-cold Y-factor method to find the gain, noise temperature of the system and noise temperature of the reference port. These calculated values are shown for the three radiometers in Table 13.

Table 13: Summarized Performance of mm-Wave Radiometers

Radiometer	**T_{sys} (K)**	**Gain (K/Volt)**	**T_{ref} (K)**
90 GHz	816	514	281
130 GHz	1310	982	255
168 GHz	2672	1524	160

The overall system temperature for the 90 and 130 GHz radiometers matched closely to the values calculated during the hot-cold tests on the MCMs. The 168 GHz radiometer however showed an increase of almost 400 K compared to the previous

measurement of the MCM Table 12. It is hypothesized that this increase in noise comes from the tri-frequency horn and additional waveguide that were not used on the first MCM test. It would be ideal for the T_{ref} to be close to 300 K to increase the noise deflection. The 90 and 130 GHz radiometers showed T_{ref} values close to 300 K, but the 168 GHz radiometer T_{ref} reached only approximately half of that goal value.

5.6.2 Thermal Stability Tests

The final test to complete the comprehensive lab testing of the mm-wave channels was to characterize their performance over a range of temperatures and test the repeatability. The test bench was modified to that in Figure 94. Each radiometer was tested individually on a thermally-controlled metal plate and a matched load was used at the input ports in place of the tri-frequency horn. The temperature of the plate was then cycled over a range of 20°C and the digitized output voltage of the radiometer was analyzed.

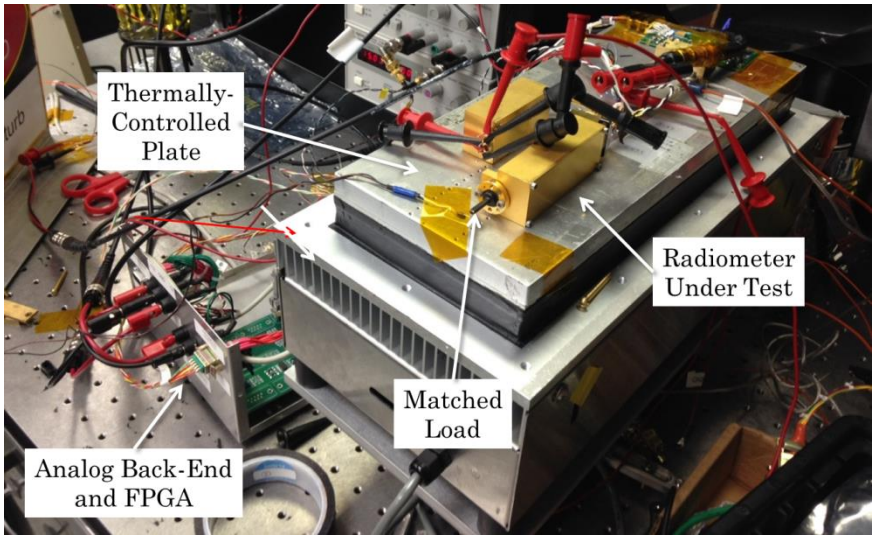

Figure 94: mm-Wave Thermal Control Test Bench

Ideally, the output voltage would be constant as the temperature is cycled; however, the performance of the microstrip components will vary with temperature. The results of this test will allow the modules to be characterized over temperature which will be useful for processing the data. Figure 95 shows the temperature profile of the thermally controlled plate in red and the temperature profile of the radiometer in blue, during these tests. The performances of the radiometers during the temperature cycling are shown in Figure 96, Figure 97, and Figure 98.

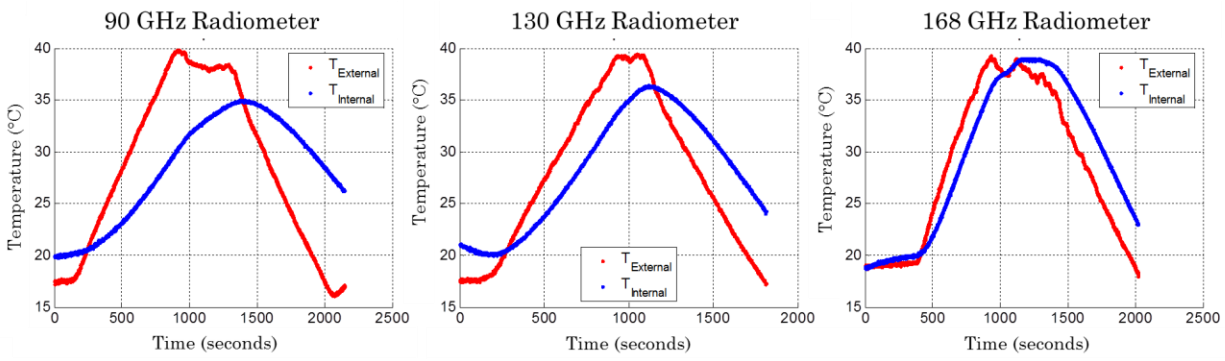

Figure 95: Temperature Profile of Thermal Plate and mm-wave Radiometers

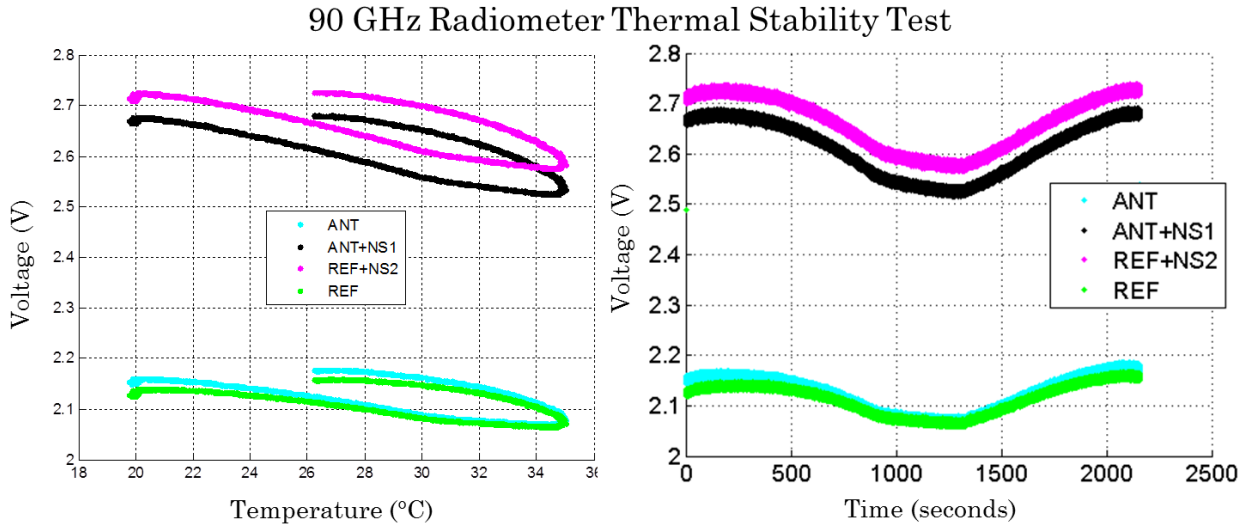

Figure 96: 90 GHz Radiometer Thermal Stability Performance

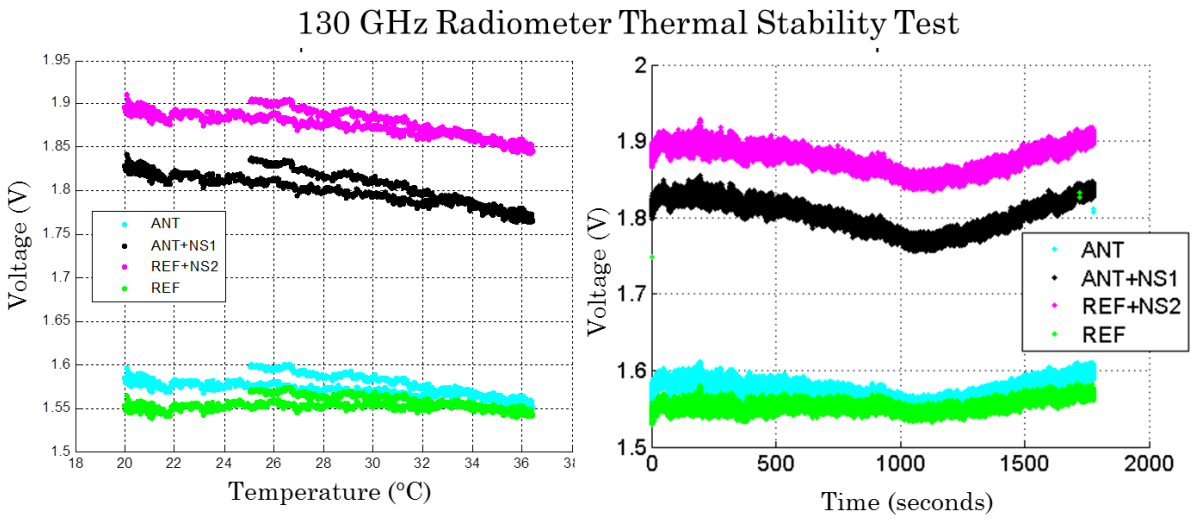

Figure 97: 130 GHz Thermal Stability Performance

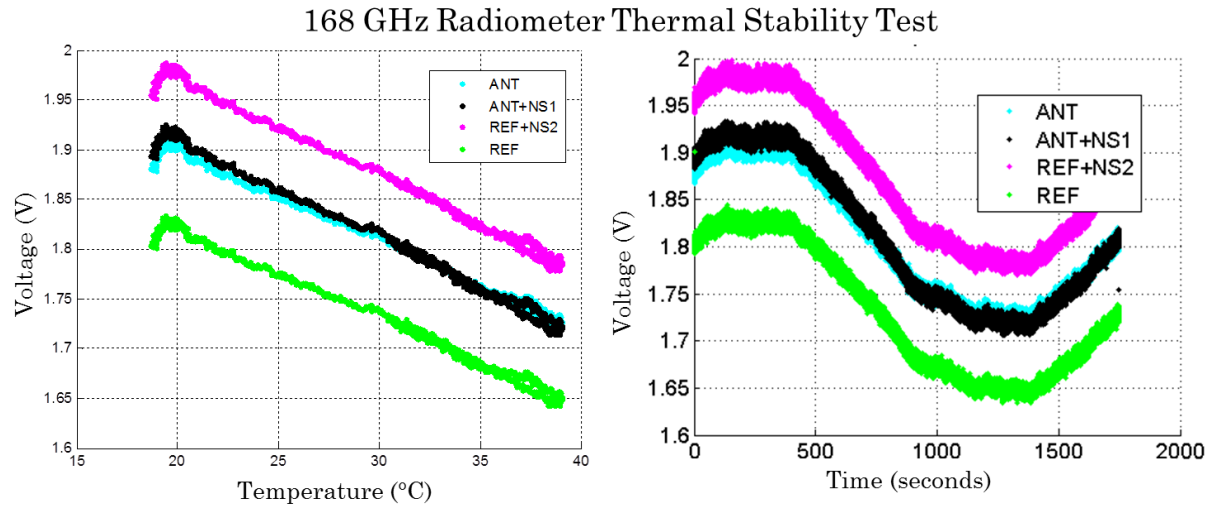

Figure 98: 168 GHz Thermal Stability Performance

The plots on the left show how consistent the performances of the radiometers were while the temperature was ramped back down. Of the three radiometers, the 168 GHz module showed the most consistent performance as the output voltage was almost exactly the same while the temperature was being ramped up as it was

while the temperature was being ramped down. The plots on the right show that while viewing the same scene, the 90 and 168 GHz radiometers output voltage will vary ~5 mV for every 1 °C temperature change and the 130 GHz radiometer output voltage is expected to only vary ~2 mv.

With the mm-wave radiometers sufficiently characterized, they were ready to be integrated with the rest of the system. The next measurements done on these channels were comprehensive field test measurements. The results of these measurements are discussed in the proceeding chapters.

Chapter VI HAMMR System Testing

Near the end of June 2014, all of the radiometers and subsystems were integrated into the High-frequency Airborne Microwave and Millimeter-Wave Radiometer (HAMMR) chassis and tested as a complete system for the first time. A few weeks later in July 2014, the HAMMR system was integrated on a Twin Otter and demonstrated airborne for the first time.

6.1. Outdoor Ground Tests

The purpose of the ground tests was to test the HAMMR instrument as a complete system for the first time and correct any system malfunctions before it was demonstrated airborne.

6.1.1 **Test Setup**

The outdoor ground tests were completed during the week of June 30, 2014. Several days were needed to work out errors discovered during the first few measurements. The HAMMR instrument was set up outside the Microwave Systems Laboratory (MSL) in a shaded area shown in Figure 99. It is necessary to be in a shaded area so the sun doesn't enter the aperture of the instrument and distort the measurements or cause thermal fluctuations.

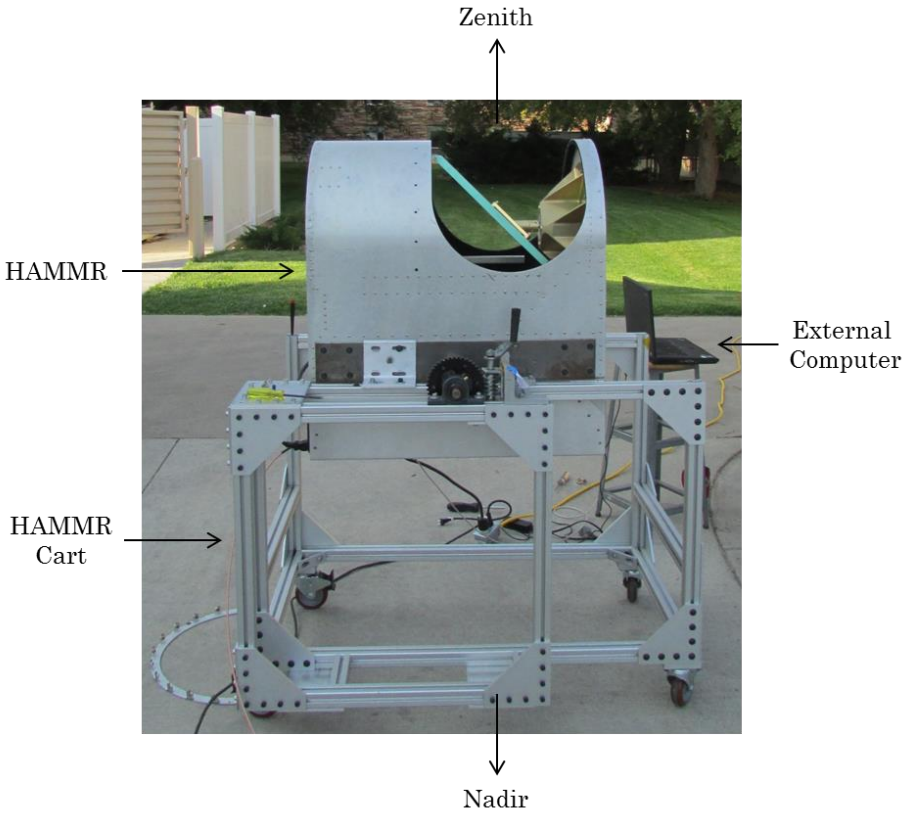

Figure 99: HAMMR Outdoor Ground Test Setup

The HAMMR instrument is mounted in a cart that was custom built by Thaddeus Johnson of the MSL. The cart holds the instrument while it is dismounted from the Twin Otter aircraft. It also has a special feature that rotates the instrument so it can view either nadir or zenith. In Figure 99, the HAMMR system has been rotated to view zenith. Once the HAMMR instrument is set up to view zenith, the system is turned on and the motor is rotated at 1 rpm as if the instrument was airborne performing cross-track scanning measurements. This type of ground based measurement and calibration is referred to as tipping curves and is visually demonstrated in Figure 100.

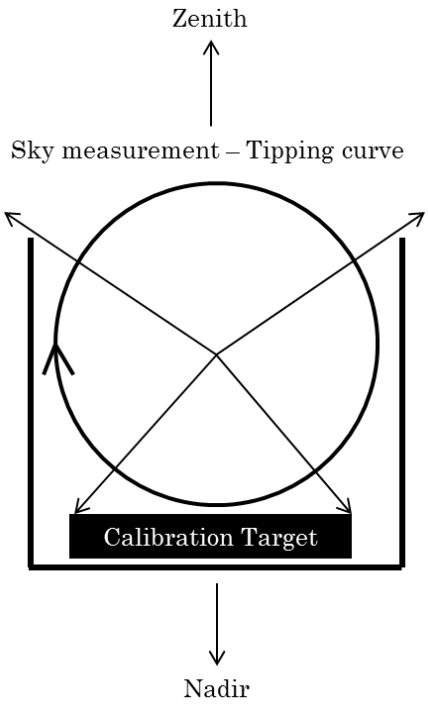

Figure 100: Front View Diagram of HAMMR During Tipping Curve Measurements

As the motor rotates, radiation from the sky, calibration target, or transitional areas in between the sky and calibration target is reflected into the radiometer antennas. The clear sky that was observed on July 3, 2014 is shown in Figure 101

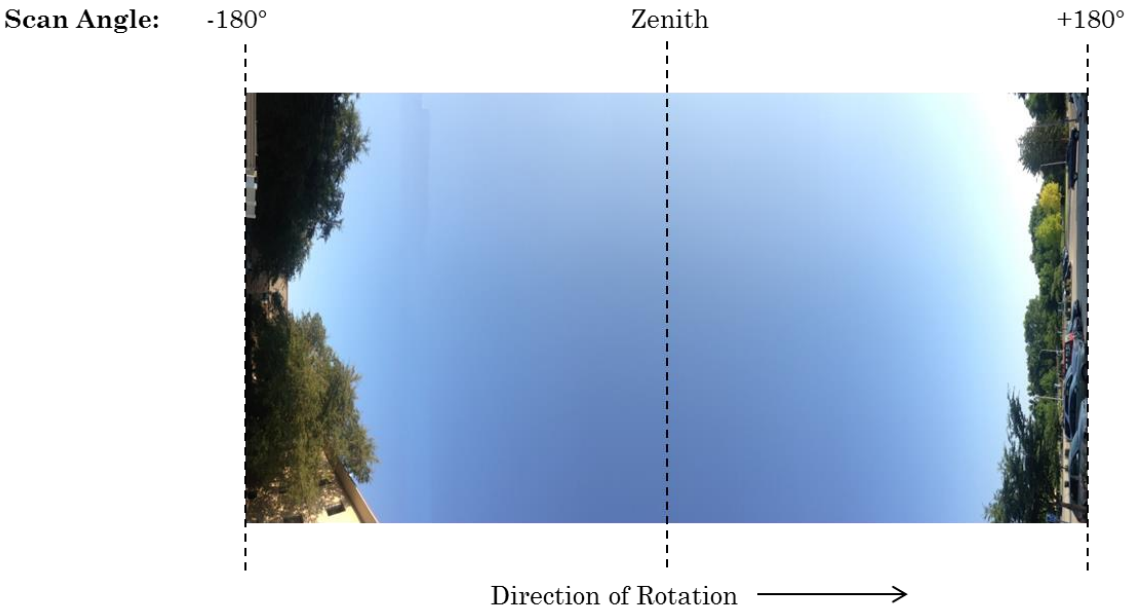

Figure 101: Sky Observed by HAMMR during Outdoor Ground Measurements

The back-end system was set up to acquire with the specifications shown in Table 14. The acquisition sequence determines when the Dicke switch is looking at the reference (REF) port or antenna (ANT) port and when the noise sources (NS) are fired. The sounding channels are super-heterodyne radiometers and, therefore, only look at ANT.

Table 14: Back-End Settings for Outdoor Ground Measurements

Radiometer	Integration Time (ms)	Acquisition Sequence
Microwave	0.2	1 ms REF 6 ms ANT 1 ms NS1 1 ms NS2 1 ms NS3

Window	0.2	1 ms REF 6 ms ANT 1 ms NS1 1 ms NS2
Sounders	1	1 ms ANT

After the measurements were completed, the radiometer output voltage data was plotted as a function of time. This data was not processed further as it was only used to verify the system was working correctly which can be determined by looking at the output voltages of the radiometers.

6.1.2 **Outdoor Ground Test Results**

The results presented here are from the final day of outdoor testing on July 3, 2014 with the setup described in the previous section. For all the results in this section, the low output voltage 'valleys' correspond to when the radiometers are viewing the sky and the high output voltage 'peaks' are measured when the radiometers are looking at the calibration target. The areas in between the peaks and valleys are the transition periods. Additionally, during the first few seconds the scanning motor is accelerating to its top angular speed of 60 Hz which is why the first few periods appear longer than the ones following it.

6.1.2.1 Microwave Channels

The microwave radiometers have six channels that produce quasi-horizontal (QH) polarized measurements at 18, 24, and 34 GHz and quasi-vertical (QV) polarized measurements at 18, 24 and 34 GHz. The results of these channels are given below.

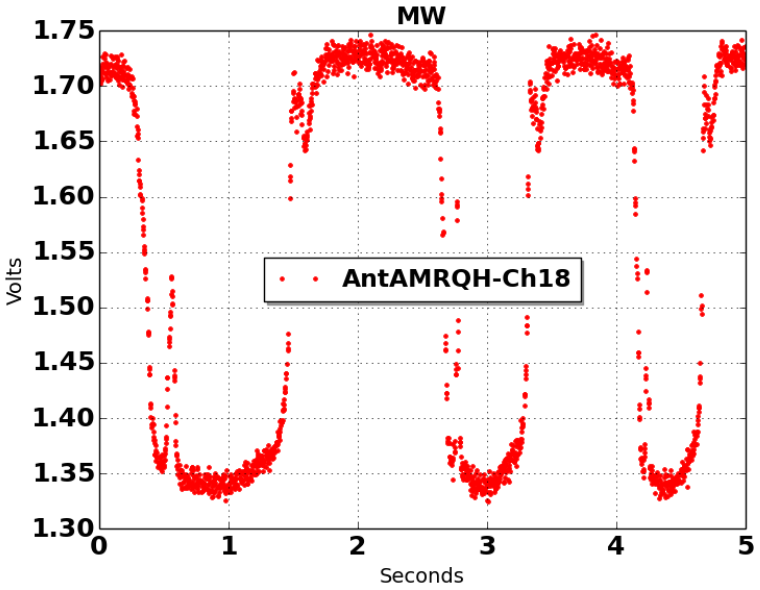

Figure 102: Outdoor Ground Test Results for Microwave QH 18 GHz Channel

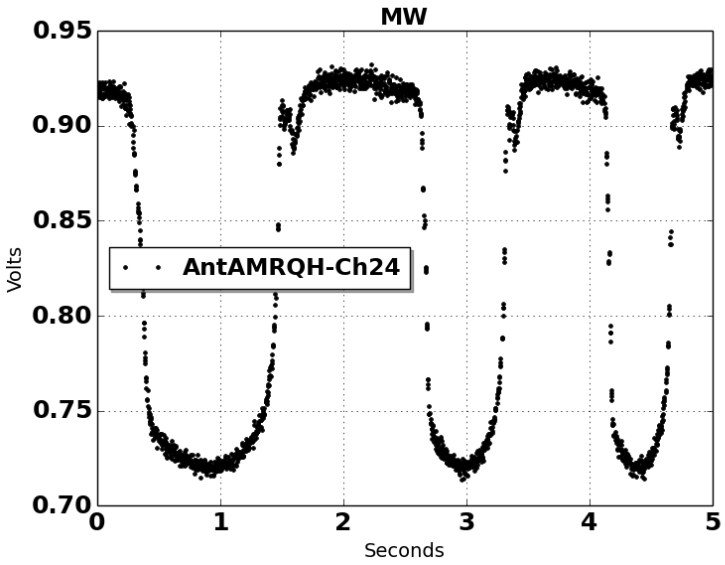

Figure 103: Outdoor Ground Test Results for Microwave QH 24 GHz Channel

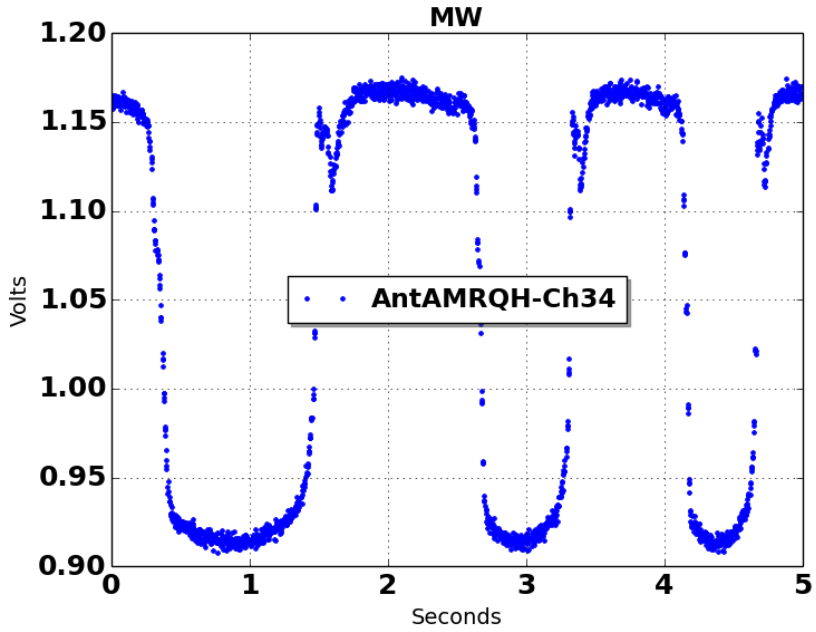

Figure 104: Outdoor Ground Test Results for Microwave QH 34 GHz Channel

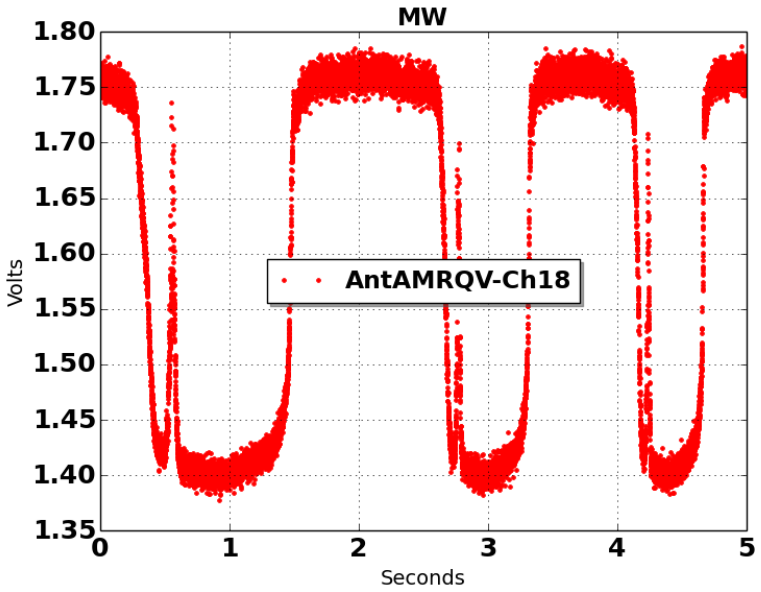

Figure 105: Outdoor Ground Test Results for Microwave QV 18 GHz Channel

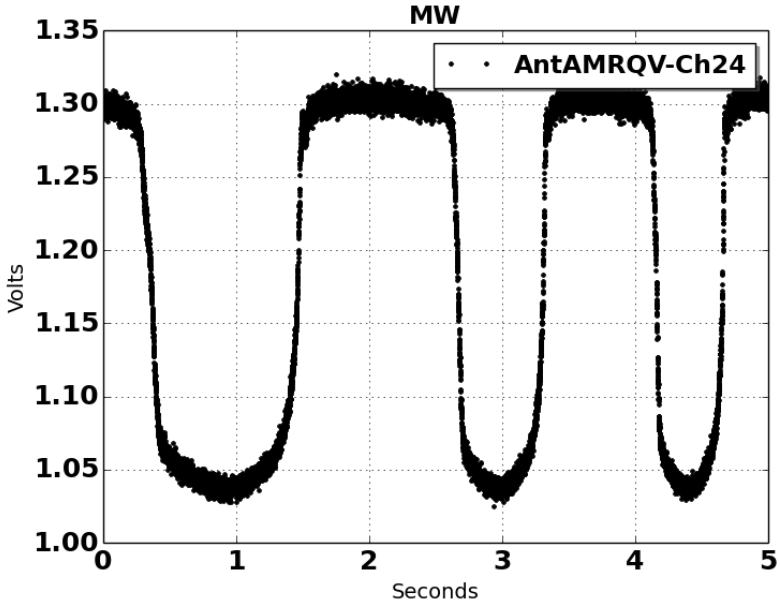

Figure 106: Outdoor Ground Test Results for Microwave QV 24 GHz Channel

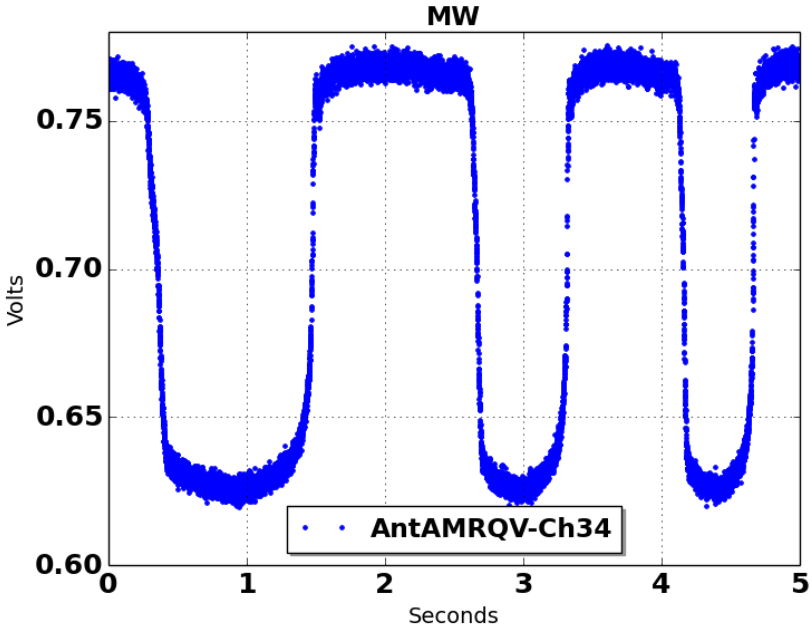

Figure 107: Outdoor Ground Test Results for Microwave QV 34 GHz Channel

These results show that the microwave channels were working properly and were ready to be tested airborne.

6.1.2.2 Millimeter-Wave Window Channels

The millimeter-wave window radiometers are made up of three channels centered at 90, 130 and 168 GHz. At the beginning of the outdoor ground tests, it was discovered that the 130 GHz diode detector was not working properly and it was sent to be repaired at JPL. Because of this, only the results of the 90 GHz and 168 GHz radiometers are given below.

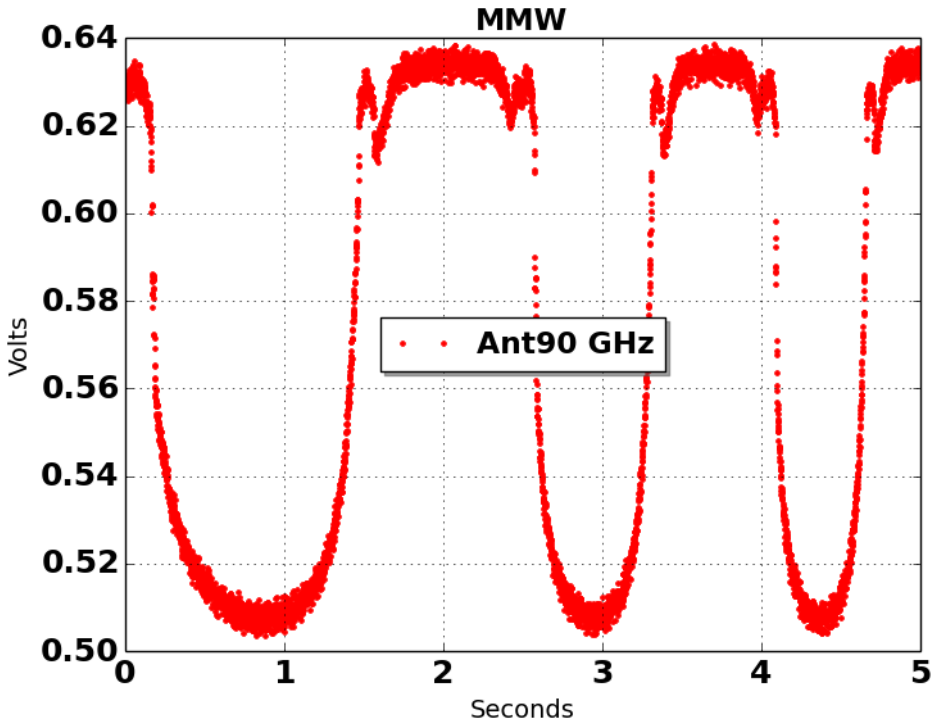

Figure 108: Outdoor Ground Test Results for Millimeter-Wave Window 90 GHz Channel

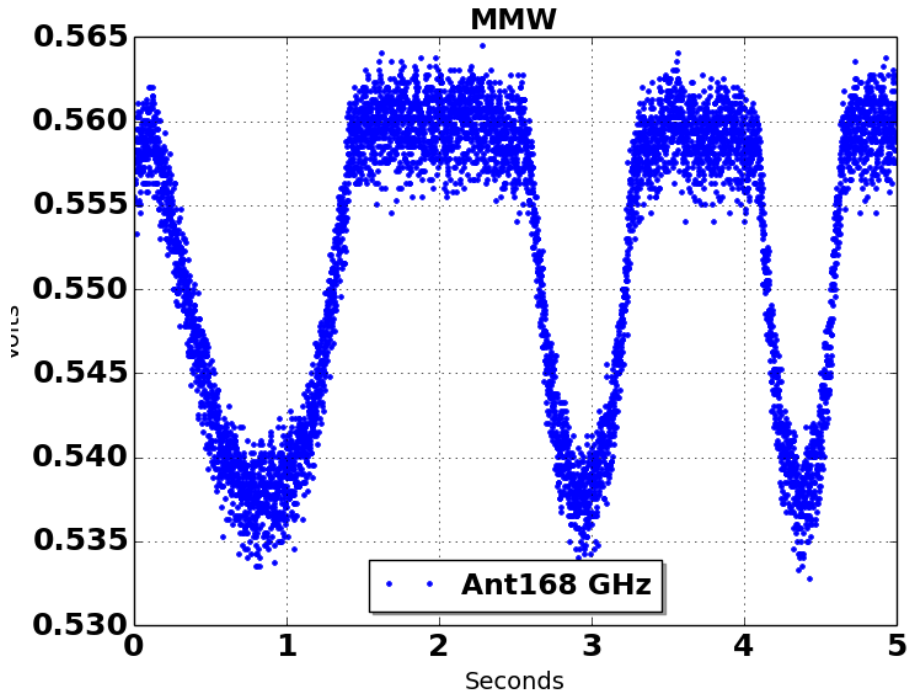

Figure 109: Outdoor Ground Test Results for Millimeter-Wave Window 168 GHz Channel

The 90 GHz and 168 GHz were found to be working properly after integration with the HAMMR system; however, the 168 GHz radiometer does show high levels of noise which is expected to reduce its radiometric resolution in the airborne tests.

6.1.2.3 Millimeter-Wave Sounding Channels

The millimeter-wave sounding radiometers have a total nineteen channels, of which, only sixteen are digitized and used for analysis. On each of the plots, the polarity sign and number following either ANT118 or ANT183 tell the offset frequency in GHz off the main frequencies of 118.75 and 183.31 GHz, respectively. Unfortunately, at the time the outdoor ground tests were carried out, multiple analog back-end boards (ABEBs) had started to malfunction; therefore, only the

results from seven 118 GHz sounding channels and six 183 GHz sounding channels are presented in this section.

Ant118+0 not available.

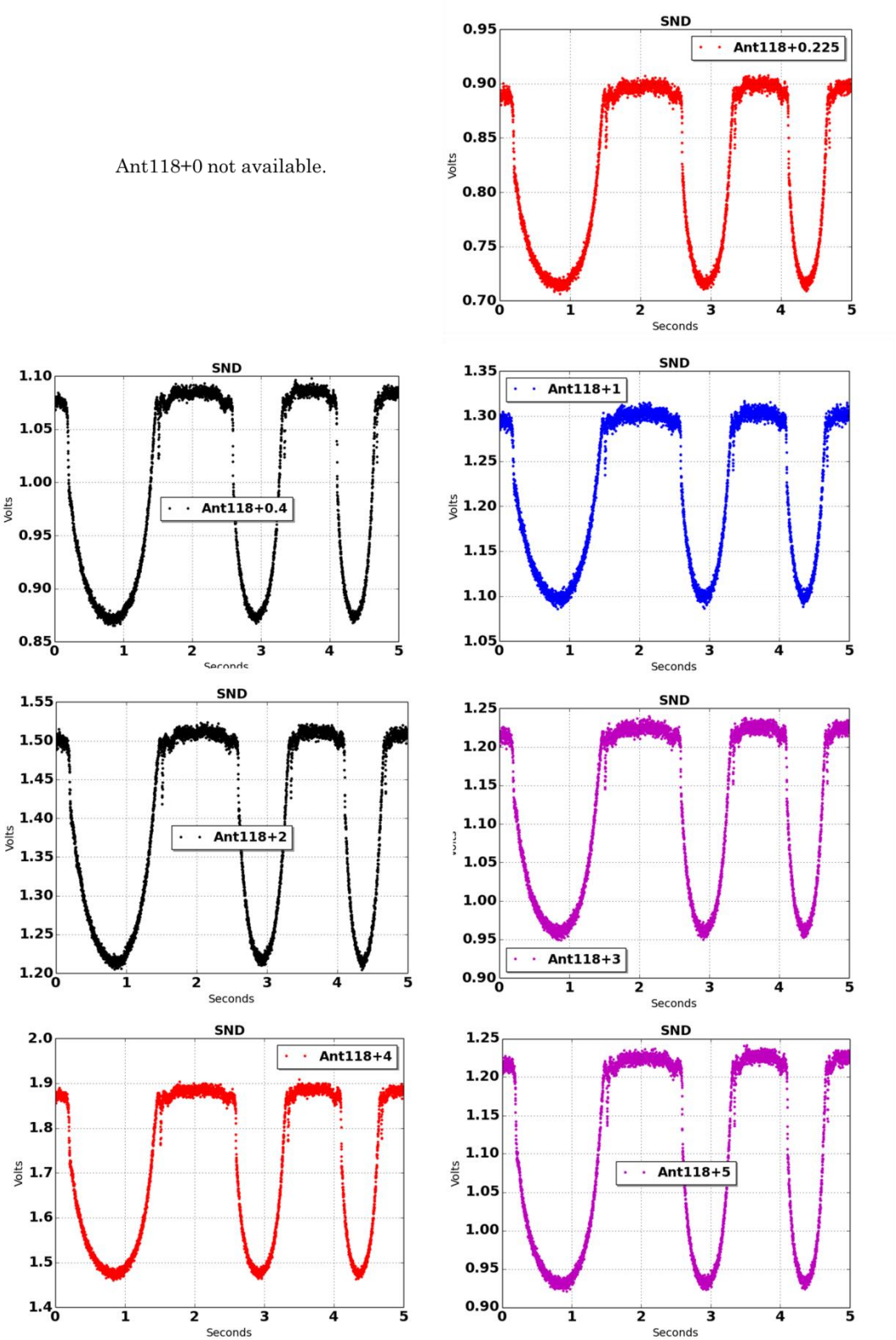

Figure 110: Outdoor Ground Test Results for Millimeter-Wave Sounding 118 GHz Channels

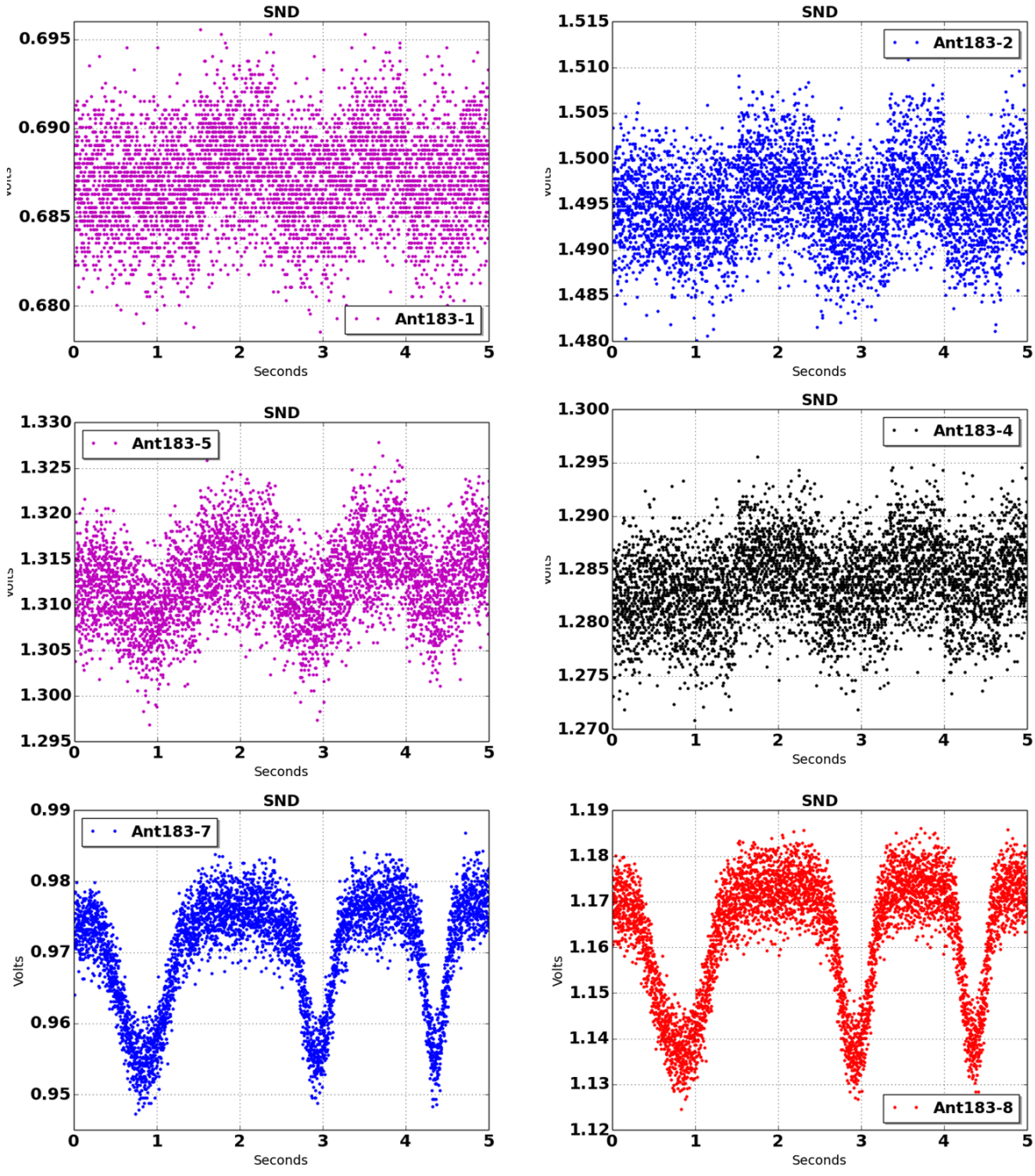

Figure 111: Outdoor Ground Test Results for Millimeter-Wave Sounding 183 GHz Channels

Unlike the other radiometers, the 183 GHz channels show dramatic differences in their responses with respect to one another. This is because as the channels get

farther from the water vapor absorption line, they become more sensitive to atmospheric water vapor which is why the -8 GHz offset channel shows the largest difference in output voltage between the sky and calibration target for the water vapor sounder.

These results show that the sounding receivers are working properly and are ready to be demonstrated airborne. The loss of some of the sounding channels was found to be a problem in the ABEBs, not the sounding receivers themselves. Part of the malfunction was found to be caused by the ABEBs saturating as they heat up. To help mitigate this problem, large heat sinks were added to the ABEB stack before the engineering flights.

6.2. Airborne Demonstration

The CSU team traveled to Twin Otter International the week of July 7, 2014 to integrate the HAMMR instrument in a Twin Otter aircraft and perform the first airborne demonstration flights. These flights are referred to as the "engineering flights" because the underlying goal of these initial flights was to ensure the HAMMR system operated correctly while in flight. One of the main concerns was that the scanning motor would malfunction due to the additional forces presented by the air flow and turbulences that would be encountered in flight. Additionally, these flights provided the first set of data acquired by the HAMMR system airborne.

6.3. Integration with the Twin Otter

The mechanics at Twin Otter built a brace around the HAMMR chassis that secured the instrument in the bottom port of the aircraft. Once the brace was completed and attached to the instrument, the CSU team assisted in mounting HAMMR into the aircraft as in Figure 112.

Figure 112: CSU Team Guiding HAMMR into the Port on the Twin Otter Aircraft

Once HAMMR was secured in the Twin Otter, the mechanics designed three custom fairings for the instrument. The two fairings on the front and back of the instrument were made to make the instrument more aerodynamic as the HAMMR

chassis has flat faces. The third fairing was designed to divert air away from the aperture of the instrument. This has two benefits: it reduces the risk of the motor malfunctioning due to wind forces and it minimizes air circulation around the radiometers which could affect their performance. The third fairing was installed near the aperture of the instrument and the interior portion of the fairing was painted matte black. The HAMMR instrument mounted in the Twin Otter with the three fairings is shown in Figure 113.

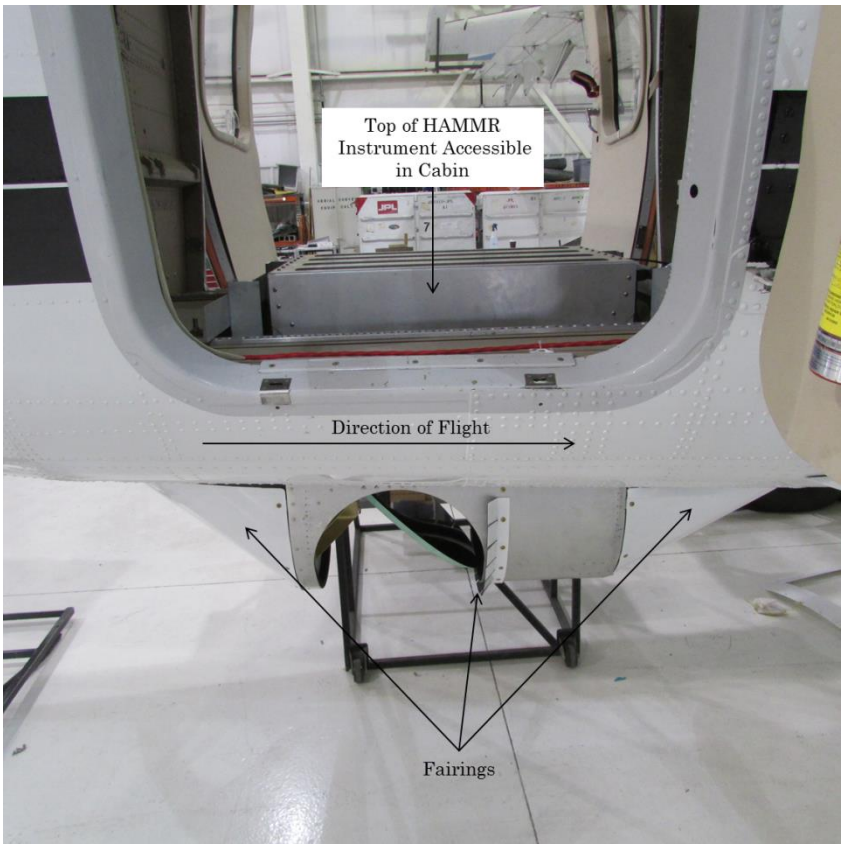

Figure 113: HAMMR in Twin Otter with Fairings

The top of the instrument was accessible to the CSU team while in the Twin Otter cabin. This feature gave the team access to the power switch and Ethernet port on the front face of the instrument. The HAMMR lid could also be removed if debugging or modifications were needed to be made after the instrument was installed. A top view of the HAMMR instrument in the Twin Otter is shown in Figure 114.

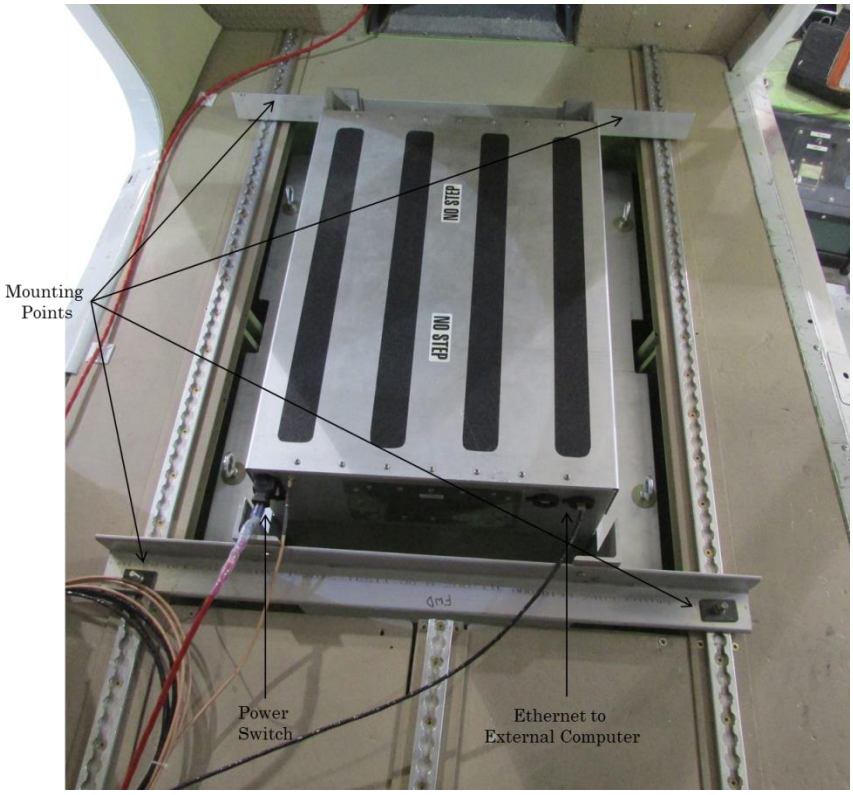

Figure 114: Top of HAMMR Mounted in Twin Otter

Inside the cabin, the Twin Otter team mounted a desk for use while in flight. The desk had another power switch for the HAMMR instrument which was easily accessible while sitting at the desk. This was added as a safety feature in case of an

emergency where the HAMMR instrument would need to powered down immediately. The final configuration of the Twin Otter aircraft and HAMMR instrument is shown in Figure 115 as the aircraft was being prepared for take-off.

Figure 115: Twin Otter and HAMMR Being Prepared for Take Off

Once the integration of the HAMMR instrument with the Twin Otter was completed, the aircraft was prepared for its initial flights.

6.4. Blue Mesa Reservoir, Colorado

The first flight of the HAMMR instrument was performed on July 9, 2014. The purpose of this initial flight was to verify functionality of the complete system and ensure the motor was able to rotate properly in flight before taking measurements over Lake Powell in Utah.

6.4.1 **Blue Mesa Reservoir Flight Plan**

Blue Mesa Reservoir was chosen as the first measurement site because it is the largest body of water in Colorado and is in close proximity to Grand Junction, Colorado where Twin Otter International is located [60]. The plan for the first flight was to circle around the Grand Junction Regional Airport and run a serious of tests on the motor to see how it was behaving in flight. If the motor malfunctioned, the Twin Otter would return to the hangar for the CSU team to debug the motor. If the motor was determined to be working properly, then the Twin Otter would fly to Blue Mesa Reservoir and follow the flight plan shown in Figure 116.

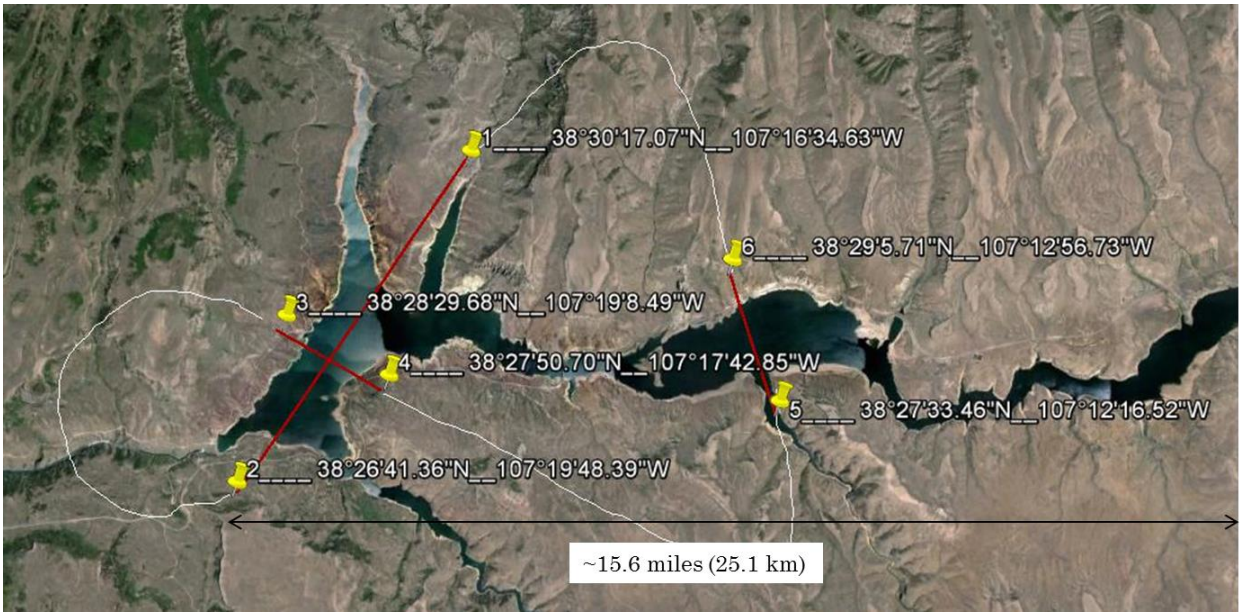

Figure 116: Blue Mesa Reservoir Flight Plan

The three red lines in Figure 116 show the critical flight paths that the CSU team requested to be flown over Blue Mesa Reservoir. Measurements taken on these paths are expected to show clear transitions between the water surface and land.

The paths are also positioned in areas of the reservoir that are very wide so the ground swath of the HAMMR should not see any emissions from land while over the reservoir. These critical flight paths are to be flown several times so the repeatability of the measurements can be determined.

For these measurements, the Twin Otter will be flown at 10,000 feet (~ 3 km) above mean sea level (AMSL). It is ideal to for the aircraft to fly at slow speeds less than 90 knots (103 mph); however, it is more important for the aircraft to maintain constant yaw, pitch, and roll to within ±10°. The pilots were therefore requested to fly at the slowest speed possible while maintaining the requirements for yaw, pitch, and roll which were recorded by the GPS/IMU.

6.4.2 **Motor Position Error Test**

The first HAMMR system check that was performed in an aircraft was to verify if the motor was rotating properly while in flight. For this test, the motor was controlled and monitored using QuickSilver's programming software QuickControl [61]. The motor encoder stores information about the motor operation in registers that can be accessed through QuickControl. The register that was monitored for this test was the Current Position Error register. The encoder determines the position of the motor by discretizing the 360° rotation into 16,000 counts (1 count = 0.0225°). As a command is sent to the motor, the encoder tracks the position the motor should be in and what position the motor is actually in. The instantaneous difference

between these two values is referred to as the current position error and is given in counts out of 16,000.

During tests in the lab, the motor had an average current position error of 10 counts or 0.225°. The goal of the average motor position error in flight was set to be less than 50 counts or 1.125°. To test the current motor position error, three commands were sent to the motor over a five minute time period: hold at zenith-viewing position, rotate at 60 Hz, and hold at zenith-viewing position. The current position error register was logged into a data file for the duration of this test and the results are plotted in Figure 117.

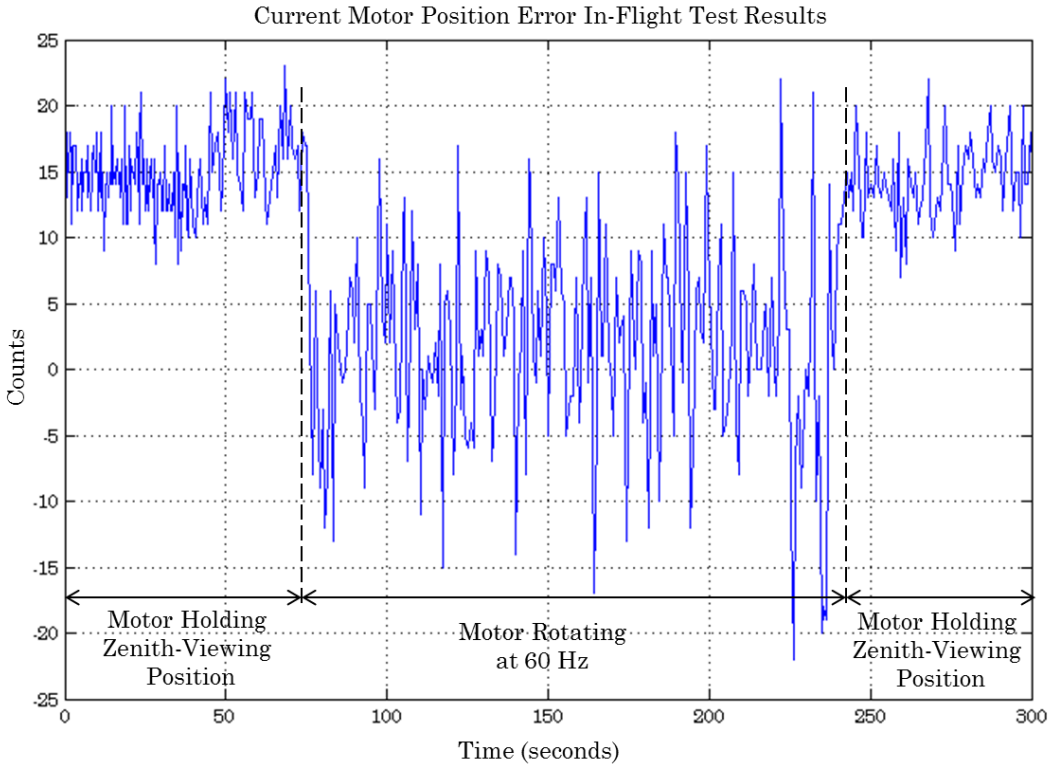

Figure 117: Current Motor Position Error In-Flight Test Results

The time periods when the motor was executing the three different commands can be easily seen in Figure 117. From a first glance, it is observed that the motor position error stayed well below 50 counts during the tests and the position error count actually decreased as the motor rotated. The average current motor position error while the motor was holding in zenith-viewing position is 14.8 (~0.3°) and the average current motor position while the motor is rotating at 1 rpm is 9.1 counts (~0.2°). These results confirmed that the motor had excellent performance in flight and was robust against additional forces introduced during flight. With the conclusion of this test, the flight to Blue Mesa was carried on.

6.4.3 **Initial Calibration Target for Blue Mesa Reservoir Flight**

The purpose of the Blue Mesa Reservoir flight was to ensure total system functionality of the HAMMR instrument while in flight and to also practice calibrating the instrument while it is mounted in the aircraft. The HAMMR needs to be calibrated right before take-off and as soon as possible after landing since the performance of the system can change over time due to temperature fluctuations.

As discussed several times in this thesis, a two point calibration is used with a "cold" load and a "hot" load. To accomplish this, a calibration target was made on the first day at Twin Otter using Eccosorb HR-10 [17], a Styrofoam cooler with outer dimensions of 25.25" x 16" x 12.63" (64.1 x 40.6 x 32.1 cm), foil, and liquid nitrogen (LN_2). The bottom of the cooler was lined with foil and the Eccosorb was

place on top of the foil and secured to the bottom of the cooler. The Eccosorb was kept at ambient temperature for the "hot" load and then LN_2 was poured in the cooler for the "cold" load. The assembled calibration target is shown in Figure 118 as a hot load and cold load.

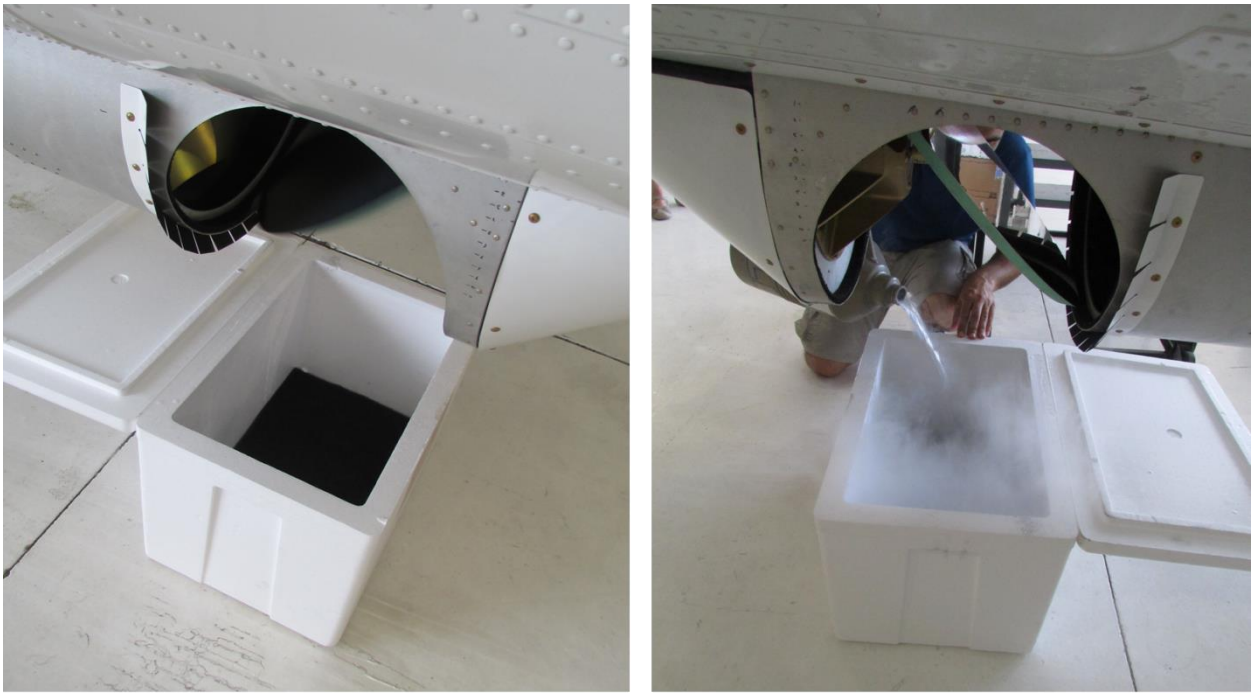

a) b)

Figure 118: a) Initial Version of Hot Calibration Target and b) Initial Version of Cold Calibration Target with LN_2

This first version of the Twin Otter calibration target needed improvements. The entire interior of the cooler should have been lined with foil and "wings" should have been added to cover the entire swath. The first day at Twin Otter posed very strict time constraints and the supplies were not available to improve the calibration target before the first flight. Although the calibration target was not

complete for the Blue Mesa flight, it was able to be corrected before the Lake Powell flights.

6.4.4 **Summary of Blue Mesa Reservoir Flight**

The first day of flights at Blue Mesa Reservoir validated total system functionality of the HAMMR in flight and proper operation of the motor. The measurements taken over the Blue Mesa Reservoir were examined for each radiometer to confirm they were operating as desired. All six channels in the microwave radiometers and all three mm-wave window channels were found to be fully operational. Fifteen out of sixteen sounding channels were working and the one channel that was not operational was due to a broken ABEB, not the radiometer itself. All of the other subsystems, such as the GPS IMU and thermistors, were also confirmed to be operating correctly. In addition verifying the HAMMR system functioned correctly in flight, the calibration target built for the first flight was able to be improved for the flights over Lake Powell.

6.5. Lake Powell, Utah

The goal of the flights over Lake Powell were to take a number of hours of measurements to be used for analyzing the airborne performance of the radiometers over an inland body of water. Lake Powell was specifically chosen for these flights as it is only a 2 hour round-trip flight time from Grand Junction, Colorado and it is

the second-largest artificial reservoir in the United States [62]. The HAMMR measurements over Lake Powell in Utah took place on July 10 and 11, 2014.

6.5.1 **Lake Powell Flight Plan**

Similar to the Blue Mesa Reservoir flight plan, the pilots were instructed to fly as slowly as possible while maintaining constant yaw, pitch, and roll to within ±10°. The Twin Otter was flown at 10,000 feet (~3 km) AMSL over the critical paths shown as colored lines in Figure 119.

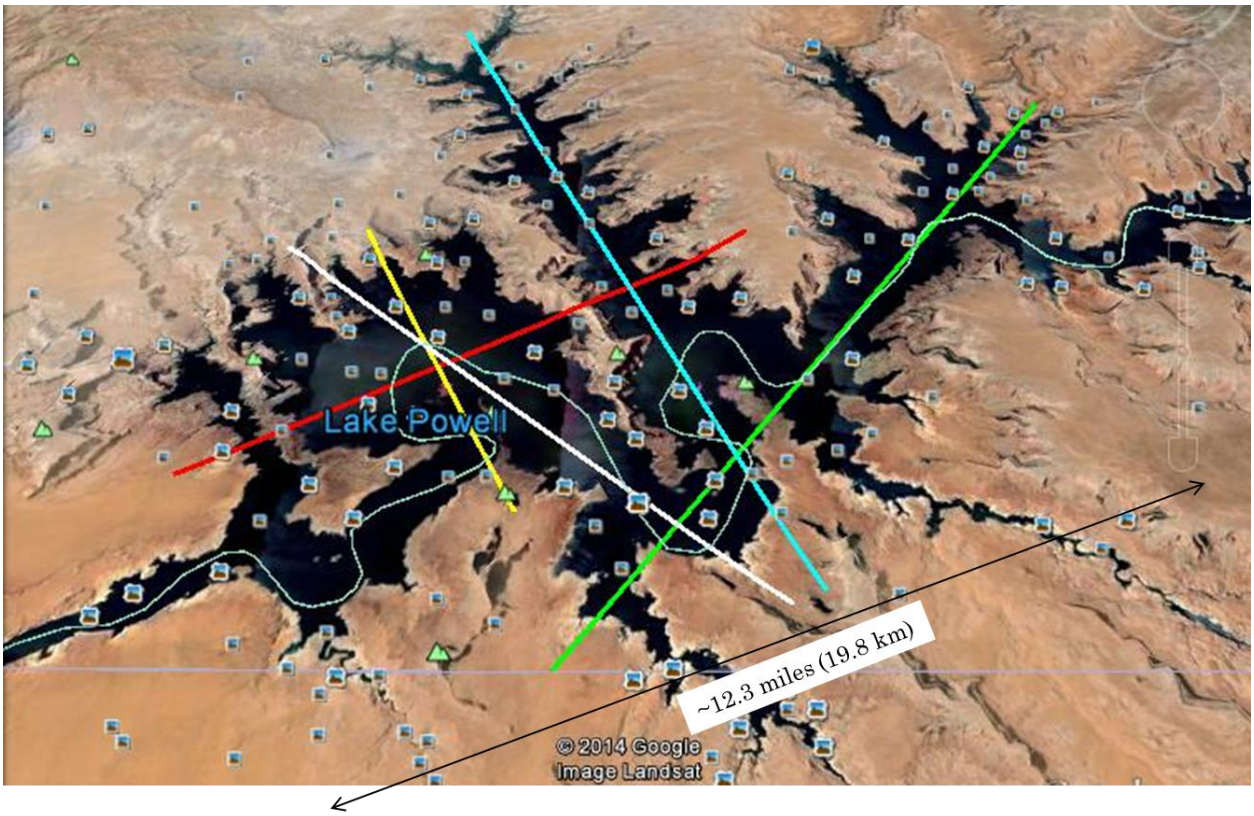

Figure 119: Lake Powell Flight Plan with Critical Paths Highlighted in Colors

These five critical flight paths were repeated four times on each of the two days.

6.5.2 **Calibration Target for Lake Powell Flights**

Before the flights to Lake Powell, the calibration target was improved by completely covering the interior with foil and adding "wings". The "wings" are also lined with foil and positioned to completely cover the HAMMR swath. In addition to the new wings and foil-lined interior, the calibration target was also lifted to be closer to the HAMMR aperture during calibration. The improved calibration target is shown in Figure 120 as it was being used to calibrate the HAMMR system before the first flight to Lake Powell.

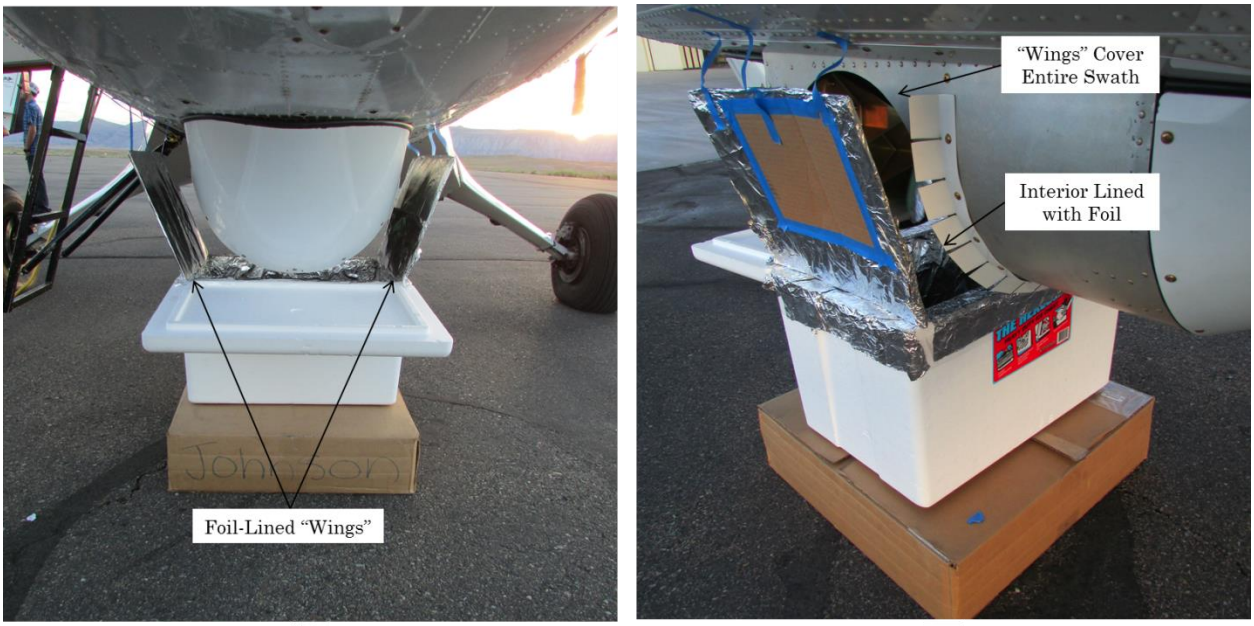

Figure 120: a) Front View of Improved Calibration Target and b) Side View of Improved Calibration Target

For the engineering flights, the "wings" were made out of cardboard as that was what was readily available at the time. A sturdier calibration target using metal

wings will be made for the validation flights over the coast of Southern California. As in the Blue Mesa reservoir calibration, the Eccosorb material was kept at ambient temperature for the "hot" load and LN_2 was poured in the cooler for the "cold" load in the two point calibration. The results of the two-point calibration carried out before the first Lake Powell flight on July 10, 2014 will be added after the results are processed.

6.6. Preliminary Results

The results presented in this section are from the HAMMR taken on July 10, 2014 over Lake Powell following the green critical path in Figure 119. At the time this thesis was completed the field data had not been calibrated to be shown in terms of brightness temperature; therefore, the measurements are analyzed here in terms of output voltage normalized with respect to the calibration target voltage. A Google Earth image of the measured scene of the HAMMR instrument is in Figure 121.

Figure 121: Google Earth of the Scene Measured by the HAMMR Instrument

The yaw, pitch and roll measured by the GPS/IMU for this set of engineering flight data is shown in Figure 122.

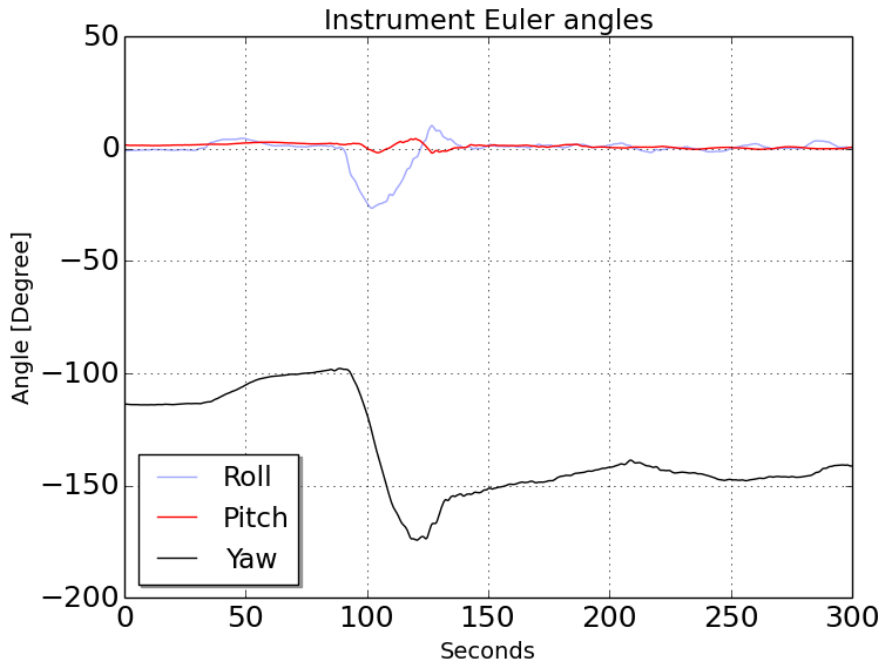

Figure 122: Yaw, Pitch and Roll of HAMMR for Flight Data

The GPS/IMU data shows that the Twin Otter turned approximately two minutes into the acquisition. This turn caused the HAMMR instrument to measure the sky momentarily and this can be seen in the results of most of the channels.

6.6.1 Microwave Channels

The results for both polarizations of the microwave channels are given below.

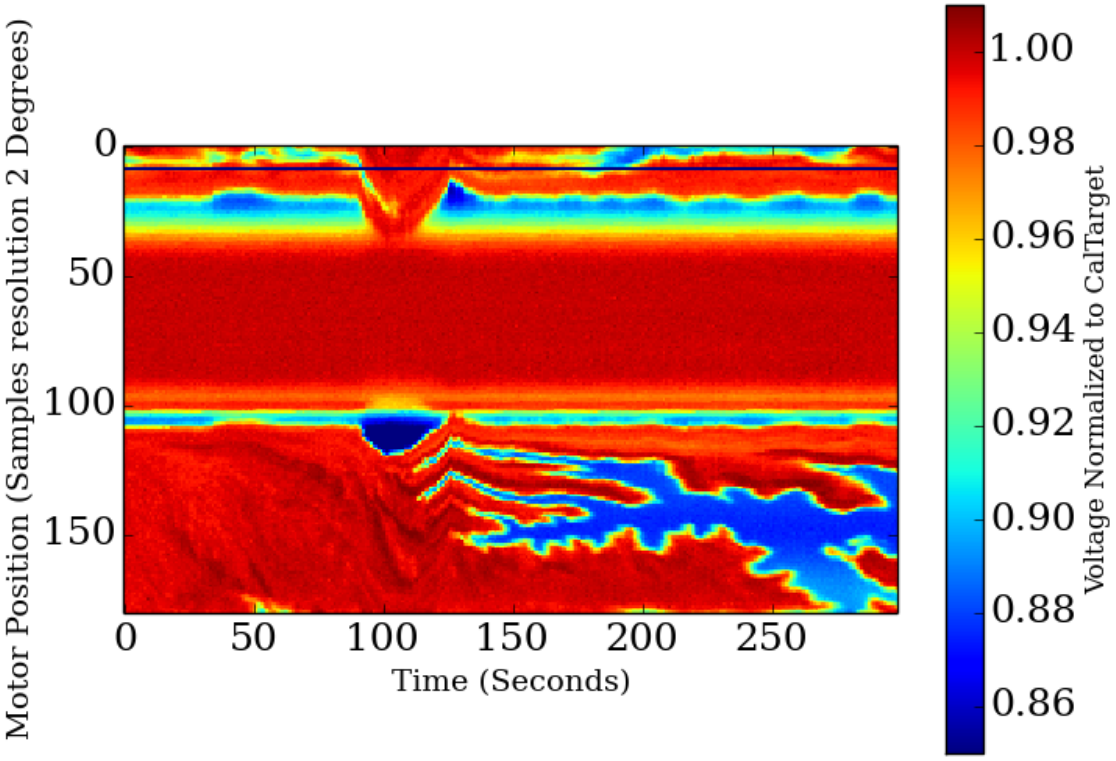

Figure 123: QH 18.7 GHz Microwave Radiometer Normalized Voltage

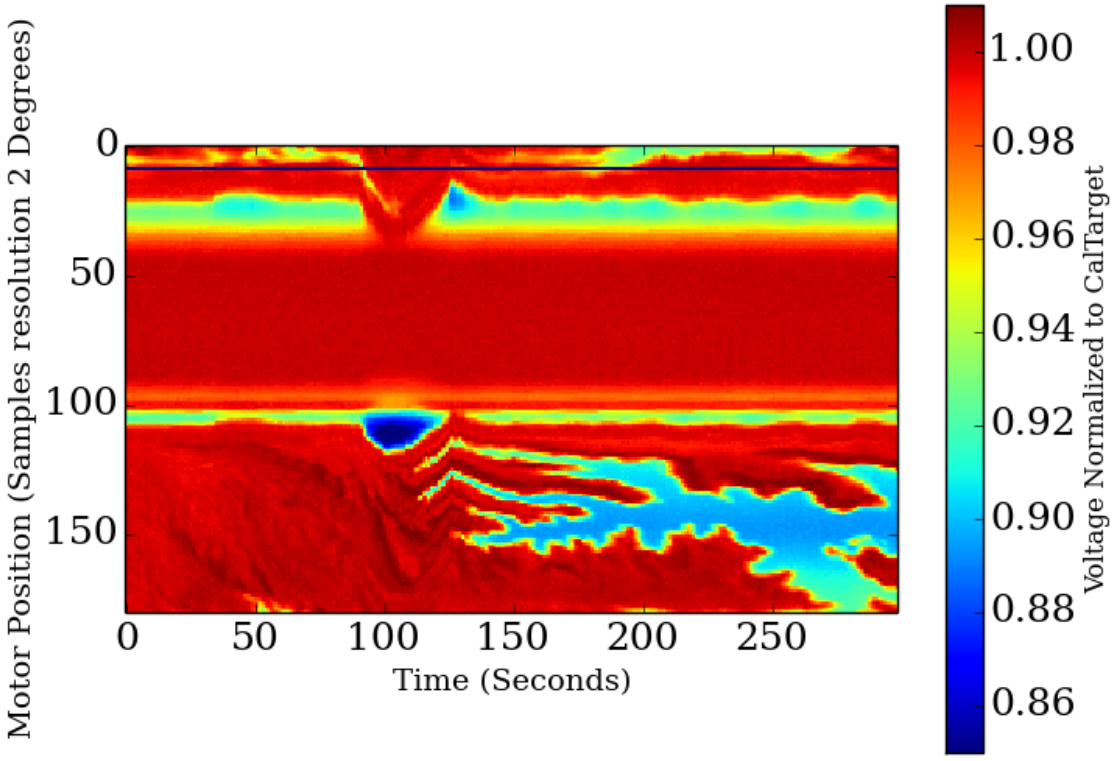

Figure 124: QH 23.8 GHz Microwave Radiometer Normalized Voltage

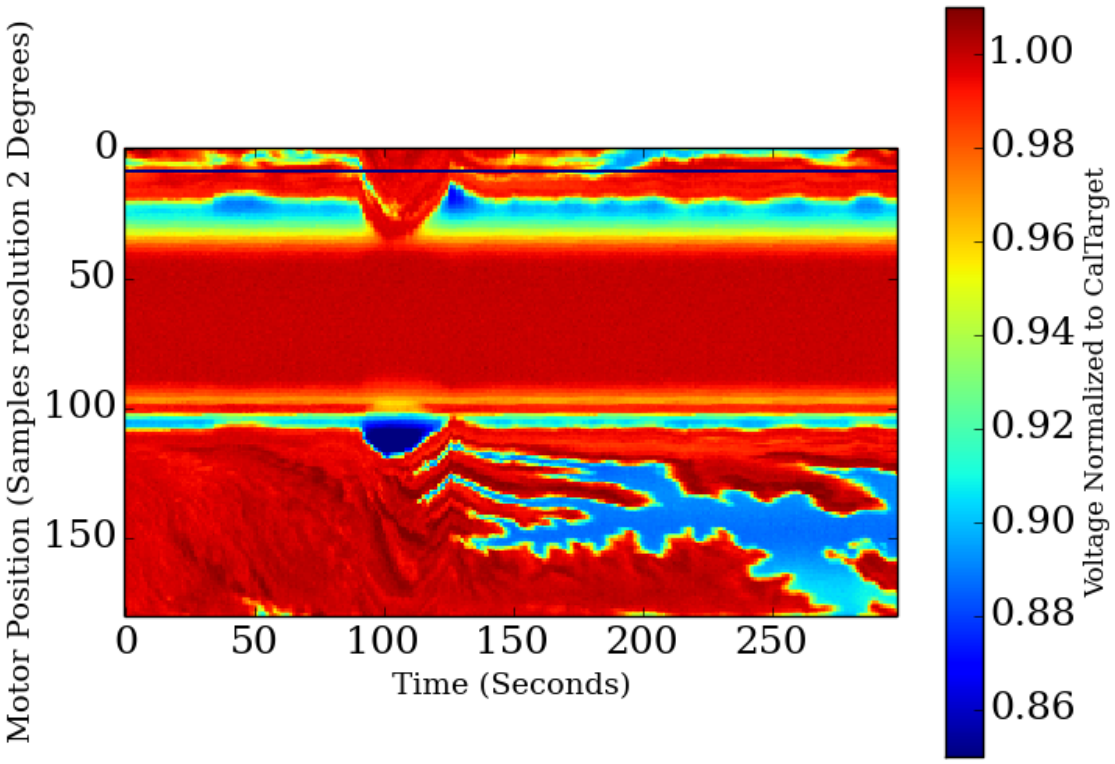

Figure 125: QH 34 GHz Microwave Radiometer Normalized Voltage

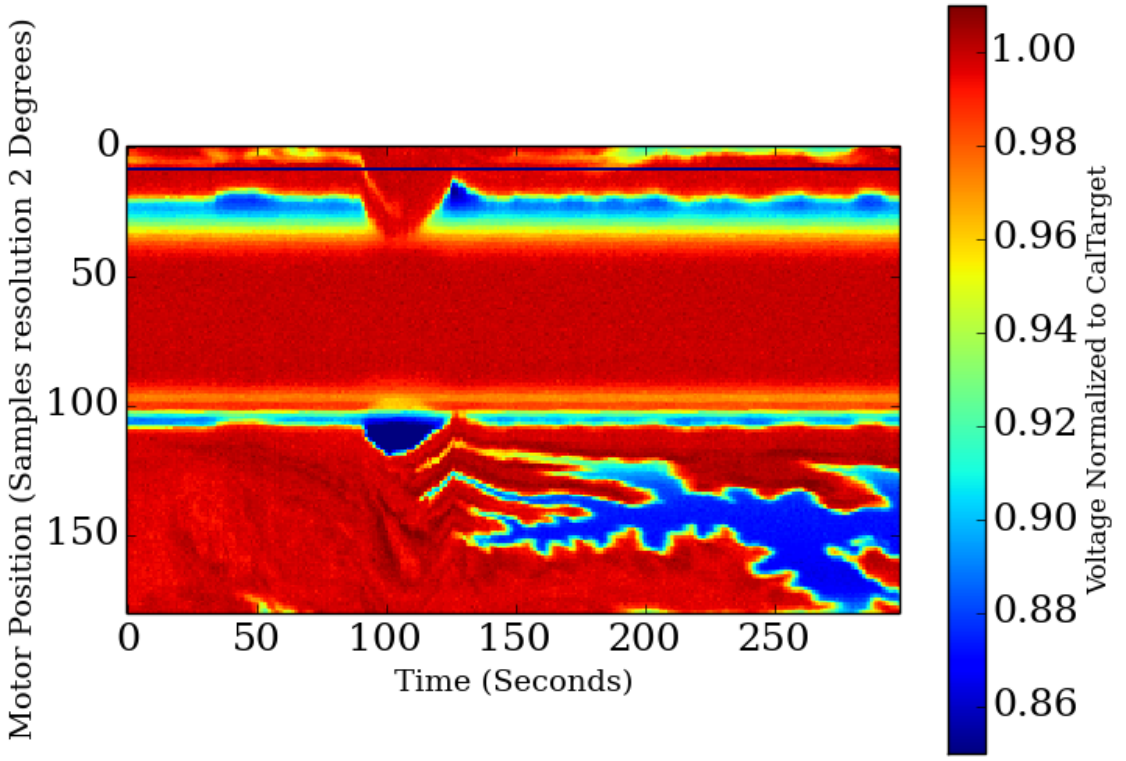

Figure 126: QV 18.7 GHz Microwave Radiometer Normalized Voltage

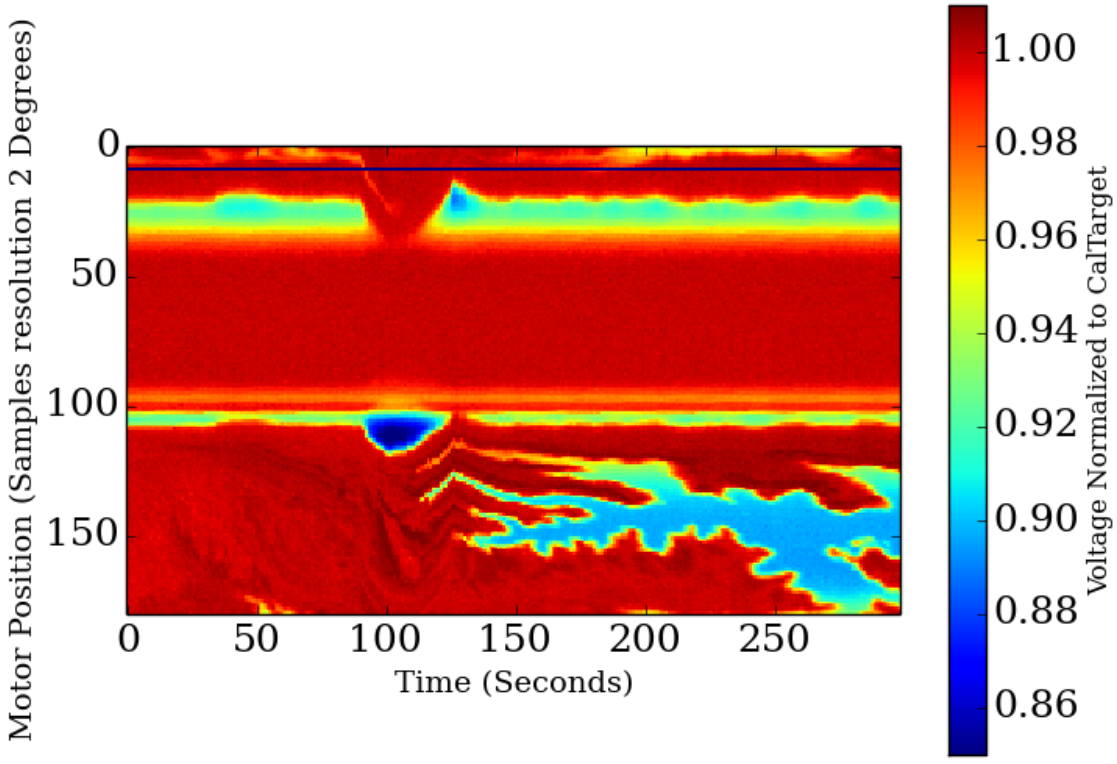

Figure 127: QH 23.8 GHz Microwave Radiometer Normalized Voltage

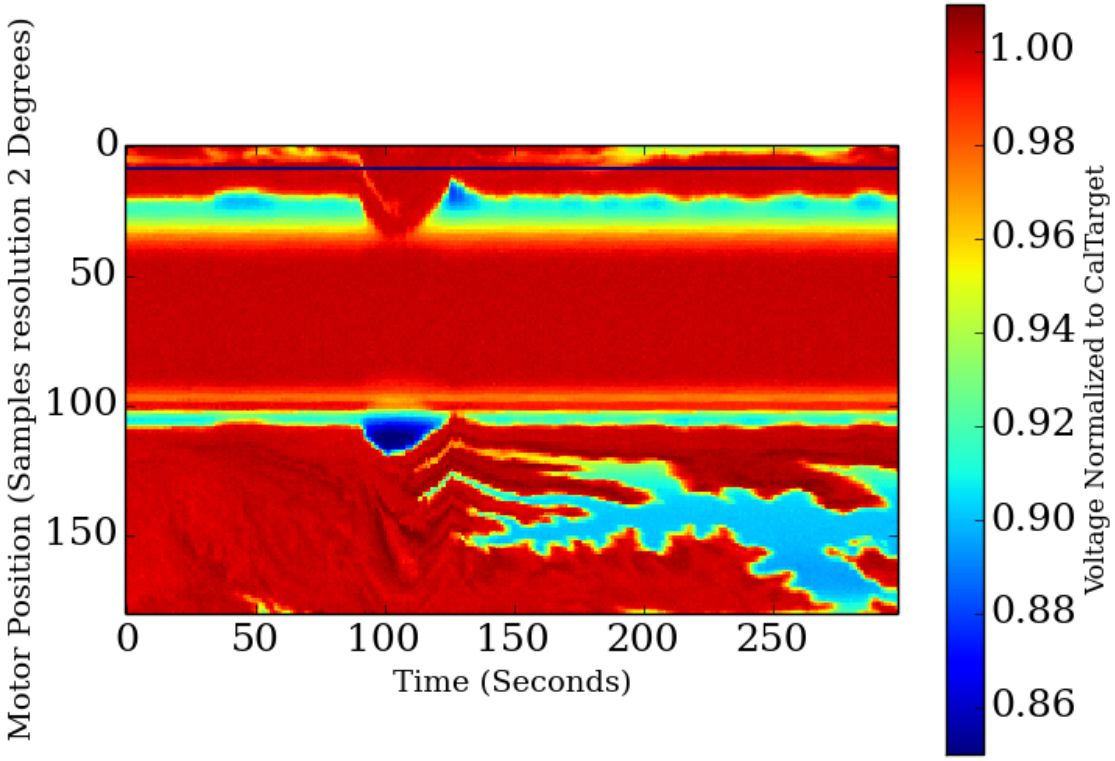

Figure 128: QH 34 GHz Microwave Radiometer Normalized Voltage

The results of all six channels on the microwave radiometers show that the microwave radiometer is sensitive to changes in brightness temperature of the measured scene. The features of Google Earth image in Figure 121 can be distinctly seen in all of the microwave channel measurements. As the aircraft turned around 90 seconds the sky was seen in all three microwave channels. The image becomes slightly distorted as the motor position scan angle deviates from nadir; however, this is expected and the footprint of the radiometers changes with scan angle.

6.6.2 Millimeter-Wave Sounding Channels

The results for all sixteen channels of the two sounding channels are given below.

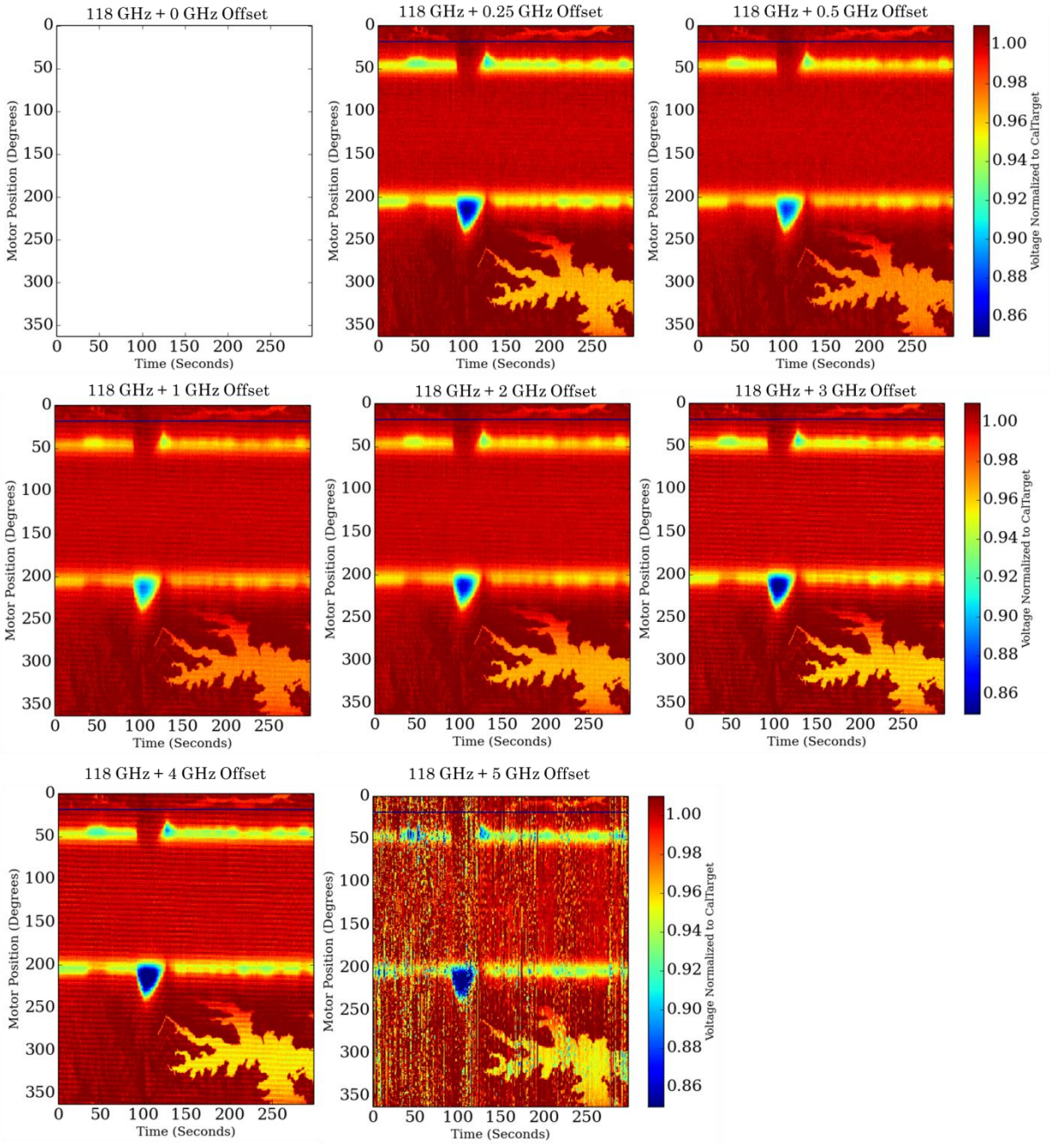

Figure 129: Temperature Sounding Results

The temperature sounding channels were sensitive to the changes in brightness temperature of the measured scene and the coastline of Lake Powell can be seen in the data. There is no data for the 0 GHz offset channel because the ABEB was malfunctioning at the time of the engineering flights.

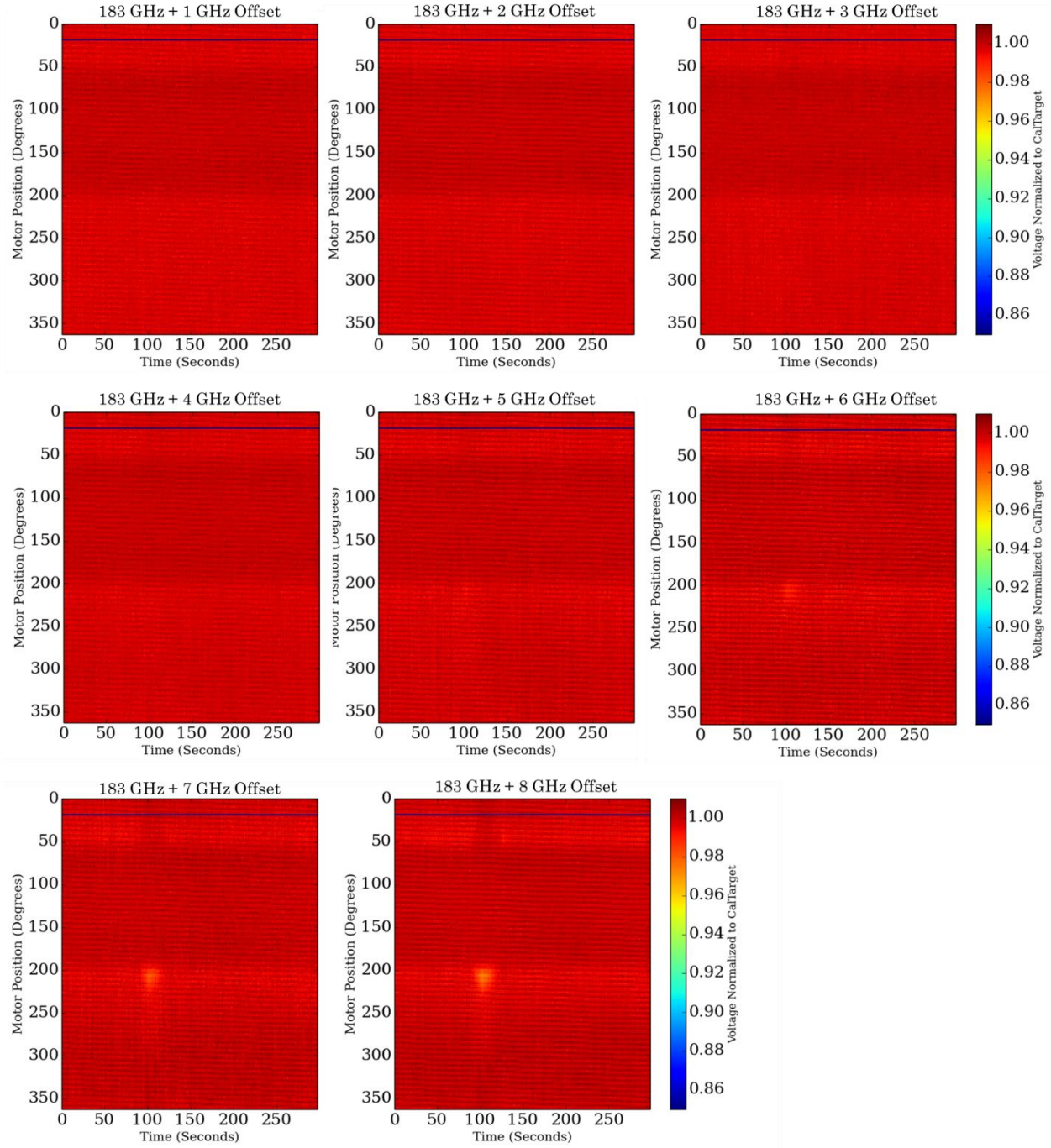

Figure 130: Water Vapor Sounding Channel Results

The water vapor sounding channels were almost completely saturated which is expected due to the high absorption of water vapor around 183.31 GHz. The higher

offset channels, specifically the +6, +7, and +8 GHz offset channels were able to measure the sky as the aircraft turned around 100 GHz.

6.6.3 Millimeter-Wave Window Channels

The results for the millimeter-wave window channels are given below.

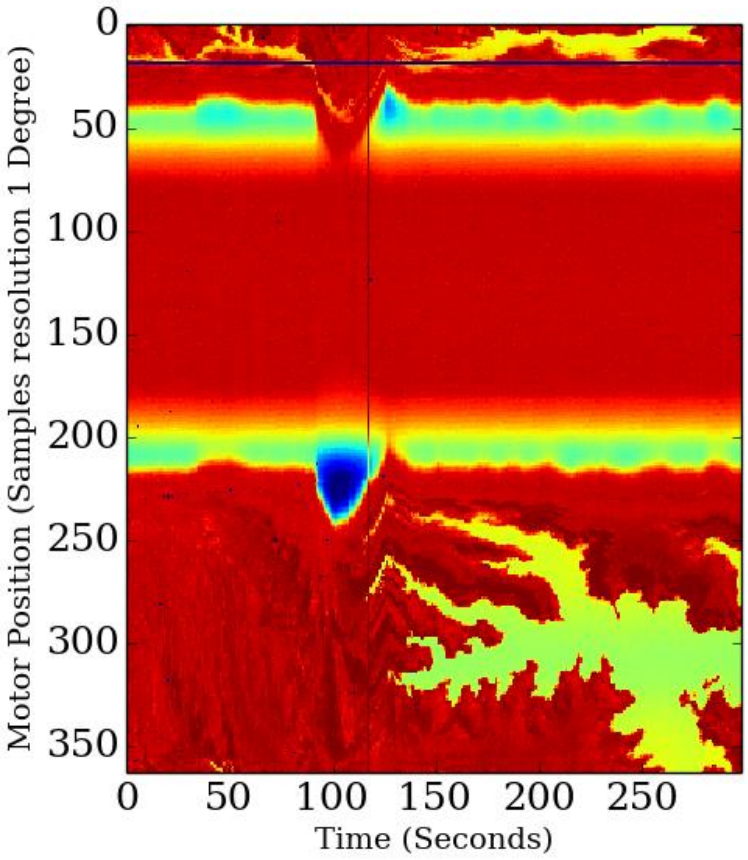

Figure 131: 90 GHz Window Channel Results

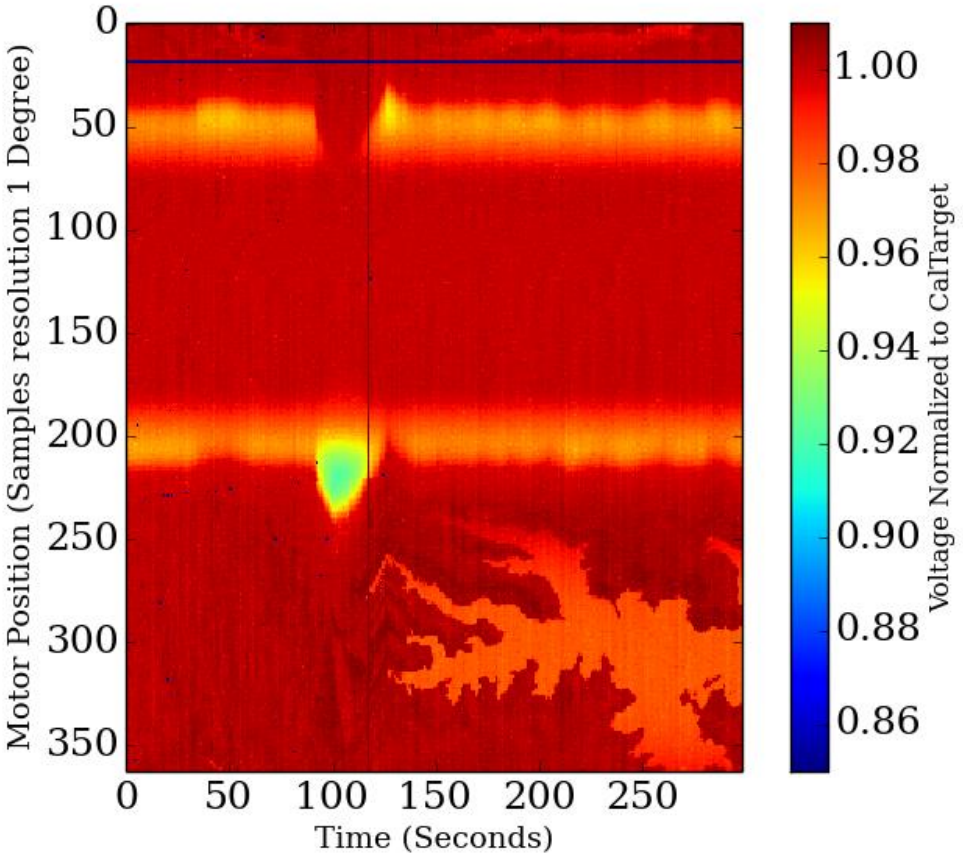

Figure 132: 130 GHz Window Channel Results

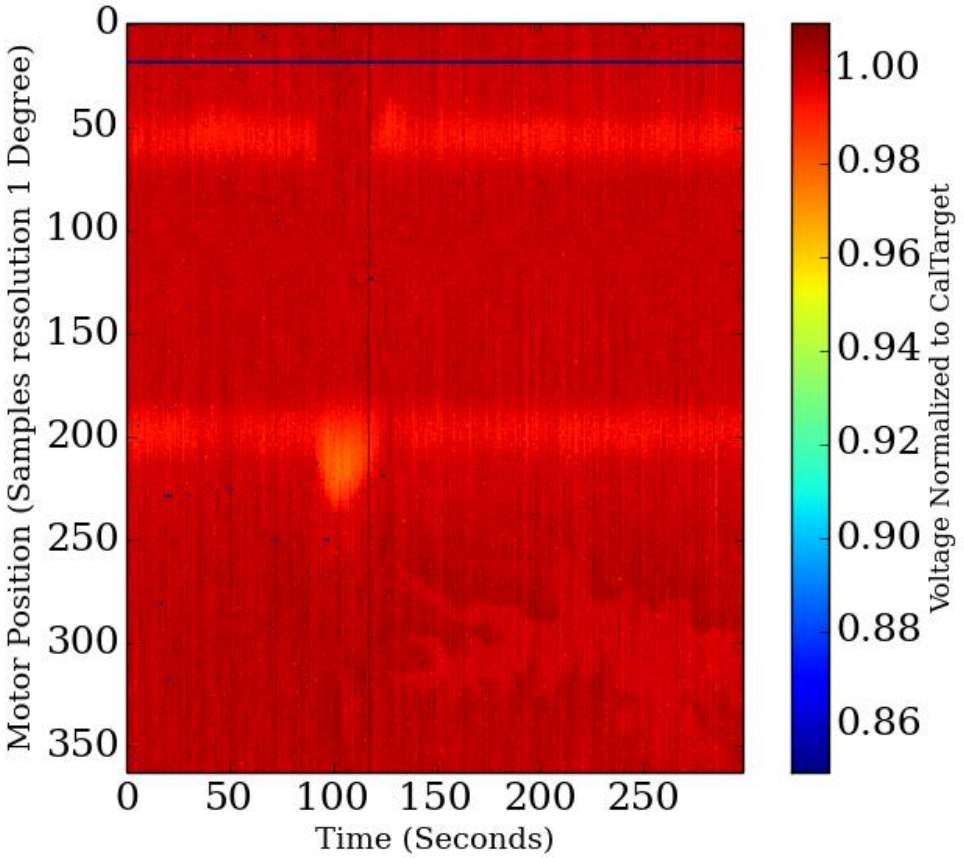

Figure 133: 168 GHz Window Channel Results

The 90 GHz and 130 GHz window channels showed excellent sensitivity to measured brightness temperature in their first airborne demonstration. The 168 GHz channel retrieved data is significantly noisier than the 90 and 130 GHz channels and is also less sensitive. This is because the 168 GHz receiver has the highest receiver noise of the three window channels and also lies close to the 183.31 GHz water vapor absorption line.

6.6.4 Microwave and Millimeter-Wave Window Channel Comparison

The purpose of the development of the high-frequency millimeter-wave window radiometers was to demonstrate the technology which can be used to improve the spatial resolution of measured wet-tropospheric path delay. Although the field data has not been calibrated to be presented in brightness temperature, the normalized voltages of the two receivers can be compared to see if the spatial resolution has improved. To this extent, the measurements of the low-frequency microwave channels and high-frequency millimeter-wave window channels are compared below.

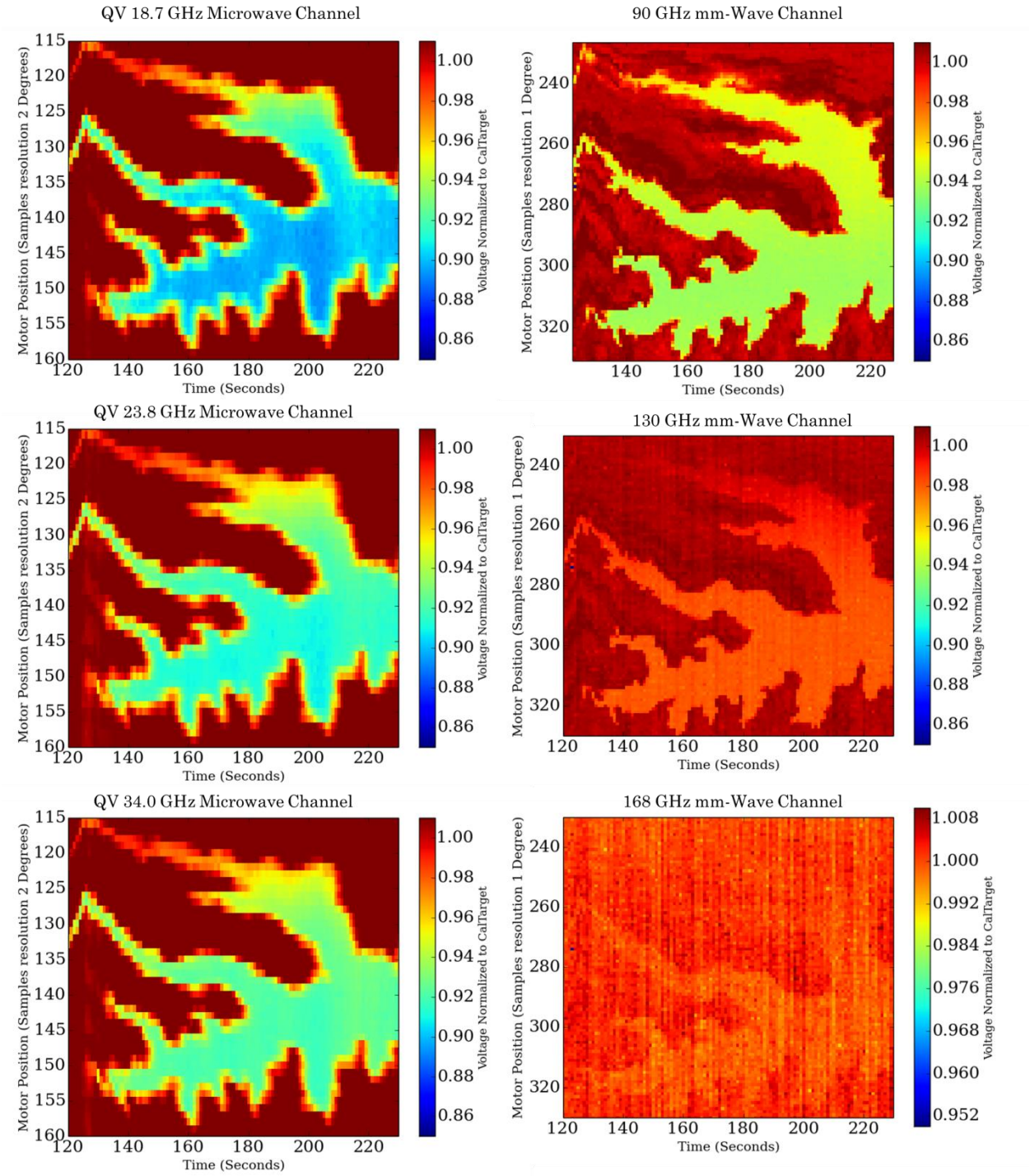

Figure 134: Comparison of Low-Frequency and High-Frequency Radiometer Measurements

Although these are just preliminary results, the side-by-side comparison the engineering flight data over Lake Powell confirms that the technology of the high-

frequency channels successfully performs measurements in airborne environments and the results show improved spatial resolution of integrated water vapor retrievals compared to the low frequency microwave radiometers.

6.7. Summary of Engineering Flights

The first airborne demonstration of the HAMMR instrument was incredibly successful. The operation of the HAMMR system went very smoothly and no malfunctions occurred in flight. The ground-breaking results from these airborne measurements are the first to combine all of these channels in a single measurement [63]. The measurements from the newly-developed, high-frequency millimeter-wave radiometers showed improved spatial resolution compared to the low-frequency microwave radiometers. The results of the sounding receivers will be discussed here once the data is processed.

Chapter VII Conclusions and Future Work

The 25-channel, cross-track scanning high-frequency airborne microwave and millimeter-wave radiometer (HAMMR) system was designed, built, tested and successfully demonstrated airborne on a Twin Otter aircraft in July 2014. The addition of the high-frequency millimeter-wave channels to the microwave frequency 18-34 GHz microwave channels is expected to improve satellite-based retrieval of tropospheric wet path delay near the coast and over inland bodies of water. The initial measurements from the engineering flights show that the millimeter-wave window radiometers have better spatial resolution than the microwave receivers do. The theory, design process, and measured performance of all the radiometers were presented in this thesis. The work completed for this thesis contributed to the development, characterization, and initial airborne demonstration of the HAMMR system.

7.1. Summary

Chapter I presents the scientific motivation for the thesis in the context of accurately measuring tropospheric wet-path delay near coasts and over inland bodies of water. The Instrument Incubator Program that funded the project is also described.

In Chapter II, fundamental concepts on radiometry and atmospheric remote sensing are introduced. Ideal blackbodies, Rayleigh-Jeans Law, and emissivity are

presented to relate thermal radiation of real bodies to their physical temperature. The Rosenkranz model of absorption in the atmosphere and the radiative transfer model for downward looking radiometers are also described. Finally, the topologies of two common radiometers, total power radiometers and Dicke radiometers, and radiometric calibration techniques are detailed in this chapter.

To provide information on the HAMMR system as a whole, Chapter III describes the subsystems and radiometer channels that constitute the HAMMR instrument. First, a block diagram of the total system was provided and described in detail. The microwave radiometer channels have a dedicated section in this chapter because it does not have its own chapter as both the millimeter-wave radiometer channels do. The block diagram and performance of the microwave channels are discussed in this section. An overview of the millimeter-wave radiometers is provided, including their operating frequencies and final measured quantities. To conclude Chapter III, the Twin Otter aircraft that is used for HAMMR airborne demonstration is discussed.

Chapter IV focuses on the millimeter-wave sounding channels. The topology and components that make up the sounders are described first. The process of tuning and measurements of the waveguide diplexer used to separate the two sounding bands is given next. The 118 GHz MIMRAM is also designed as part of this thesis and the design considerations were discussed for this component. The final section discussed the design of the sounder receivers and how they are integrated on the

optical bench with all of the external sounder components. The measured results of the sounding radiometer channels are presented last.

The bulk of the content of this thesis is in Chapter V, which covered the design and lab testing of the millimeter-wave window channels. The architecture of the window channels is discussed including the benefits of the direct detection architecture that is used for these radiometers. The improvements to the millimeter-wave window channel lab prototypes developed under the ACT-08 are first summarized before going into detail on each improvement. The design and measurements of the waveguide coupler prototypes are discussed and the results showed improved performance as well as a 66% reduction in size compared to the previously used, commercially available couplers. Following this, the design process and measured results of the waveguide band definition filters were presented. By using the waveguide filters designed as part of this thesis, it allows the passband to be directly measured in its final configuration, which is critical in characterizing the performance of the window channels. The diode detector blocks and their designs are then explained in the context of interfacing with the rest of the window channel components. The most complex design is the multi-chip modules which house the internal calibration and RF MMIC chain of the receivers. The considerations and design process of the MCMs are analyzed extensively in this chapter and the measurements of each of the MCMs are also discussed. The chapter ends with the

results of the lab measurements performed on the millimeter-wave radiometers as a whole.

Chapter VI presents all of the measurements performed with the entire HAMMR instrument. Outdoor ground tests were completed during the week of June 30, 2014 to verify all the systems were working properly when integrated into the final HAMMR system. The results from the ground tests allowed the MSL team to refine the instrument and ensure it would be ready for the airborne demonstration on a Twin Otter aircraft the following week. The MSL team traveled to Twin Otter International in Grand Junction, Colorado, during the week of July 7, 2014 to integrate the HAMMR instrument on a Twin Otter aircraft and perform the first airborne demonstration of the instrument. The engineering flights of the HAMMR instrument were successful and provided the first data set ever to combine all of these channels in a single measurement. The most significant conclusion of the engineering flights was the demonstration of improved spatial resolution of the high-frequency millimeter-wave window channels compared to that of the low-frequency microwave channels.

7.2. Conclusions

Two key scientific objectives of NASA's Surface Water and Ocean Topography (SWOT) mission are to characterize the ocean mesoscale and sub-mesoscale circulation with a spatial resolution of 15 km (over 68% of the world's oceans) and

monitor the height of inland bodies of water with areas larger than 250 m^2 and flow rates of rivers at least 100 m wide. To this extent, tropospheric wet-path delay needs to be accounted to achieve 1 cm (baseline) to 3 cm (threshold) vertical resolution for sea surface height measurements.

Past and current satellite altimeter missions include nadir-viewing microwave radiometers from 18-34 GHz to retrieve tropospheric wet-path delay. These low-frequency microwave radiometers achieve retrievals with rms errors of less than 1 cm in the open ocean, up to about 40 km from the coasts. However, due to the large footprint of low-frequency microwave radiometers, land emissions contaminate the measurements in coastal areas, increasing the errors. To address this issue, we propose the addition of higher-frequency radiometers operating from 90-168 GHz to retrieve wet-path delay near the world's coastlines and potentially enabling retrievals over inland bodies of water.

The High-frequency Airborne Microwave and Millimeter-wave Radiometer (HAMMR) instrument was designed, built, tested and demonstrated on a Twin Otter aircraft as a collaborative effort between the Colorado State University (CSU) Microwave Systems Laboratory (MSL) and the Jet Propulsion Laboratory (JPL). HAMMR consists of three sets of radiometer channels, the newly-developed millimeter-wave window channels (90, 130 and 168 GHz), millimeter-wave

sounding channels (near 118 and 183 GHz), and the low-frequency microwave channels (18.7, 23.8 and 34.0 GHz).

The HAMMR instrument successfully performed measurements on a Twin Otter aircraft from Grand Junction, CO, from July 9-11, 2014. The first airborne demonstration of the high-frequency radiometers showed improved resolution compared to low-frequency microwave radiometers. In addition, the data set from the airborne demonstration is the first to combine all of these channels in a single measurement.

7.3. Lessons Learned

Because the microwave channels were not designed as part of the work for this thesis, only the lessons learned during the design and testing of the millimeter-wave channels are discussed.

7.3.1 **Millimeter-Wave Sounding Channels**

To meet deadlines for completion of the HAMMR instrument, the millimeter-wave sounding channels did not include band definition filters, video amplifiers, or diode detectors as originally intended. As a result, the output voltage of the sounding channels is only 1 mV, significantly less than the outputs of the other radiometers which are approximately 1 V. In addition, filters and diode detectors were added after the output of the sounding receivers, creating multiple interfaces before the

input of the analog back-end boards (ABEBs). As a result, the small 1 mV signals output from the sounder receivers were very prone to radio frequency interference (RFI). It was found that 60 Hz noise emitted by the power supplies of the system was being coupled onto the lines between the sounder receivers and ABEBs, resulting in oscillations on the order of tens of millivolts. Much of the noise was reduced with DC blocking capacitors inserted directly before the diode detectors; however, it is recommended in the future to output only higher voltage signals from the radiometers for input to the ABEBs, due to their immunity to coupled noise.

7.3.2 **Millimeter-Wave Window Channels**

Many practical lessons were learned during the design of the millimeter-wave window channels. When transitioning from the performance design phase in HFSS to the physical design phase in Solidworks, it is recommended to always export the physical model in the HFSS file and import it directly to Solidworks. In the first designs completed during this work, the HFSS model was transferred to Solidworks by building a new model with dimensions identical to the HFSS model; however, this is prone to human error as was seen in the 168 GHz coupler. Additionally, when fabricating similar structures for different radiometer frequency channels, it is beneficial for all the channels to be designed based on a similar structure. This was done for the 90, 130 and 168 GHz diode detector blocks. All three of them have identical outer dimensions, biasing feed-through locations, and pressure ridges.

This permits the machinist to use one CNC code for the majority of the blocks, which also reduces cost and manufacturing time.

7.4. Future Work

With the successful completion of the initial engineering flights in July 2014, HAMMR will be flown on a Twin Otter for validation flights over the coast of Southern California in the early fall of 2014. In the time between the engineering flights and validation flights, the sounding channels will continue to be debugged to find the source of the frequency offset. After the completion of the validation flights, the technology can be further developed under new grants. Ultimately, the HAMMR technology could be co-located with satellite altimeters to correct for tropospheric wet-path delay near coastlines and over inland bodies of water.

Chapter VIII Bibliography

[1] National Research Council, *Earth Science and Applications from Space: A Midterm Assessment of NASA's Implementation of the Decadal Survey*. Washington, DC: The National Academies Press, 2012.

[2] National Aeronautics and Space Administration. (2014, May) "NASA-CNES Move Forward with Global Water and Ocean Surface Mission". [Online]. http://www.nasa.gov/press/2014/may/nasa-cnes-move-forward-with-global-water-and-ocean-surface-mission/#.U7VyQ_mzGWU

[3] E. Rodriguez. (April 2014) Surface Water and Ocean Topography Mission (SWOT): Science Requirments Document.

[4] Jet Propulsion Laboratory. Ocean Surface Topography from Space. [Online]. https://sealevel.jpl.nasa.gov/

[5] A. Lee, "Developoment and Fabrication of Internally-Calibrated, MMIC-Based Millimeter-Wave Radiometers at 92 GHz and 166 GHz," M.S. Thesis, Electrical and Computer Engineering, Colorado State University, Fort Collins, CO USA, Spring 2012.

[6] D. Albers, "Design, Fabrication, and Demonstration of Low-Mass, Low-Power, Small-Volume, Direct Detection Millimeter-Wave Radiometers at 92 and 130 GHz," M.S. Thesis, Electrical and Computer Engineering, Fort Collins, CO USA, Fall 2012.

[7] National Aeronautics and Space Administration (NASA) Earth Science Technology Office (ESTO). (2014) The Instrument Incubator Program (IIP). [Online]. http://esto.nasa.gov/obs_technologies_iip.html

[8] National Aeronautics and Space Administration. (2010) IIP ROSES 2010 Solicitation. [Online]. http://esto.nasa.gov/files/solicitations/IIP_10/ROSES2010_IIP_A35.pdf

[9] F. T. Ulaby, R. K. Moore, and A. K. Fung, *Microwave Remote Sensing: Active and Passive, Vol. I - Microwave Remote Sensing Fundamentals and Radiometry*. Reading, MA: Addison-Wesley, 1981.

[10] P. W. Rosenkranz, "Water Vapor Microwave Continuum Absorption: A Comparison of Measurements and Models," *Radio Sci.*, vol. 33, no. 4, pp. 919-928, Jul.-Aug. 1998.

[11] S. Sahoo, "Radiometric Information Content for Water Vapor and Temperature," private communication.

[12] J. Randa, et al., "Recommended Terminology for Microwave Radiometry," *Institute of the National Institute of Standards and Technology*, Aug. 2008.

[13] M. Janssen, *Atmospheric Remote Sensing by Microwave Radiometry*. New York, NY: John Wiley & Sons, Inc., 1993.

[14] S. C. Reising, et al., "Development of an Internally-Calibrated Wide-Band Airborne Microwave Radiometer to Provide High-Resolution Wet-Tropospheric Path Delay Measurements for SWOT," Colorado State University, 2013.

[15] Quick Silver Controls, Inc. (2011, May) Datasheet:QCI-DS009. [Online]. http://www.quicksilvercontrols.com/SP/DS/QCI-DS009_QCI-A34.pdf

[16] T. Johnson, et al., "Design and Calibration of an Ambient Calibration Target for an Airborne Microwave and Millimeter-Wave Radiometer," in *USNC-URSI National Radio Science Meeting*, Boulder, CO, 2014.

[17] Emerson & Cuming Microwave Products. (2014) ECCOSORB HR. [Online]. http://www.eccosorb.com/products-eccosorb-hr.htm

[18] Digi-Key. (2014) Thermistors - NTC - KS502J2. [Online]. http://www.digikey.com/product-detail/en/KS502J2/615-1073-ND/2651614

[19] Superlogics. (2010) 8017: 8 Channel Analog Input, 16-Bit, Data Acquisition Module (RS-485 DAQ). [Online]. http://www.superlogics.com/option.asp?cat=807&prod=786#

[20] SPG Systems. IG-500N: GPS aided miniature INS. [Online]. http://www.sbg-systems.com/products/ig500n-miniature-ins-gps

[21] S. Nelson, "Design, Fabrication, and Testing of a Data Acquisition and Control System for an internally-Calibrated Wide-Band Microwave Airborne Radiometer," M.S. Thesis, Colorado State University, Fort Collins, Colorado, Fall 2013.

[22] Arrow Electronics. (2014) BEMICRO SDK. [Online]. https://parts.arrow.com/item/detail/arrow-development-tools/bemicrosdk#FFEJ

[23] Mediawave PC, Inc. MW-5300: Fanless Embedded Computer. [Online].

http://www.mediawavepc.com/e_MW-5300.htm

[24] Omega Engineering. 1/32 DIN Dual-Zone Controller: CN79000 Series. [Online]. http://www.omega.com/pptst/CN79000.html

[25] Riedon. TO-220 Power Film Resistors. [Online]. http://riedon.com/resistors/view/to-220-power-film-resistors-pf2200/

[26] B. A. Voronin and S. S. Voronina, "Contribution of Weak Water Vapor Absorption Lines to Extinction of Narrow-Band Laser Radiation in Atmopheric Microwindows," *Atmos. Ocean. Optics*, vol. 15, no. 4, pp. 321-324, 2002.

[27] National Aeronautics and Space Administration. (2010, May) Advanced Microwave Radiometer. [Online]. http://www.nasa.gov/mission_pages/ostm/overview/index.html#.U6xpPvmzGWU

[28] D. Baumgardner, et al., "The Cloud Particle Spectrometer with Polarization Detection (CPSPD): A Next Generation Open-Path Cloud Probe for Distinguishing Liquid Cloud Droplets from Ice Crystals," in *The 16th International Conference on Clouds and Precipitation*, Leipzig, Germany, 2014.

[29] Microwave Engineering Corporation. Antennas and Millimeter-Wave Products. [Online]. http://www.microwaveeng.com/catalog/Antennas.pdf

[30] S. C. Reising, et al., "SWOT IIP-10 Year 2 Annual Review: Development of an Internally-Calibrated Wide-Band Airborne Microwave Radiometer to Provide High-Resolution Wet-Tropospheric Path Delay Measurements for SWOT,"

2013.

[31] A. von Engeln and S. Buhler, "Temperature profile determination from microwave oxygen emissions in limb sounding geometry," *Journal of Geophysical Research: Atmospheres*, vol. 107, no. D19, 2002.

[32] National Aeronautics and Space Administration. NASA Airborne Science Program: Aircraft List. [Online]. https://airbornescience.nasa.gov/aircraft/Twin_Otter_International

[33] P. Kangaslahti, T. A., B. Lambrigsten, and D. Pukala, "MIMRAM — Miniature MMIC low mass/power Radiometers for Geostationary Thinned Aperture Radiometer," in *NASA Science Technology Conference*, College Park, MD, 2007.

[34] Microwave Communications Laboratories, Inc. (2010) 90 Degree Hybrid Coupler - Stripline. [Online]. http://mcli.com/CatalogueRetrieve.aspx?ProductID=1126960&A=SearchResult&SearchID=8076474&ObjectID=1126960&ObjectType=27

[35] ANSYS. (2014) ANSYS HFSS Features. [Online]. http://www.ansys.com/Products/Simulation+Technology/Electronics/Signal+Integrity/ANSYS+HFSS/Features

[36] G. Matthaei, L. Young, and E. M. T. Jones, *Microwave Filters, Impedance-Matching Networks, and Coupling Structures*. Norwood, MA: Artech House, Inc., 1980.

[37] Machine List. Zen Machine & Scientific Instrument. [Online]. http://www.machinelist.us/company-zen-machine-scientific-inst-in-lyons-co-5916

[38] Miteq. Mechanically-Tuned Dielectric Resonantor Oscillators. [Online]. https://miteq.com/docs/MITEQ-DROH16000.PDF

[39] Millitech. Active Multiplier Chain. [Online]. http://www.millitech.com/pdfs/specsheets/IS000037-AMC.pdf

[40] Aerowave, Inc. Attenuators. [Online]. http://www.aerowave.net/Catalog/12-13.pdf

[41] Microwave Communications Laboratories, Inc. 90 Degree Hybrid - Stripline. [Online]. http://mcli.com/products/hybrids/90-degree-hybrid-stripline

[42] Wenzel Associates, Inc. 501-04516D. [Online]. http://www.wenzel.com/wp-content/parts/501-04516.pdf

[43] Mini Circuits. Coaxial Power Splitter/Combiner. [Online]. http://www.minicircuits.com/pdfs/ZFSCJ-2-1.pdf

[44] Amphenol Connex. SMC Str Jk, Solder Cup, 50 Ohm, Blkhd. [Online]. http://www.amphenolconnex.com/152127.html

[45] Mini Circuits. Low Power Coaxial Amplifier. [Online]. http://www.minicircuits.com/pdfs/ZFL-1000.pdf

[46] Mini Circuits. Power Splitter/Combiner. [Online]. http://www.minicircuits.com/pdfs/ZFSC-4-1+.pdf

[47] S. C. Reising, et al., "Development of Low-Mass, Low-Power, High-Frequency Microwave Radiometers with Internal Calibration to Provide High-Resolution Wet-Tropospheric Path Delay Measurements for the SWOT Mission," in *Earth Science Technology Forum*, Pasadena, CA, 2011. [Online]. http://esto.nasa.gov/conferences/estf2011/papers/Reising_ESTF2011.pdf

[48] NASA ESTO. (2008) NASA's Science Mission Directorate Awards Funding for 16 Projects Under . [Online]. http://esto.nasa.gov/files/solicitations/ACT_08/ROSES2008_ACT_A21_selections.html#reising

[49] T. Johnson and T. Hadel, "Radiometer-on-a-Chip," 2012.

[50] ELVA-1 Millimeter Wave Division. (2013) Waveguide Directional Couplers. [Online]. http://www.elva-1.com/products/a40044

[51] ANSYS. (2014) ANSYS Designer RF. [Online]. http://www.ansys.com/Products/Simulation+Technology/Electronics/RF+&+Microwave/ANSYS+DesignerRF

[52] Dassault Systemes. (2014) Solidworks 3D CAD Packages. [Online]. http://www.solidworks.com/sw/products/3d-cad/packages.htm

[53] A. R. Kerr, et al. (2004, May) Alma Memo 494: MF-112 and MF-116 Compact Waveguide Loads and FTS Measurements at Room Temperature and 5 K. [Online]. http://legacy.nrao.edu/alma/memos/html-

memos/alma494/memo494.pdf

[54] Emerson & Cuming Microwave Products. (2008, Oct.) Eccosorb MF. [Online]. http://www.eccosorb.com/Collateral/Documents/English-US/MF.pdf

[55] Virginia Diodes, Inc. (2014) Detectors. [Online]. http://vadiodes.com/index.php/en/products/detectors

[56] Millitech, LLC. Rectangular Waveguide Specifications and Mil-Specification Cross Reference. [Online]. http://www.millitech.com/pdfs/recspec.pdf

[57] D. M. Pozar, *Microwave Engineering*, 4th ed. Danvers, MA: John Wiley & Sons, Inc., 2012.

[58] Microwaves 101. (18, Aug.) Microstrip. [Online]. http://www.microwaves101.com/encyclopedia/microstrip.cfm

[59] Glenair. High-Performance Micro-D Connectors and Cables. [Online]. http://www.glenair.com/micro_d/

[60] Wikipedia. (2014, Jul.) Blue Mesa Reservoir. [Online]. http://en.wikipedia.org/wiki/Blue_Mesa_Reservoir

[61] Quicksilver Controls, Inc. (2014, Jul.) QuickControl. [Online]. http://www.quicksilvercontrols.com/QuickControl.html

[62] Wikipedia. (2014, Jul.) Lake Powell. [Online]. http://en.wikipedia.org/wiki/Lake_Powell